Shale Gas Reservoir Development Strategies Using Complex Well Architectures Operating under Fixed Plateau Rate Conditions

Dr. Mari H. Alqahtani, Prof. Turgay Ertekin, and Sultan M. Almalki

ABSTRACT

In this study, artificial neural networks (ANN) were used to develop a shale gas reservoir expert system. The developed expert system provides solutions for complex wells instead of the typical massively hydraulically fractured horizontal wells (MHFHWs). The objective of the expert system was to accurately and instantaneously perform the following three tasks: (1) Predict the production profile for a given complex well structure from a given shale gas reservoir; (2) Propose a robust suite of complex well design parameters capable of producing a given production profile from a given set of reservoir properties; and (3) Predict shale reservoir rock properties corresponding to a given gas production profile from a given complex well design. All wells in this study operate under fixed plateau rate conditions.

ANN based models are capable of solving problems that do not have a definite analytical or numerical solution. As an example, one can consider the complex interaction of a complex well's transient behavior, especially in dual porosity reservoir systems as experienced in shale gas reservoirs. In addition, ANN based models have the ability to analyze large databases using their high power pattern recognition capabilities. The developed expert system is able to perform its aforementioned three tasks instantaneously at high levels of accuracy.

Developing a complex well shale gas expert system has its advantages compared to relying on conventional methods. For example, developing an analytical model to predict the performance of a complex well is an arduous task, especially in shale gas reservoirs, due to their complexities and heterogeneities. In addition, sole reliance on numerical reservoir simulation to design a complex well, capable of matching a desired production profile from a desired reservoir, consumes a lot of time to build and to run all possible scenarios, and then to optimize. Use of ANNs has the ability to overcome these challenges, as illustrated in this article.

To assess if complex wells can be an alternative to MHFHWs, both well types were compared against each other in the same reservoirs. In such a comparison, response functions such as cumulative productions, production profiles, and flowing bottom-hole pressure profiles are included. Due to the scarcity of real field data for complex wells in shale gas reservoirs, numerous reservoir simulation models were used to generate the time series of data to be used in training the expert systems.

All reservoir simulation input properties are randomly generated within a determined maximum and minimum value, and their corresponding outputs are paired together. The resulting large database is reorganized to fit the three expert system objectives, and is further divided into training, testing, and validation subsets. For each objective, an ANN based model was structured and trained on the large database. Several data transformation techniques and functional links were used to increase the ANN prediction accuracy levels.

The results prove that complex wells have the capability to meet or exceed the MHFHW plateau time and cumulative production, in shale gas reservoirs. Complex wells with their increased and targeted reservoir exposure, along with their reduced water consumption, are becoming an attractive alternative to MHFHWs.

INTRODUCTION

Unconventional gas production continues to accelerate globally with each passing year, and the increase is dominated by shale gas production. Production forecasts of natural gas are available from the U.S. Energy Intelligence Agency (EIA)[1]. The data shows that shale gas is the dominant driver in the growth of natural gas production during the next 20+ years, Fig. 1. The demand for natural gas, as consumption rises, is expected to drive an increase in shale gas in particular, and unconventional gas in general. For example, U.S. natural gas consumption is forecasted to increase even under low economic growth
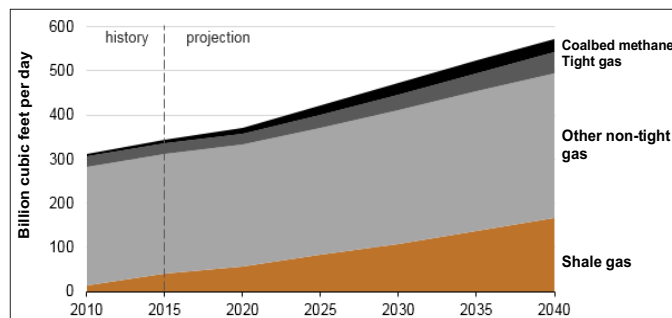

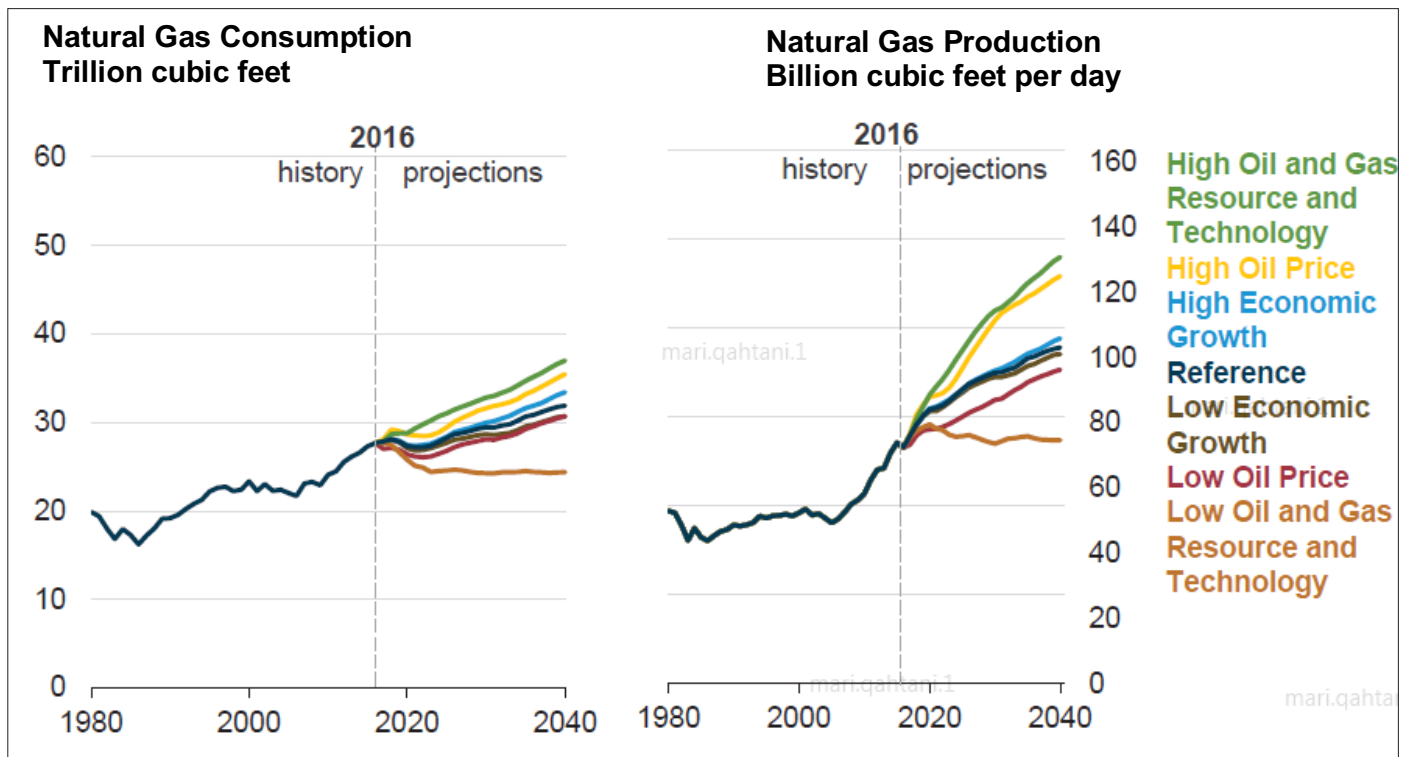*Fig. 1. Projected world natural gas production by type, from 2010 to 2040[1].*

Natural Gas Consumption Trillion cubic feet

Natural Gas Production Billion cubic feet per day

High Oil and Gas Resource and Technology
High Oil Price
High Economic Growth
Reference
Low Economic Growth
Low Oil Price
Low Oil and Gas Resource and Technology

Fig. 2. U.S. historic and forecasted natural gas consumption[2].

and low oil prices, Fig. 2[2].

In the U.S., shale gas has been produced over a period of more than a century[3]; however, it was not significantly developed and commercially produced until the last decade[4]. This shale gas development postponement has different causes, such as the supply and demand of natural gas, expensive exploitation techniques, and lack of a sufficient understanding of the unconventional resources.

Shale gas is globally available in large quantities; however, it is difficult to develop shale gas resources due to their low permeability characteristics, typically less than 0.001 millidarcies[5].

ASSESSING THE LEVEL OF CONFINEMENT IN HYDRAULIC FRACTURES IN SHALE GAS FORMATIONS

The hydraulically fracturing of shale formations faces several disadvantages such as consuming large quantities of water and confining the hydraulic fractures within the region of interest. The longer the half-length of the hydraulic fracture, the lower its level of confinement becomes. The existing natural fracture networks and their hydraulic connectivities have a controlling effect on hydraulic fracture propagation.

Several studies have shown that hydraulic fractures in naturally fractured reservoirs, such as shale formations, are more likely to follow a complex to a very complex geometry, Fig. 3[6, 7].

This complex geometry is affected by a number of factors, such as in situ stress distribution, natural fracture connectivity, fluid leakoff from the propagating fracture, natural fracture orientation, and the tip of the fracture effect. As existing

hydraulic fracture models are not capable of capturing such a complex hydraulic fracture propagation, new models are required to accurately capture their complex geometry[6, 8, 9].

Not all authors consider all of the aforementioned complexities in their studies. For example, some authors consider the fluid leakoff from the propagating fracture in their hydraulic fractures model[8] while others assume there is no leakoff[10]. Dahi-Taleghani and Olson (2011)[8] have considered the shear stress caused by hydraulic fracture fluid leakoff into the natural fractures, and natural fractures reopening due to stress caused by the tip effect. Their model is based on the assumption that hydraulic fractures will propagate in the direction of intersecting natural fractures. Then, they modified their model and indicated that when hydraulic fractures intersect natural
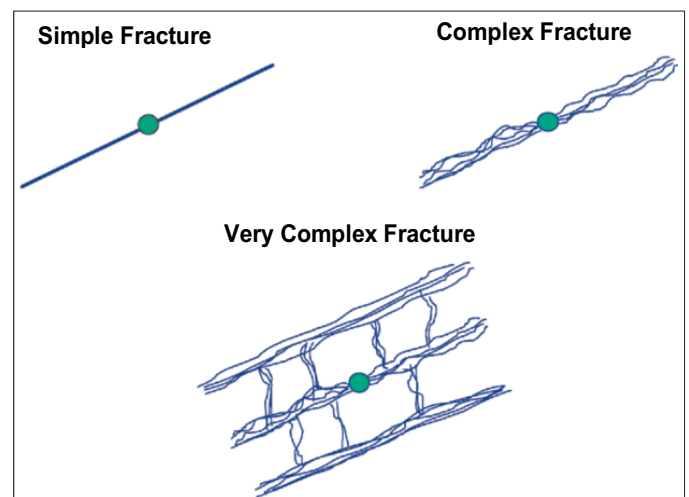

Simple Fracture   **Complex Fracture**

Very Complex Fracture

Fig. 3. Hydraulic fracture complexity: simple, complex and very complex fractures[6].
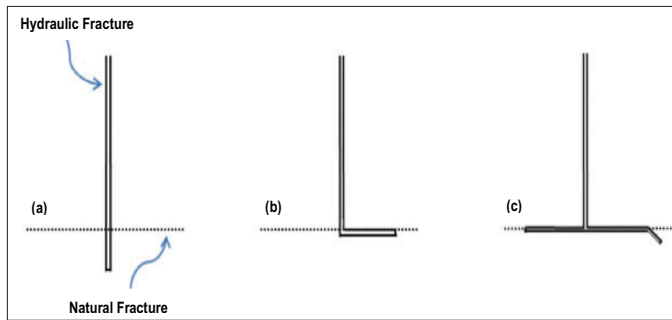
Fig. 4. Possible scenarios at the normal intersection of a hydraulic fracture and a natural fracture: (a) hydraulic fracture crosses natural fracture without incident, (b) hydraulic fracture ends at natural fracture, and (c) hydraulic fracture diverts into natural fracture and propagation continues[8].

fractures, they can get arrested by it or cut through it, Fig. 4[8].

Some investigators have evaluated the fracture propagation that would occur after a hydraulic fracture intersects an existing natural fracture. Their model indicates that when a hydraulic fracture intersects a natural fracture, one of the following scenarios would occur: (1) crossing the natural fracture, dilation of the natural fracture, then propagation from the tip of the natural fracture, or (2) dilation of the natural fracture, then breakout of a fracture from along the natural fracture[11].

Most hydraulic fracture analysis models, when implemented in natural fractured reservoirs, highlight the uncertainty associated with the propagation direction and the level of confinement. Low level confinement becomes more pronounced in massive hydraulic fractures commonly used in shale gas wells.

Complex Wells

In this research, complex wells are considered an attractive alternative to the massively hydraulically fractured horizontal wells (MHFHWs) as complex wells have more reservoir control and contact. Since their early 1990s commencement, complex wells have seen an increase in their field application[12, 13]. In comparison to single lateral horizontal wells, maximum reservoir contact wells have lower cost per barrel and higher net present value (NPV)[14, 15]. While fishbone wells and MHFWHs can generate similar NPV, fishbone wells are more favorable since in their implementation, lower levels of uncertainty are encountered[16].

Rate transient behavior of the complex well's laterals is not fully understood in general, particularly in dual porosity and/or dual permeability reservoirs. There is no available analytical model that predicts the complex well's behavior along with their lateral's interaction.

There have been few studies conducted to solve this problem numerically. For instance, segmenting laterals and then superimposing results to get a final solution is used in a number of studies[12, 17]. Another approach used is representing each lateral as a partially penetrating well and then summing up their transient and pseudo steady-state solutions[18].

Artificial Intelligence and its Applications to Oil and Gas Reservoirs

Artificial intelligence applications have been proven effective in solving field development and optimization, and in complex well design problems. Fuzzy logic, genetic algorithms, and acceleration routines were used in several studies to select optimal complex well design, location, and trajectory[19-21]. Furthermore, functional transformation, neuro simulators, dimension reduction techniques, fuzzy logic, stochastic modeling, and parallel predictive models were used to develop neuro simulators, forecast natural gas production for 20 years in the U.S., and develop a top-down reservoir model capable of identifying reservoir sweet spots, and estimating reserves[22-26].

An artificial neural network (ANN) based model is a powerful tool that can learn the relationship between input parameters and their corresponding outputs. The relationship between input and output parameters, or the governing equation, can be linear or nonlinear. This feature of ANN becomes most useful when the relationship between inputs and outputs is not yet known. Although a trained ANN can predict a solution within a specific acceptable error range, it lacks the ability to explicitly state the relationship between input and output parameters.

To predict output parameters, ANN relies on a number of weights and biases. At the training phase, the ANN develops and calibrates its weights and biases during the trial-and-error process linking the input layer to the output layer. To minimize the approximation error, the ANN uses the gradient descent technique in which the input layer is connected to the output layer through a number of user specified hidden layers, Fig. 5. Each layer is connected to the other layers by neurons and transfer functions. The user chooses the transfer functions,
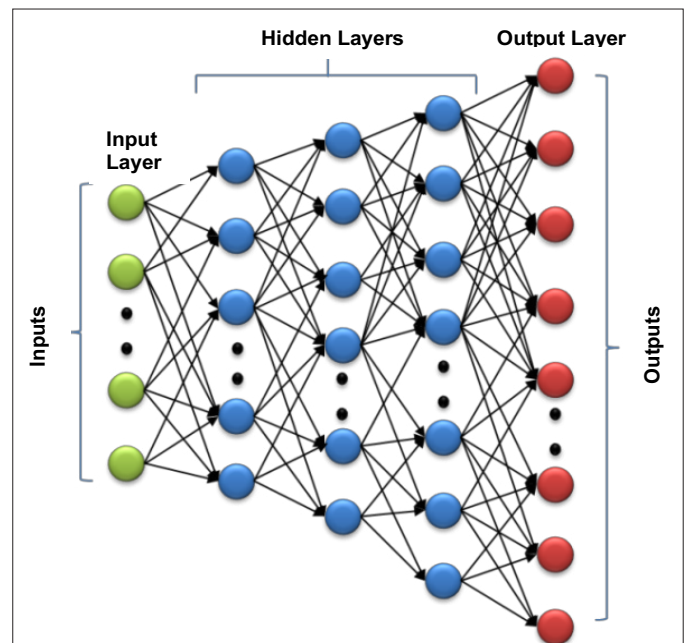

Fig. 5. A schematic showing how the input layer is connected to the output layer through a series of specified layers.

Name	Input/Output Relation	Icon	MATLAB Function
Hard Limit	$a = 0 \quad n < 0$ $a = 1 \quad n \geq 0$		hardlim
Symmetrical Hard Limit	$a = -1 \quad n < 0$ $a = +1 \quad n \geq 0$		hardlim
Linear	$a = n$		purelin
Saturating Linear	$a = 0 \quad n < 0$ $a = n \quad 0 \leq n \leq 1$ $a = 1 \quad n > 1$		satlin
Symmetric Saturating Linear	$a = -1 \quad n < -1$ $a = n \quad -1 \leq n \leq 1$ $a = 1 \quad n > 1$		satlins
Log-Sigmoid	$a = \dfrac{1}{1 + e^{-n}}$		logsig
Hyperbolic Tangent Sigmoid	$a = \dfrac{e^n - e^{-n}}{e^n + e^{-n}}$		tansig
Positive Linear	$a = 0 \quad n < 0$ $a = n \quad 0 \leq n$		poslin
Competitive	$a = 1 \quad$ neuron with max n $a = 0 \quad$ all other neurons		compet

Table 1. Commonly used transfer functions[27]

which can be linear or nonlinear, that best suits the problem[27]. Table 1 is a list of commonly used transfer functions.

METHODOLOGY

The objective of this research is to use ANNs to develop an expert system that instantaneously and accurately performs the following tasks:

1. Forward Production Profile Expert System — Fixed Plateau Rate (FEx-P): The trained ANN in this expert system, predicts — within an acceptable error range — the complex well's production profile. The FEx-P uses reservoir properties and complex well design parameters as inputs.

2. Inverse Well Architecture Design Expert System — Fixed Plateau Rate (IWEx-P): The trained ANN in this expert system, predicts — within an acceptable error range — a complex well's design capable of delivering the user defined production profile. The IWEx-P uses the production profile and reservoir properties as inputs.

3. Inverse Reservoir Rock Properties Expert System — Fixed Plateau Rate (IREx-P): The trained ANN in this expert system, predicts — within an acceptable error range — the reservoir rock properties. The IREx-P uses the production profile and the complex well's design parameters as inputs.

A large enough database that spans all possible ranges is needed in ANN training to achieve the previously stated goals. Subsequently, comparing a complex well's performance against the MHFHWs performance is needed as a preliminary step. This comparison is needed to ensure that the complex wells can be an alternative to MHFHWs prior to ANN training.
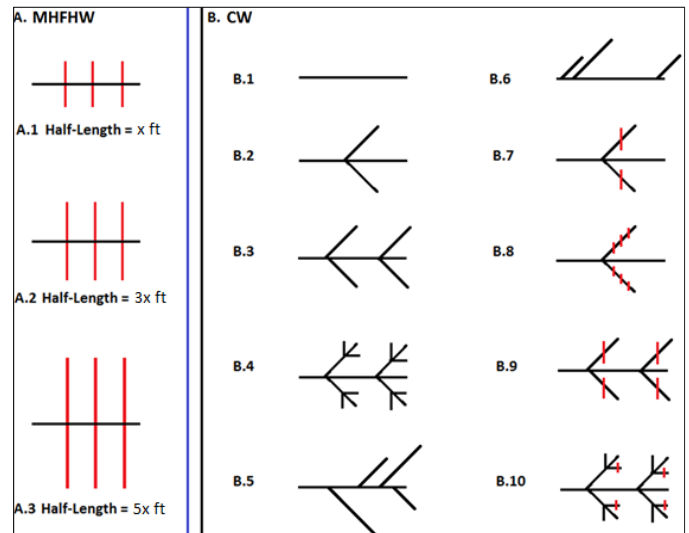

Fig. 6. Samples of different MHFHW architectures (left) and different complex well architectures (right) used in their production performance comparison. The red lines represent hydraulic fractures[21].

Comparing Performance of Complex Wells against MHFHWs

To ensure the relevance in comparison, all numerical reservoir simulation cases, which were compared against each other, share the same reservoir conditions and parameters, fluid properties, and well operating conditions. Production profiles from several MHFHWs that differ in their designs were compared against several complex wells that differ in their designs as well. Figure 6 shows a sample of the different complex wells and MHFHW architectures used in this comparison[21].

Data Gathering and Preparation

To achieve acceptable accuracy from an ANN, the expert system needs to be trained using an accurate database that is significant in size, so as to be inclusive to different combinations of input parameters. The challenge that has been faced in this research is the scarcity of complex well data in shale gas formations. It is desired to have 500+ complex well cases that capture variations in rock properties, production profiles, and well design. Currently, such a comprehensive database does not exist as it involves complex well operations in shale gas reservoirs. Therefore, training the ANN on real data is not possible at this time. To overcome this challenge we are utilizing a commercial reservoir simulation software that is capable of simulating dual permeability and/or dual porosity reservoirs. A large number of randomly generated shale gas models were generated. Their inputs and outputs were compiled to form the database that the ANN is receiving to conduct its training, validating, and testing.

All input and output parameters in the generated database have to capture the minimum and maximum limits set by the user. For example, if the user defines a reservoir thickness between 10 ft and 400 ft, and the complex wells have a number of laterals — between two and seven — then the database must include cases with reservoir thicknesses between 10 ft and 400 ft, and must include complex wells designed with 2, 3, 4, 5, 6, and 7 laterals. All minimum and maximum limits of reservoir rock and complex well design parameters utilized in

this investigation are presented in Tables 2 and 3, respectively. Furthermore, Tables 4, 5, and 6 show the input parameters of each of the three expert systems developed in this study.

ANN Training and Optimization Workflow

The generated database consists of a large number of data sets. Each data set consists of reservoir properties, complex well design parameters, and a corresponding production profile. Data sets are divided into appropriate inputs and outputs based on the prediction mode, for either forward or inverse prediction applications. For each prediction mode, the database is divided into three groups, i.e., training, validation, and testing data sets.

During the training phase, ANN calibrates its weights and biases until it reaches an acceptable error margin. During the subsequent validation phase, ANN gets exposed to new data sets, and it further calibrates its weights and biases. If the desired level of accuracy is not achieved during the validation phase, then the training phase needs to be repeated again, but the knowledge gained in the validation phase is kept by the ANN to better aid the next training phase. Once an acceptable error is reached, then the testing phase begins. Throughout the testing phase, the trained ANN gets introduced to a new testing data set, which was not shown to the expert either during the training or validation phases. If the desired

Horizontal Mainbore Length (ft)	864 – 1836
Number of Laterals	1 – 8
Length of Laterals (ft)	382 – 1756
Location of Mainbore (j^{th} row)	(middle row of 55, 77, 95, or 109 cells)
Lateral Spacing (ft)	54 – 1,836
Lateral Phase Angle (degrees)	45
Lateral Placement Pattern	Fishbone Pattern
Wellbore Constant Pressure p_{wf} (psi)	2,000 – 5,500

Table 3. The parameters of the complex well design

Reservoir Properties			Fluid Composition	
Reservoir Size (acres)	200 – 800		C1	1.00000
Initial Reservoir Pressure P_i (psia)	4,000 – 6,000		C2	0.00000
Reservoir Temperature (°F)	140		C3	0.00000
Matrix Porosity (%)	5 – 10		iC4	0.00000
Fracture Porosity (%)	1% – 10% of Matrix Porosity		nC4	0.00000
Matrix Permeability (i,j) (md)	1.0E-05 – 1.0E-04		iC5	0.00000
Fracture Permeability (i,j) (md)	0.01 – 1.0		nC5	0.00000
Reservoir Thickness (ft)	50 – 300		C6	0.00000
Fracture Spacing (i,j,k) (ft)	1 – 5		C7+	0.00000

Table 2. The minimum and maximum limits of the reservoir and fluid properties

Category	Parameter	Unit
Well Design Parameters	Mainbore Length	ft
	Well Location with Respect to the Northern Reservoir Boundary	ft
	Well Location with Respect to the Western Reservoir Boundary	ft
	Number of Laterals	
	First Lateral Direction	1 - upward 2 - downward
	Second Lateral Direction	
	Third Lateral Direction	
	Fourth Lateral Direction	
	Fifth Lateral Direction	
	Sixth Lateral Direction	
	Seventh Lateral Direction	
	Eighth Lateral Direction	
	First Lateral Spacing	ft
	Second Lateral Spacing	
	Third Lateral Spacing	
	Fourth Lateral Spacing	
	Fifth Lateral Spacing	
	Sixth Lateral Spacing	
	Seventh Lateral Spacing	
	Eighth Lateral Spacing	
	First Lateral Length	ft
	Second Lateral Length	
	Third Lateral Length	
	Fourth Lateral Length	
	Fifth Lateral Length	
	Sixth Lateral Length	
	Seventh Lateral Length	
	Eighth Lateral Length	
Reservoir Properties	Drainage Area	Acres
	Reservoir Thickness	ft
	Initial Reservoir Pressure (p_i)	psi
Well Operating Condition	Flowing BHP (p_{wf})	psi
Reservoir Properties	Matrix Porosity (ϕm)	fraction
	Natural Fracture Porosity (ϕf)	fraction
	Matrix Permeability (km)	md
	Natural Fracture Permeability (kf)	md
	Natural Fracture Spacing	ft

Table 4. The input parameters of the FEx-P

Category	Parameter	Unit
Reservoir Properties	Drainage Area	Acres
	Reservoir Thickness	ft
	Initial Reservoir Pressure (p_i)	psi
Well Operating Condition	Flowing BHP (p_{wf})	psi
Reservoir Properties	Matrix Porosity (ϕm)	fraction
	Natural Fracture Porosity (ϕf)	fraction
	Matrix Permeability (km)	md
	Natural Fracture Permeability (kf)	md
	Natural Fracture Spacing	ft
Well Performance	Cumulative Production at Day 1	scf
	Cumulative Production at Day 30	
	Cumulative Production at Day 60	
	… … …	
	… … …	
	Cumulative Production at Day 3,600	

Table 5. The input parameters of the IWEx-P

accuracy level is not observed in the testing phase (blind testing phase), then input combinations that are less represented and contribute more to error are identified. More cases representing these input combinations are generated to be introduced to the original database. Figure 7 is a workflow for the ANN training process[29].

When the ANN is trained for the first time, it is always trained on the original input and output data set, without data manipulation, modifications, or functional links. This allows the user to experiment with data manipulation techniques and functional links. The user will understand how the ANN responds to each change individually, and to a combination of changes. Accordingly, the original data set becomes a reference point for the user. At the optimization stage, the goal of the trainer becomes increasing ANN prediction accuracy. This is done by either modifying the ANN structure, by changing and introducing/or removing neurons, functional links, or new data sets. In other words, the user can introduce functional links, change the learning function, change the training function, change the transfer function, change the number of layers, change the number of neurons in some or all layers, and/or user data manipulation techniques.

There is a difference in how an error is defined in forward prediction problems vs. inverse prediction problems. In a forward prediction problem, an error is simply the percentage of difference between the actual outcomes and predicted outcomes — in reference to actual outcomes. In this research,

Category	Parameter	Unit
Well Design Parameters	Mainbore Length	ft
	Well Location with Respect to the Northern Reservoir Boundary	ft
	Well Location with Respect to the Western Reservoir Boundary	ft
	Number of Laterals	
	First Lateral Direction	1 - upward 2 - downward
	Second Lateral Direction	
	Third Lateral Direction	
	Fourth Lateral Direction	
	Fifth Lateral Direction	
	Sixth Lateral Direction	
	Seventh Lateral Direction	
	Eighth Lateral Direction	
	First Lateral Spacing	ft
	Second Lateral Spacing	
	Third Lateral Spacing	
	Fourth Lateral Spacing	
	Fifth Lateral Spacing	
	Sixth Lateral Spacing	
	Seventh Lateral Spacing	
	Eighth Lateral Spacing	
	First Lateral Length	ft
	Second Lateral Length	
	Third Lateral Length	
	Fourth Lateral Length	
	Fifth Lateral Length	
	Sixth Lateral Length	
	Seventh Lateral Length	
	Eighth Lateral Length	
Reservoir Properties	Reservoir Thickness	ft
	Initial Reservoir Pressure (p_i)	psi
Well Operating Condition	Flowing BHP (p_{wf})	psi
Well Performance	Cumulative Production at Day 1	scf
	Cumulative Production at Day 30	
	Cumulative Production at Day 60	
	... ...	
	... ...	
	Cumulative Production at Day 1,080	

Table 6. The input parameters of the IREx-P

simulation production profiles represent the actual outcomes, and the ANN production profiles represent the predicted outcomes. On the other hand, inverse prediction problems are different than forward prediction problems in terms of error calculations. In inverse prediction problems, it would be misleading to define the error margins based on the prediction accuracy of outputs, due to the non-unique nature of the inverse problems. The nature of the non-uniqueness of a solution is better explained by the case illustrated in Fig. 8, where the expert system is predicting the complex well design for a given production profile from a given set of reservoir properties.

It is clear that the well design in the simulation model (actual outcome) and the predicted well design (predicted outcome) are totally different. Both wells have different mainbore lengths, lateral lengths, lateral directions, lateral spacing, etc. Therefore, if the error was based on the ANN's ability to reproduce the same well design, we would have been misled by a huge percentage error. Subsequently, going back to Fig. 8, we realized that both wells were capable of producing the desired production profile from the same set of reservoir properties. In other words, the solution of this inverse prediction problem is not unique; therefore, several different well designs can reproduce the same production profile from the same set of reservoir properties. For this reason, we have implemented a closed loop error calculation in the inverse prediction problems, where the error is based on the predicted parameter's ability to reproduce the desired production profile.

RESULTS

The results of this study show that complex wells can meet or exceed the performance of MHFHWs. In addition, this research shows that a well-trained ANN is capable of accurately and instantaneously predicting production profiles, reservoir properties, and complex well design parameters in shale gas reservoirs. At the initial stage of this research, it was observed that ANN prediction ability is improved, especially when production profiles are monotonically increasing. Therefore, the cumulative production profiles were used instead of production rates in ANN training.

Complex Wells and MHFHW Comparison

The outcomes of this numerical reservoir simulation model comparison highlight the fact that complex wells have the capability of meeting or exceeding the MHFHW's overall cumulative production and plateau time. Figure 9[29] shows two examples of complex wells with higher production than the corresponding MHFHWs.

Further analysis of the different complex well architectures used and their production profiles, has led to a specific complex well configuration that has the tendency to mimic the MHFHW production profiles, Fig. 10[29]. This general
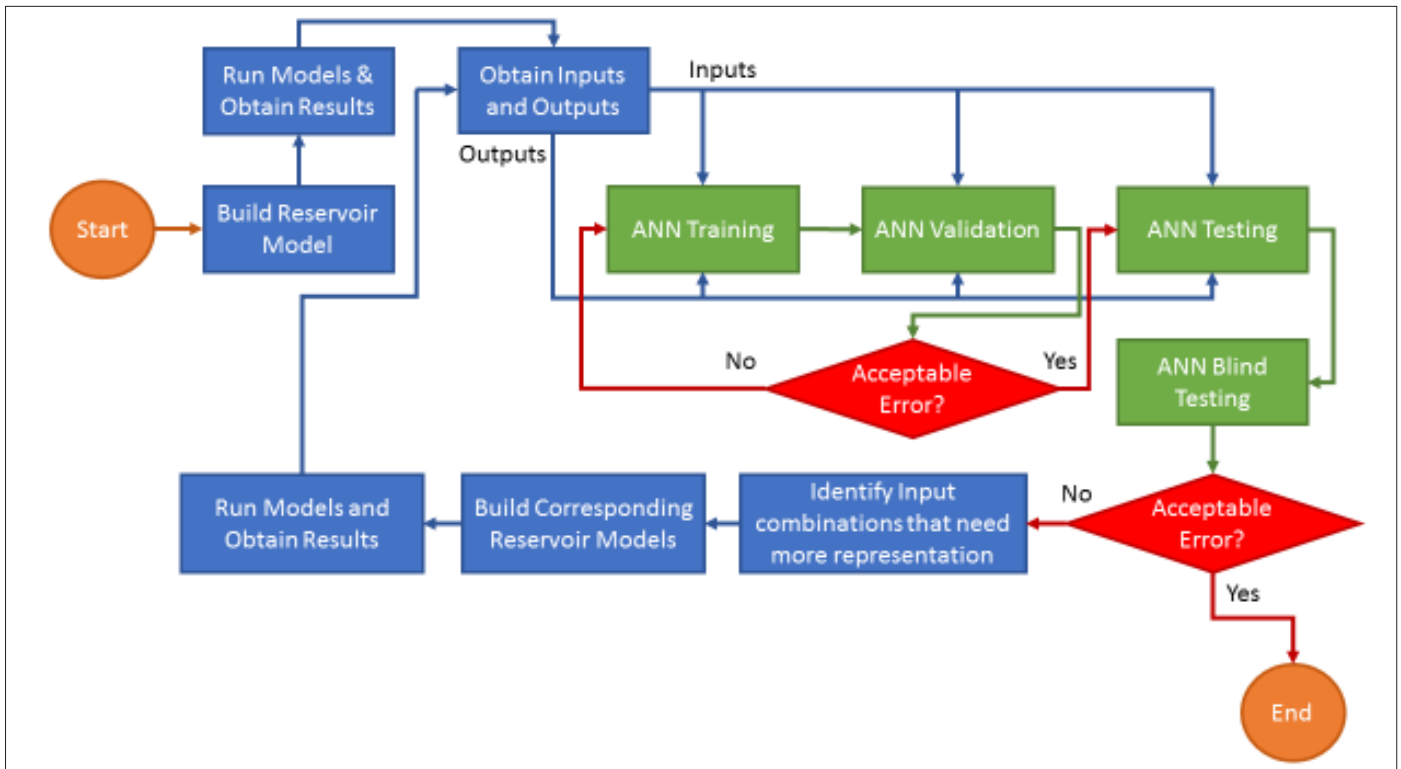
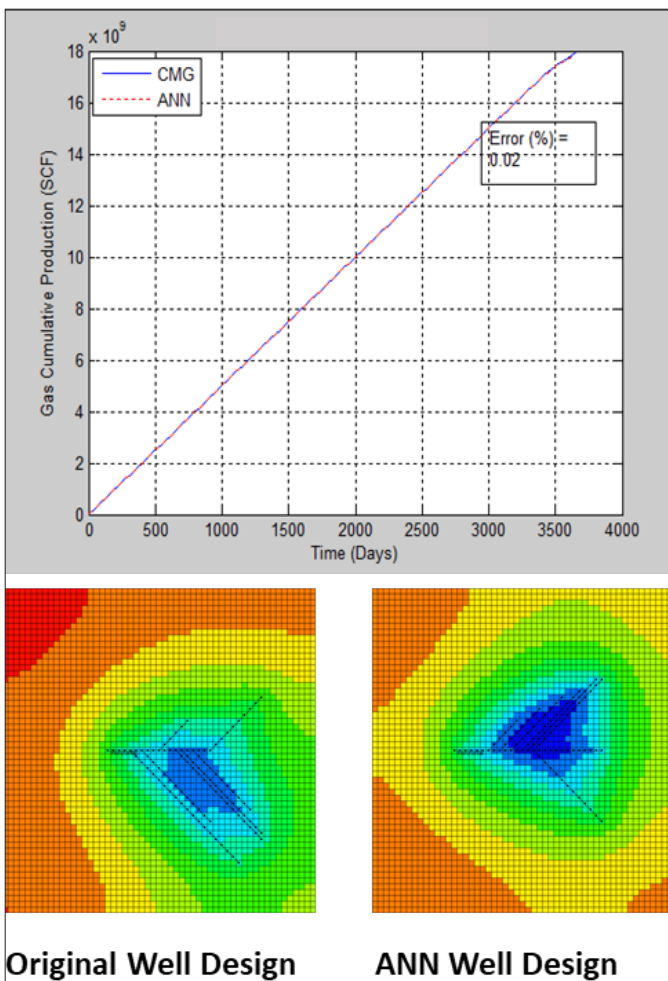Fig. 7. Workflow for the ANN training process[29].

Fig. 8. A comparison of the simulation vs. the ANN results of well designs and production profiles (0.02% error based on production profiles).

complex well architecture became a subject of several well configuration sensitivities and comparative studies with the goal of matching the MHFHW production profiles. An exact match was achieved by the complex well configuration shown in Figs. 11 and 12[29]. This complex well configuration has a horizontal mainbore and two 45° laterals that share the same origin on the mainbore. Each lateral has a uniformly spaced mini-hydraulic fracture. All mini-hydraulic fractures share the same height, width, permeability, and porosity as the massive hydraulic fractures in the MHFHW in this comparison. This complex well configuration can match any MHFHW as long as changes in mainbore and lateral lengths are proportional, and while hydraulic and mini-hydraulic fracture spacing is kept the same, on both complex wells and MHFHWs.

A number of sensitivities were performed on the mini-hydraulic fractures and the massive hydraulic fractures lengths. Cases that yielded matching profiles are highlighted in Table 7. These matching cases indicate that the half-lengths of the mini-hydraulic fractures of the matching complex well configurations are in correlation with the half-lengths of the massive hydraulic fractures of the MHFHW, as per Eqn. 1. This equation is applicable to dual porosity reservoirs with isotropic natural fractures and matrix permeability ($k_{m-x} = k_{m-y} = k_{m-z}$ and $k_{f-x} = k_{f-y} = k_{f-z}$).

$$Mini\text{-}HF\ HL = (MHF\ HL - 100)\ /\ 2 \qquad (1)$$

where *Mini-HF HL* is mini-hydraulic fracture half-length (ft), and *MHF HL* is massive hydraulic fracture half-length (ft).
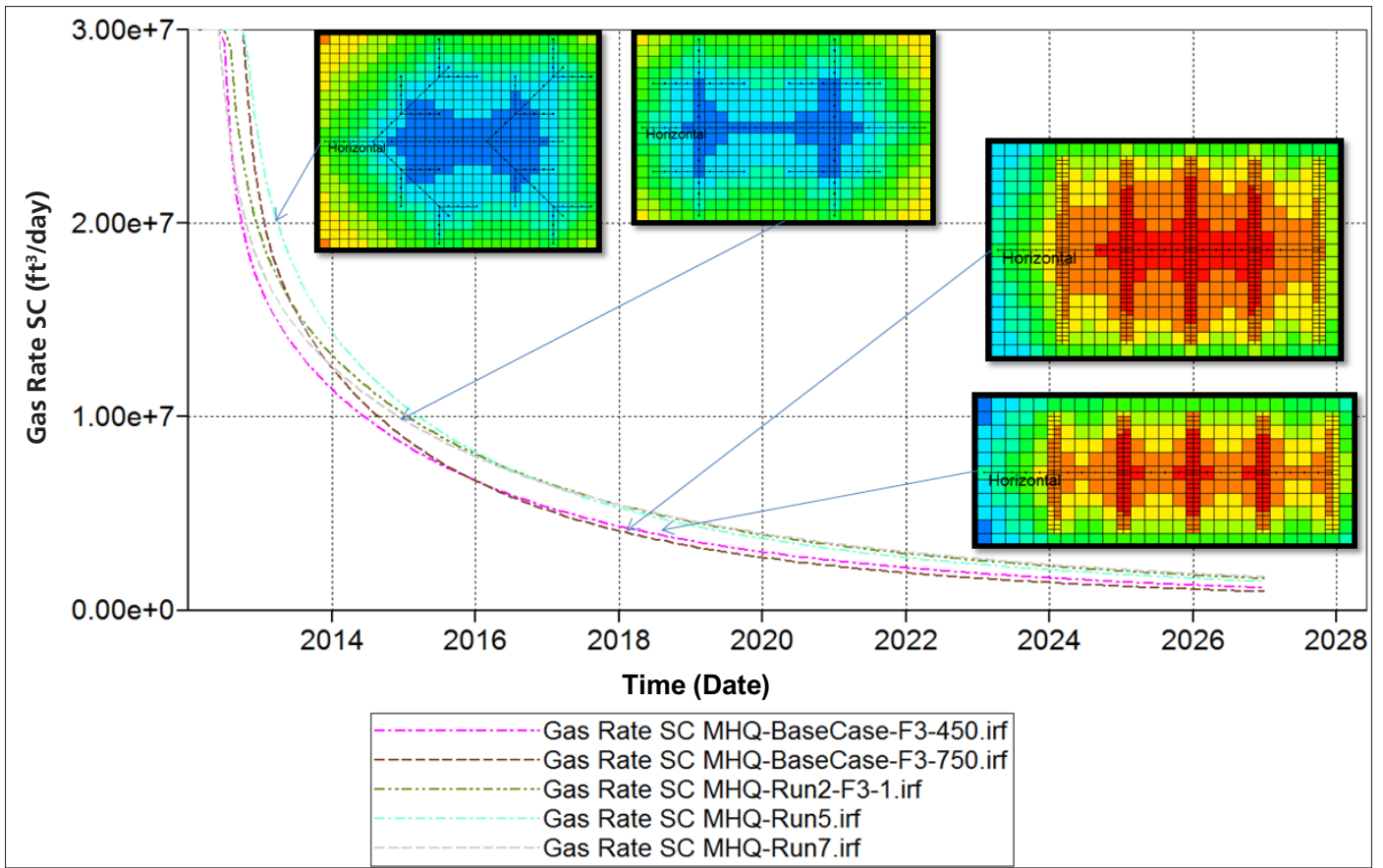
Fig. 9. Two examples of complex well architectures that are over-performing two corresponding MHFHWs[29].
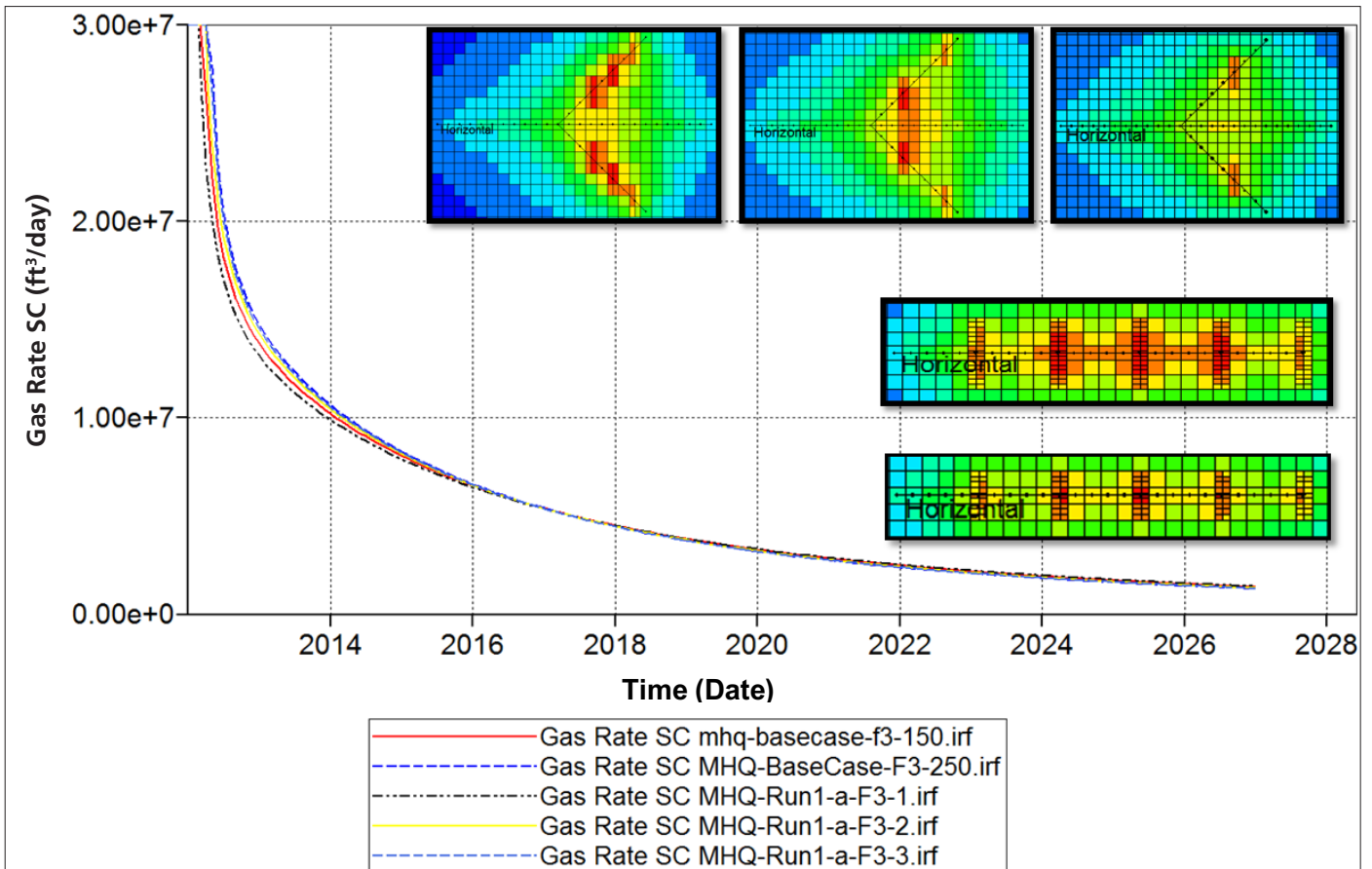

Fig. 10. Complex well configurations with a tendency to mimic the MHFHW production profiles[29].
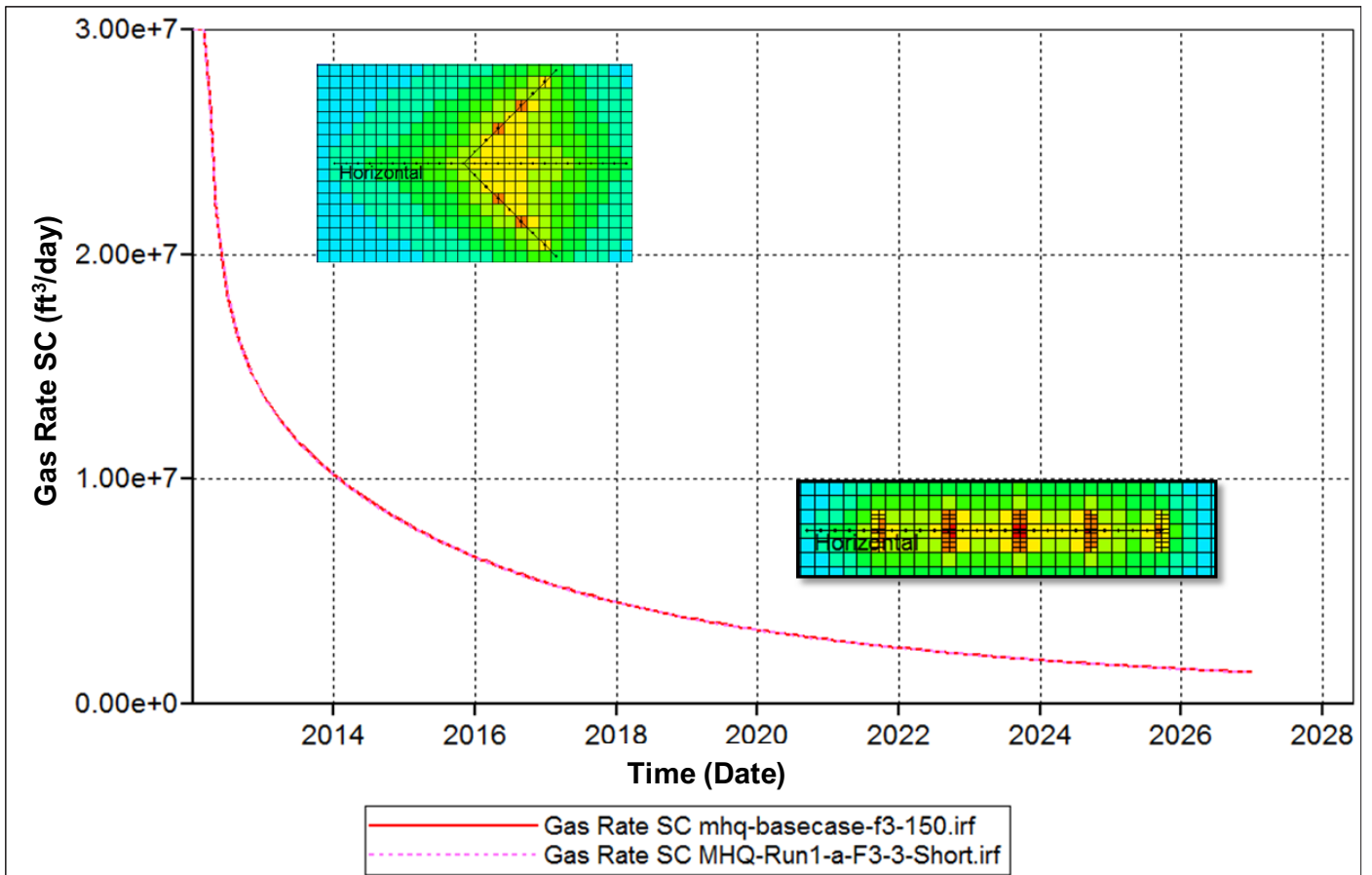
Fig. 11. A five stage MHFHW with 0.03 ft width and 150 ft half-length, and complex wells with six mini-hydraulic fractures of 0.03 ft width and 25 ft half-length[29].
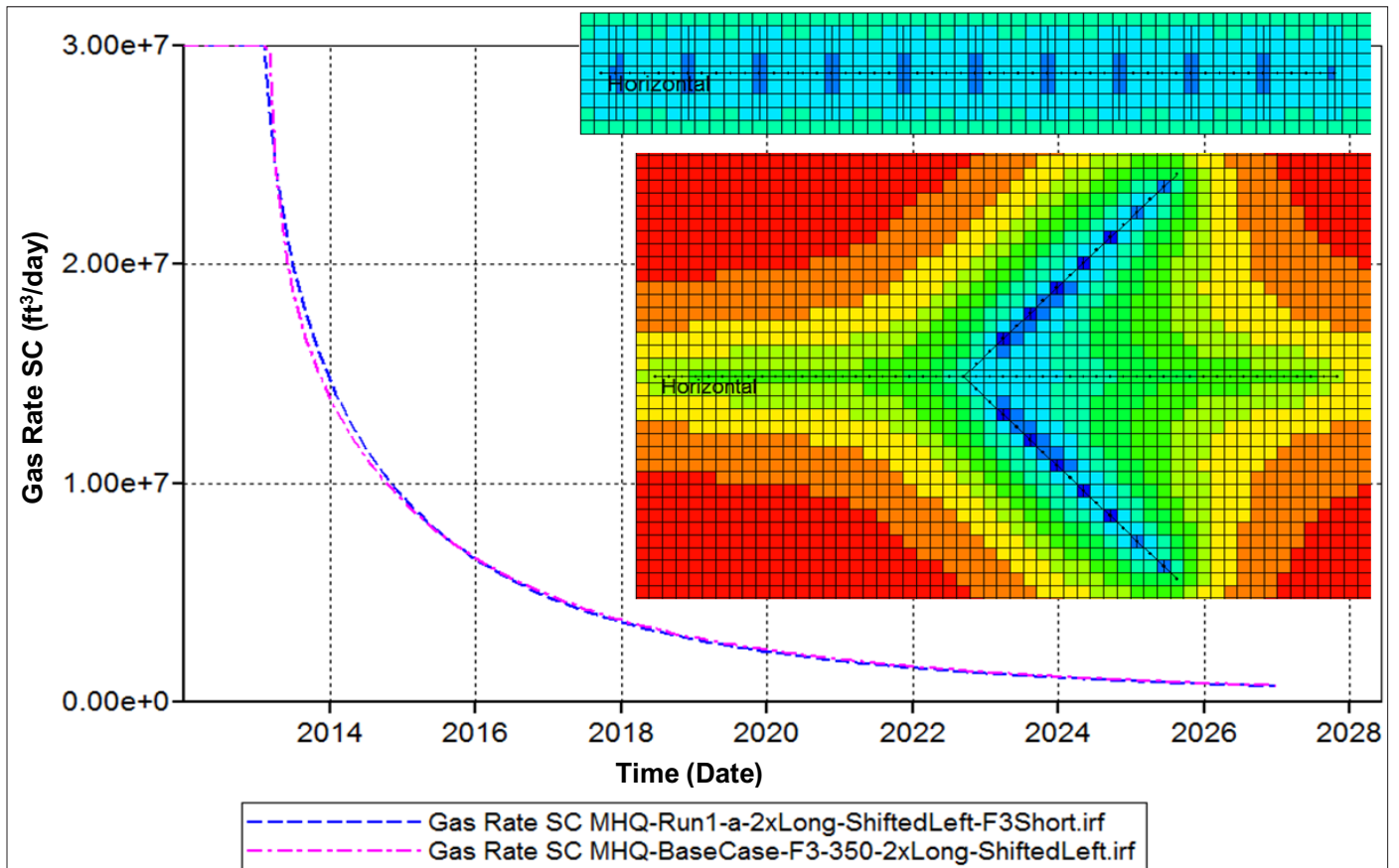

Fig. 12. An 11 stage MHFHW with 0.03 ft width and 150 ft half-length, and complex wells with 14 mini-hydraulic fractures of 0.03 ft width and 25 ft half-length[29].

Massive Hydraulic Fractures		Mini-Hydraulic Fractures	
Half Length (ft)	Total Length (ft)	Half Length (ft)	Total Length (ft)
150	1,500	25.000	300
250	2,500	41.667	500
350	3,500	58.333	700
450	4,500	75.000	900
550	5,500	91.667	1,100
650	6,500	108.333	1,300
750	7,500	125.000	1,500

Table 7. Results of a sensitivity study performed on the massive hydraulic fracture lengths and the mini-hydraulic fracture lengths, where matching cases are highlighted with the same color

Forward Production Profile Expert System — Fixed Plateau Rate (FEx-P)

Within its training range and for any given complex well design parameters, and any given shale gas reservoir properties, the FEx-P can accurately and instantaneously predict cumulative production profiles. The ANN design parameters of this expert system are shown in Table 8.

To improve the accuracy levels during training of the ANN, simple functional links and complex functional links, Table 9, and data manipulation techniques, Table 10, were introduced as input and output neurons. Data manipulation techniques have noticeably reduced the prediction error, but its primary contribution was reducing the observed oscillations in predicted profiles. Trial and error, quantification of the error source, the lessons learned from Alqahtani and Ertekin (2017)[28], and work on the FEx-P expert system were all used to come up with the optimum combination of functional links, data manipulation techniques, and ANN structure.

Predicting the time for the end of the plateau period is critically important for wells operating under fixed plateau rate conditions. At initial stages of training of the FEx-P, time at the end of the plateau was an output parameter that the ANN was trained to predict, as well as the cumulative production profile. Subsequently, further analysis of the results showed

Network Type	Feed-forward with Back Propagation
Number of Hidden Layers	3
Number of Neurons for Hidden Layers	(6, 10, 14)
Number of Case Scenarios	743
Train, Validate, Test Ratio (%)	(75, 24, 1)
Training Function	Trainscg (Scaled Conjugate Gradient)
Transfer Functions	(Tansig, Tansig, Logsig)
Learning Function	Learngdm
Performance Function	Msereg (Mean Square Error with Reg.)
Minimum Performance Goal	5E-05
Maximum Number of Validation Increases	1,000
Maximum Number of Training Iterations	8,000
Minimum Gradient Magnitude	1E-06

Table 8. The ANN design parameters of the FEx-P

Number	Functional Link	Input or Output
FL 1	Matrix Porosity * Fracture Porosity	Input
FL 2	SQRT [Matrix Permeability^2+ Fracture Permeability^2]	Input
FL 3	Maximum (Eigen Values — Matrix Permeability and Fracture Permeability)	Input
FL 4	Mainbore Length/Reservoir Area	Input
FL 5	Mainbore Length/Reservoir Thickness	Input
FL 6	Total Wellbore Length (Mainbore + All Laterals)	Input
FL 7	Reservoir Thickness * Reservoir Area * Matrix Porosity	Input
FL 8	Reservoir Thickness * Reservoir Area * Matrix Porosity * Matrix Permeability	Input
FL 9	Reservoir Thickness * Reservoir Area * Matrix Porosity * Fracture Permeability	Input

Table 9. The functional links of the FEx-P

Number	Parameter	Input or Output
DM 1	1/(Matrix Porosity)	Input
DM 2	1/(Fracture Porosity)	Input
DM 3	1/(Matrix Permeability)	Input
DM 4	1/(Fracture Permeability)	Input

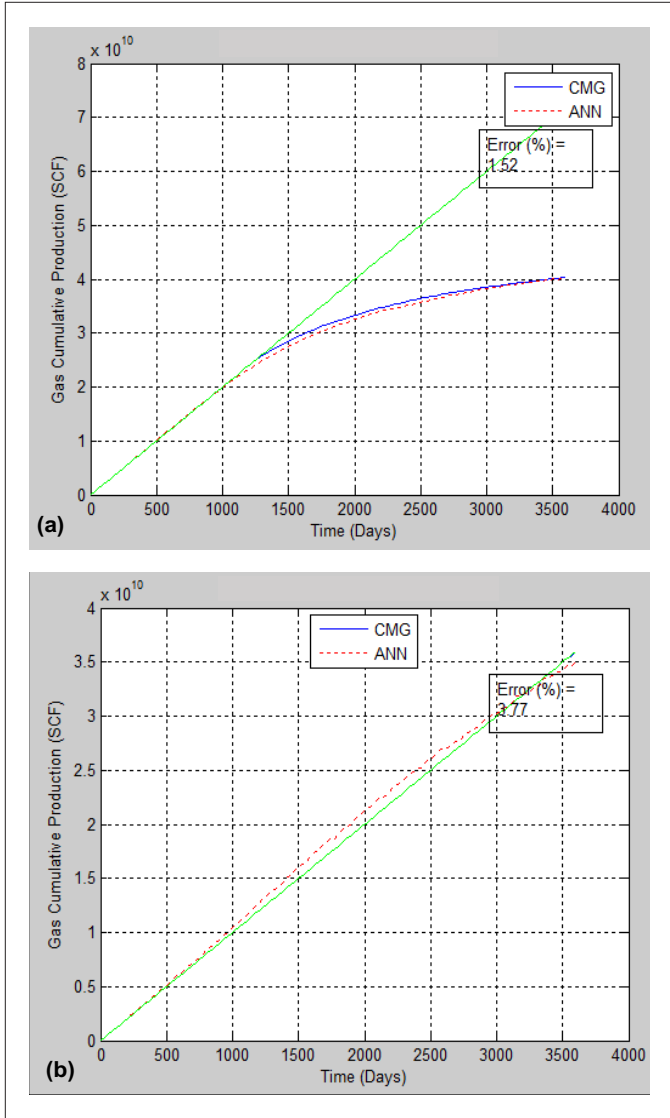Table 10. The data manipulation techniques of the FEx-P

(a)

(b)

Fig. 13. Two examples of the simulation results vs. the ANN predictions of an original test case (1.52% and 3.77% error): (a) shows a good match between the ANN and the simulation, and a time at the end of the plateau of 1,300 days; (b) shows a good match between the ANN and the simulation, and a plateau that extends beyond the 10-year time frame of the study.

that predicting time at the end of the plateau was a source of high prediction error, and it was consequently removed to improve accuracy. The ANN was not able to make an accurate prediction of time at the end of the plateau because it was not consistent in all cases, and in some cases it did not have a logical connection to the input parameters.

Since all cases have a 10-year production profile, the database was consequently divided into two categories. The first category has a known time at the end of the plateau, and
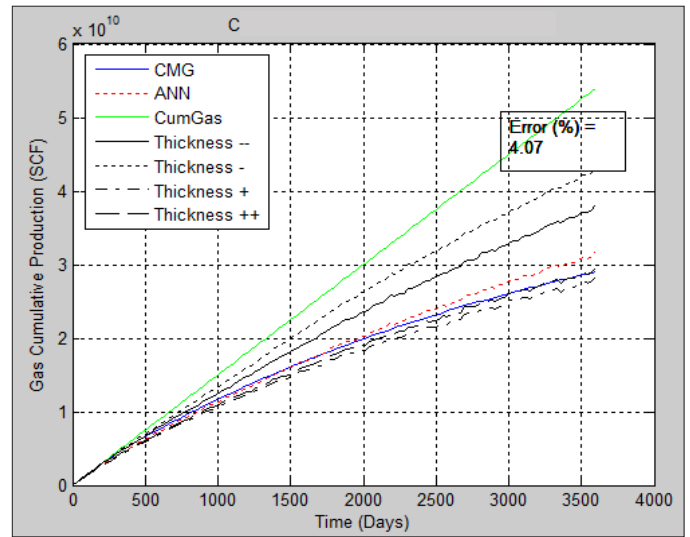
Fig. 14. The FEx-P logical response to reservoir thickness changes. As expected, the higher the reservoir thickness, the higher the cumulative production, and vice versa.
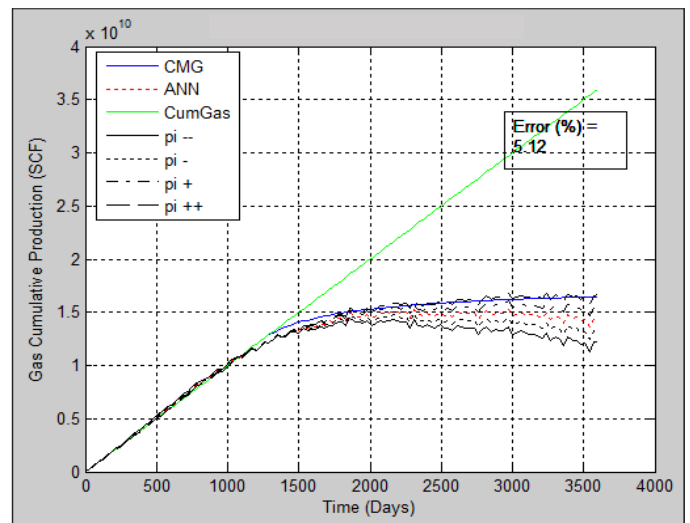

Fig. 15. The FEx-P logical response to initial reservoir pressure changes. As expected, the higher the pi, the longer its time at the end of the plateau, and vice versa.

the second category has an unknown time at the end of the plateau, because its plateau was extended for more than 10 years. All cases in the second category were given a default value of 10 years as the time at the end of the plateau. The introduction of the inaccurate default value of 10 years to all cases in the second category masked the relation between the input parameters and the time at the end of the plateau, which caused the ANN to make erroneous predictions. Therefore, time at the end of the plateau was dropped from the output parameters. Consequently, the accuracy of the predicted

	Original Test Cases	Blind Cases
Average Error (%)	4.06	5.27
Maximum Error (%)	7.14	13.80
Minimum Error (%)	1.52	1.82

Table 11. The original test cases and blind cases errors of the FEx-P

	Base Case 1	**ΔZ -**	**ΔZ - -**	**ΔZ ++**	**ΔZ +**
Area	600	600	600	600	600
Thickness	270	200	150	320	300
Initial Pressure	5,900	5,900	5,900	5,900	5,900
Plateau Rate	15,000,000	15,000,000	15,000,000	15,000,000	15,000,000
Matrix Porosity	0.087	0.087	0.087	0.087	0.087
Fracture Porosity	0.0074	0.0074	0.0074	0.0074	0.0074
Matrix Permeability	3.00E-05	3.00E-05	3.00E-05	3.00E-05	3.00E-05
Fracture Permeability	0.745	0.745	0.745	0.745	0.745
Spacing Fracture	3	3	3	3	3

Table 12. The reservoir thickness practicality test cases of the FEx-P

	Base Case 2	**pi - -**	**pi -**	**pi +**	**pi ++**
Area	200	200	200	200	200
Thickness	105	105	105	105	105
Initial Pressure	5,200	4,800	5,000	5,400	5,600
Plateau Rate	10,000,000	10,000,000	10,000,000	10,000,000	10,000,000
Matrix Porosity	0.063	0.063	0.063	0.063	0.063
Fracture Porosity	0.0018	0.0018	0.0018	0.0018	0.0018
Matrix Permeability	8.00E-05	8.00E-05	8.00E-05	8.00E-05	8.00E-05
Fracture Permeability	0.496	0.496	0.496	0.496	0.496
Spacing Fracture	5	5	5	5	5

Table 13. The initial reservoir pressure practicality test cases of the FEx-P

production profiles has increased significantly. Nonetheless, a straight line representing cumulative plateau production vs. time was introduced to the FEx-P output plots — the green line in Figs. 13, 14, 15 — which allows users to visually estimate the time at the end of the plateau period. Time at the end of the plateau is estimated at the point when the predicted cumulative production profile deviates from the cumulative plateau production line.

Table 11 shows the minimum, maximum, and average prediction errors of FEx-P. The neural network training, the training performance, and the regression plots are not shown in this article, but can be found in the original dissertation[29]. Figure 13 shows two random test cases, where the green straight line represents the cumulative production of a continuous plateau vs. time to allow for visual identification of time at the end of the plateau.

Practicality Test of the FEx-P

A robust expert system, similar to the FEx-P, should capture expected logical response to sensitivities in input parameters. For example, if initial pressure is increased while keeping all other parameters fixed, the accurate response of the expert system should be an increase in the end of the plateau time. If an ANN is overtrained, it would memorize outputs and have low prediction errors during training or validation processes.

Network Type	Feed-Forward with Back Propagation
Number of Hidden Layers	4
Number of Neurons for Hidden Layers	(8, 6, 10, 14)
Number of Case Scenarios	576
Train, Validate, Test Ratio (%)	(75, 24, 1)
Training Function	Trainscg (Scaled Conjugate Gradient)
Transfer Functions	(Tansig, Tansig, Tansig, Tansig)
Learning Function	Learngdm
Performance Function	Msereg (Mean Square Error with Reg.)
Minimum Performance Goal	5E-05
Maximum Number of Validation Increase	1,000
Maximum Number of Training Iterations	8,000
Minimum Gradient Magnitude	1E-06

Table 14. The ANN design parameters of the IWEx-P

Number	Functional Link	Input or Output
FL 1	Total Wellbore Length (mainbore + all laterals)	Input
FL 2	Drainage Area/Total Wellbore Length	Input
FL 3	Plateau Rate — Actual Initial Rate	Input
FL 4	Cumulative Production at End of Year 10 — Actual Initial Rate	Input
FL 5	Cumulative Production at End of Year 10 — Drainage Area	Input

Table 15. The functional links of the IWEx-P

Consequently, they would have higher prediction errors in blind tests and practicality tests. Practicality tests show that the trained ANN understands the effect that each input parameter has on the outputs, and proves that the ANN is not over-strained. Accordingly, a trained ANN that does not respond accurately or logically to sensitivities, would still need more training, and should not be considered as an expert system.

In this section, two random data sets were selected to test for practicality response of the expert system. Reservoir thickness was selected as the sensitivity parameter in the first data set, and initial reservoir pressure was selected as the sensitivity parameter in the second data set. Table 12 shows values of the thickness sensitivities, where two sensitivity cases have lower thickness values than the base case, and two other sensitivity cases have higher thickness values than the base case, while keeping all other parameters fixed. Figure 14 shows the response of the FEx-P to changes in thickness. As expected, the higher the reservoir thickness, the higher the cumulative production, and vice versa.

On the other hand, Table 13 shows values of the initial reservoir pressure (p_i) sensitivities, were two sensitivity cases have lower p_i values than the base case, and two other sensitivity cases have higher p_i values than the base case, while keeping all other parameters fixed. Figure 15 shows the response of the FEx-P to changes in p_i. As expected, the higher the p_i, the longer its time at the end of the plateau, and vice versa.

Inverse Well Architecture Design Expert System — Fixed Plateau Rate (IWEx- P)

Within its training range, and for any given complex well design and any given shale gas reservoir properties, the IWEx-P can accurately and instantaneously propose a complex well design capable of producing user specified cumulative production profiles from the user specified rock properties. The prediction error of the IWEx-P was calculated based on comparing the original — input — production profile against the production profile generated by the proposed complex well design, due to the non-uniqueness of the solution. The ANN design parameters of this expert system are shown in Table 14. The functional links, Table 15, and data manipulation techniques, Table 16, were introduced to the input and output layers during ANN training to reduce the prediction error.

Table 17 shows the maximum, minimum, and average

prediction error of the IWEx-P. The ANN training, training performance, and regression are not shown in this article, but can be found in the original dissertation[29]. Figure 16 shows representative original test cases. In addition, Fig. 17 shows representative blind test cases, where the green straight line represents the cumulative production of a continuous plateau vs. time, to allow for visual identification of time at the end of the plateau.

Inverse Reservoir Rock Properties Expert System — Fixed Plateau Rate (IREx- P)

For any given complex well design and any given three-year cumulative gas production profile, the IREx-P can accurately and instantly predict the corresponding shale gas reservoir property suite. Several ANNs were trained to achieve this goal, but they were not reaching the desired accuracy levels. Further analysis indicated that the root cause of the high closed loop production errors were mainly controlled by parameters such as natural fracture permeability, drainage area, and matrix porosity.

The introduction of a number of functional links and data manipulation techniques that target natural fracture permeability, drainage area, and matrix porosity did not result in a significant reduction in closed loop production error.

Number	Parameter	Input or Output
DM 1	Mainbore Length/54	Input
DM 2	Well Distance from the *j* Boundary/54	Input
DM 3	Well Distance from the *j* Boundary/54	Input

Table 16. The data manipulation techniques of the IWEx-P

	Original Test Cases	Blind Cases
Average Error (%)	2.94	14.64
Maximum Error (%)	8.59	55.61
Minimum Error (%)	0.00	0.81

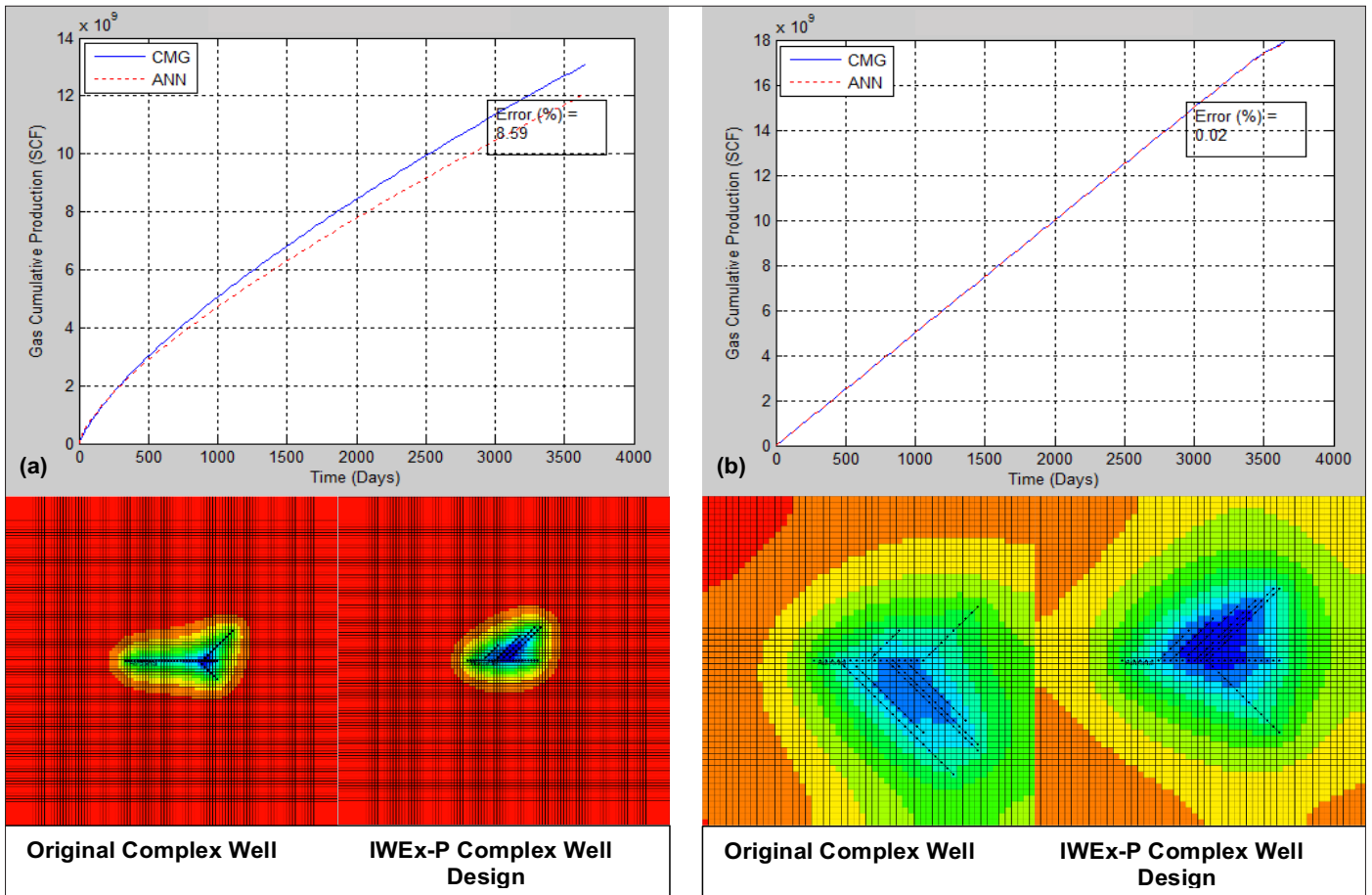Table 17. The original test case and blind case errors for the IWEx-P

Fig. 16. A comparison of the simulation results (a) vs. the forward ANN production predictions (b), using the ANN predicted well design parameters (8.59% and 0.02% error — original test cases).
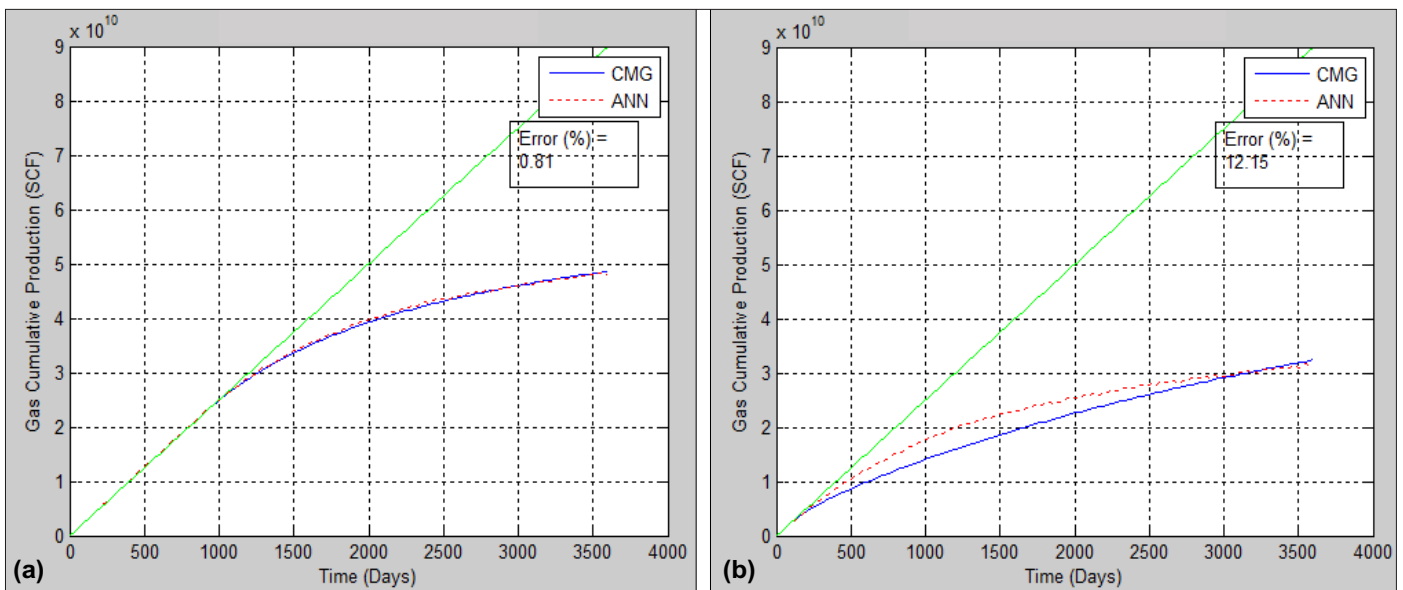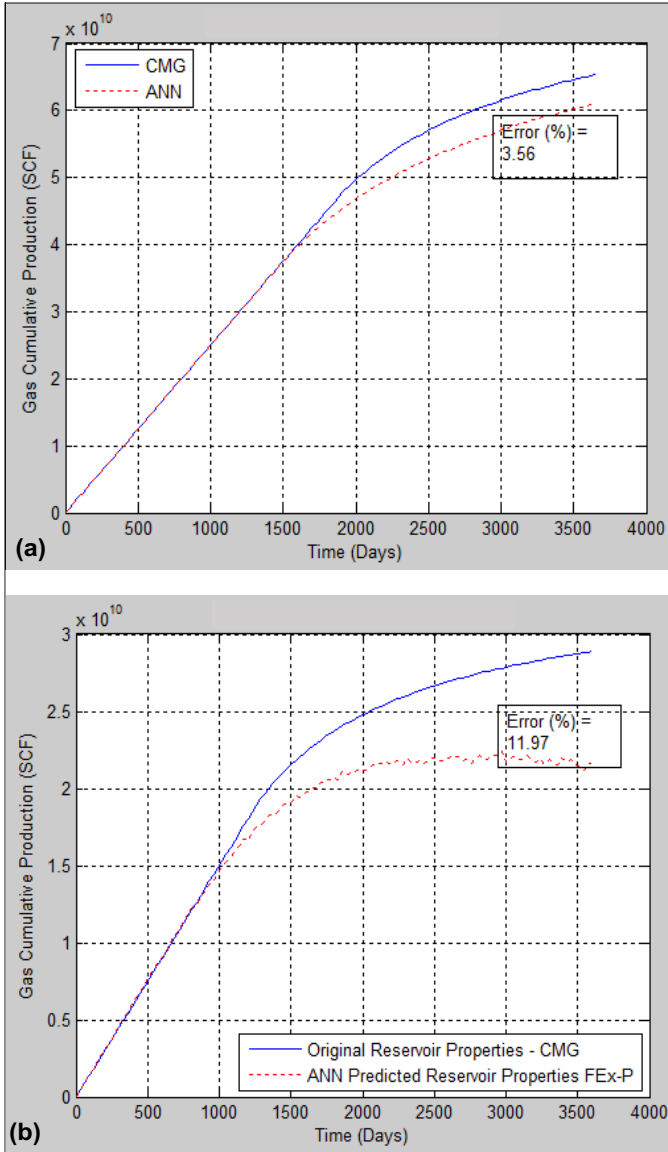

Fig. 17. A comparison of the simulation results (a) vs. the forward ANN production predictions (b), using the ANN predicted well design parameters (0.81% error and 12.55% — blind test cases): (a) shows a good match between the ANN and the simulation, and a time at the end of the plateau of 1,000 days; (b) shows a decent match between the ANN and the simulation, and a time at the end of the plateau of 100 days.

Therefore, a new approach that connects four trained ANNs in a series to form the IREx-P expert system was used. The first ANN predicts the natural fracture permeability; the second ANN predicts the drainage area; the third ANN predicts the matrix porosity, and finally, the fourth ANN predicts all

other rock properties.

The first ANN is trained on the original set of input parameters, and it makes accurate predictions of natural fracture permeability, thereby reducing the closed loop error. The second ANN uses the original input parameters plus natural

	Original Test Cases	Blind Cases
Average Error (%)	4.30	12.79
Maximum Error (%)	9.07	27.99
Minimum Error (%)	1.36	1.86

Table 18. The original test cases errors for the IREx-P.

(a)

(b)

Fig. 18. A comparison of the simulation results (a) vs. the forward ANN production predictions (b), using the ANN predicted reservoir properties (3.56% error — an original test case, and 11.97% error — a blind test case).

fracture permeability values predicted by the first ANN, and makes accurate drainage area predictions — which helps in further lowering the closed loop error. The input parameters in the third ANN are the original input parameters, the natural fracture permeability values predicted by the first ANN, and the drainage area values predicted by the second ANN. The third ANN makes accurate predictions of the matrix porosity. Using this workflow, the three parameters that contribute most to the high close-loop production error are predicted accurately. The fourth ANN predicts the remaining

rock properties by using the original input parameters plus predictions of the first, second, and third ANN.

Table 18 shows the maximum, minimum, and average prediction errors of the IREx-P. The neural network training, the training performance, and the regression plots for all four ANNs used in the IREx-P, are found in the original dissertation[29]. Figure 18 shows representative original and blind test cases.

CONCLUSIONS

The results of the presented expert system, in its forward and inverse prediction modes, prove that a well-trained ANN is capable of making fast and accurate predictions. These results increase confidence in utilizing ANNs to solve petroleum engineering problems. It also opens the door for future work to be conducted. For example, in this work all complex well configurations were varied in the X-Y plain. In future work, the complex well design can be varied in the Z direction where laterals can have an up or down dip. As another example, in this work, a single set of gas properties was used and in future work gas properties could be varied and added as input or output parameters. Finally, results presented in this article increase the level of confidence in using complex wells as an alternative to MHFHWs.

ACKNOWLEDGMENTS

REFERENCES

1. U.S. Energy Information Administration (EIA): "Annual Energy Outlook 2017 with Projections to 2050," January 2017, 127 p. (*http://www.eia.gov/outlooks/aeo/pdf/0383(2017).pdf*).

2. U.S. Energy Information Administration (EIA): "Shale Gas Production Drives World Natural Gas Production Growth," August 2016, (*http://www.eia.gov/todayinenergy/detail.php?id=27512*).

3. U.S. Department of Energy: "Natural Gas from Shale: Questions and Answers," April 2013, 40 p. (*https://energy.gov/sites/prod/files/2013/04/f0/complete_brochure.pdf*).

4. U.S. Energy Information Administration (EIA): "U.S. Natural Gas Gross Withdrawals from Shale Gas," December 2018, (*http://www.eia.gov/dnav/ng/hist/ngm_epg0_fgs_nus_mmcfa.htm*).

5. Holditch, S.A.: "Tight Gas Sands," *Journal of Petroleum Technology*, Vol. 58, Issue 6, June 2006, pp. 86-93.

6. Fisher, M.K., Wright, C.A., Davidson, B.M., Steinsberger, N.P., et al.: "Integrating Fracture Mapping Technologies

to Improve Stimulations in the Barnett Shale," *SPE Production & Facilities*, Vol. 20, Issue 2, May 2005, pp. 85-93.

7. Weng, X., Kresse, O., Cohen, C-E., Wu, R., et al.: "Modeling of Hydraulic-Fracture-Network Propagation in a Naturally Fractured Formation," *SPE Production & Operations*, Vol. 26, Issue 4, November 2011, pp. 368-380.

8. Dahi-Taleghani, A. and Olson, J.E.: "Numerical Modeling of Multistranded Hydraulic Fracture Propagation: Accounting for the Interaction between Induced and Natural Fractures," *SPE Journal*, Vol. 16, Issue 3, September 2011, pp. 575-581.

9. Simonson, E.R., Abou-Sayed, A.S. and Clifton, R.J.: "Containment of Massive Hydraulic Fractures," *Society of Petroleum Engineers Journal*, Vol. 18, Issue 1, February 1978, pp. 27-32.

10. Hossain, M.M., Rahman, M.K. and Rahman, S.S.: "A Shear Dilation Stimulation Model for Production Enhancement from Naturally Fractured Reservoirs," *SPE Journal*, Vol. 7, Issue 2, June 2002, pp. 183-195.

11. Potluri, N.K., Zhu, D. and Hill, A.D.: "The Effect of Natural Fractures on Hydraulic Fracture Propagation," SPE paper 94568, presented at the SPE European Formation Damage Conference, Scheveningen, the Netherlands, May 25-27, 2005.

12. Ouyang, L-B. and Aziz, K.: "A General Single-Phase Wellbore/Reservoir Coupling Model for Multilateral Wells," *SPE Reservoir Evaluation and Engineering*, Vol. 4, Issue 4, August 2001, pp. 327-335.

13. Joshi, S.: "Horizontal and Multilateral Wells: Performance Analysis — An Art or a Science?" *Journal of Canadian Petroleum Technology*, Vol. 30, Issue 10, October 2000, pp. 19-23.

14. Stalder, J.L., York, G.D., Kopper, R.J., Curtis, C.M., et al.: "Multilateral Horizontal Wells Increase Rate and Lower Cost per Barrel in the Zuata Field, Faja, Venezuela," SPE paper 69700, presented at the SPE International Thermal Operations and Heavy Oil Symposium, Porlamar, Margarita Island, Venezuela, March 12-14, 2001.

15. Vento, M. and Durst, D.: "Why Multilateral Cemented Junction Wells Can Help Economics for Development Projects in Oil and Gas Shale Reserves," SPE paper 178171, presented at the SPE/IADC Middle East Drilling Technology Conference and Exhibition, Abu Dhabi, UAE, January 26-28, 2016.

16. Yu, X., Guo, B., Ai, C. and Bu, Z.: "A Comparison between Multifractured Horizontal and Fishbone Wells for Development of Low Permeability Fields," SPE paper 120579, presented at the SPE Asia Pacific Oil and Gas Conference and Exhibition, Jakarta, Indonesia, August 4-6, 2009.

17. Iktissanov, V.A.: "Pressure Transient Analysis and Simulation of Nonconventional Wells," SPE paper 133477, presented at the SPE Russian Oil and Gas Conference and Exhibition, Moscow, Russia, October 26-28, 2010.

18. Jordan, C.L., Waeyan, B., Smith, C.R. and Jackson, R.: "An Alternative Method for Horizontal and Multilateral Pressure Transient Analysis," paper 2009-022, presented at the Offshore Mediterranean Conference and Exhibition, Ravenna, Italy, March 25-27, 2009.

19. Garrouch, A.A., Lababidi, H.M.S. and Ebrahim, A.: "A Novel Expert System for Multilateral Well Completion," SPE paper 83474, presented at the SPE Western Regional/AAPG Pacific Section Joint Meeting, Long Beach, California, May 19-24, 2003.

20. Yeten, B., Durlofsky, L.J. and Aziz, K.: "Optimization of Nonconventional Well Type, Location, and Trajectory," *SPE Journal*, Vol. 8, Issue 3, September 2003, pp. 200-210.

21. Bukhamsin, A.Y., Farshi, M.M. and Aziz, K.: "Optimization of Multilateral Well Design and Location in a Real Field Using a Continuous Genetic Algorithm," SPE paper 136944, presented at the SPE/DGS Annual Technical Symposium and Exhibition, al-Khobar, Saudi Arabia, April 4-7, 2010.

22. Hari, D., Ertekin, T. and Grader, A.S.: "Methods of Neuro-Simulation for Field Development," SPE paper 39962, presented at the SPE Rocky Mountain Regional/Low-Permeability Reservoirs Symposium, Denver, Colorado, April 5-8, 1998.

23. Al-Fattah, S.M. and Startzman, R.A.: "Neural Network Approach Predicts U.S. Natural Gas Production," SPE paper 67260, presented at the SPE Production and Operations Symposium, Oklahoma City, Oklahoma, March 24-27, 2001.

24. Zargari, S. and Mohaghegh, S.D.: "Field Development Strategies for Bakken Shale Formation," SPE paper 139032, presented at the SPE Eastern Regional Meeting, Morgantown, West Virginia, October 13-15, 2010.

25. Te Stroet, C., Zwaan, J., de Jager, G., Montijn, R., et al.: "Predicting Sweet Spots in Shale Plays by DNA Fingerprinting and Machine Learning," URTEC paper 2671117, presented at the SPE/AAPG/SEG Unconventional Resources Technology Conference, Austin, Texas, July 24-26, 2017.

26. Kormaksson, M., Vieira, M.R. and Zadrozny, B.: "A Data Driven Method for Sweet Spot Identification in Shale Plays Using Well Log Data," SPE paper 173455, presented at the SPE Digital Energy Conference and

Exhibition, The Woodlands, Texas, March 3-5, 2015.

27. Hagan, M.T., Demuth, H.B. and Beale, M.H.: *Neural Network Design*, 1st edition, Boston, MA: PWS Pub., 1996.

28. Alqahtani, M.H. and Ertekin, T.: "Shale Gas Reservoir Development Strategies Using Complex Specified Bottom-hole Pressure Well Architectures," SPE paper 188144, presented at the SPE Kingdom of Saudi Arabia Annual Technical Symposium and Exhibition, Dammam, Saudi Arabia, April 24-27, 2017.

29. Alqahtani, M.H.: "Shale Gas Reservoirs Development Strategies Via Advanced Well Architectures," Ph.D. Dissertation in Petroleum and Natural Gas Engineering, Pennsylvania State University, University Park, Pennsylvania, 2015.

BIOGRAPHIES
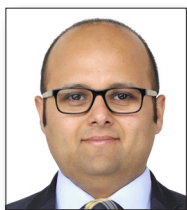
Dr. Mari H. Alqahtani is the Zuluf Unit supervisor of Saudi Aramco's Northern Area Reservoir Management Department. During his career, he has held several positions with Saudi Aramco, including Facilities Engineer, Economics Evaluator, Reserves Estimator, Senior Reservoir Engineer, and Deputy Team Leader of Integrated Reservoir Studies.

Mari holds a U.S. patent in Offshore Recovery Enhancement Mechanism.

He has been an active member of the Society of Petroleum Engineers (SPE) since 2003. In 2014, Mari was elected as the SPE Graduate Students' Representative of the SPE Penn State Chapter. In 2017, he was the Annual Technical Symposium & Exhibition (ATS&E) pre-Events Courses and Workshops co-Chairman. In 2018, Mari was the ATS&E Technical Program co-Chairman. Currently, he is the Assistant to the 2020 International Petroleum Technology Conference (IPTC) Program Chairman.

Mari received his B.S. degree in Petroleum and Natural Gas Engineering (with honors) in 2005 from West Virginia University, Morgantown, WV. In 2010, he received his M.S. degree in Petroleum Engineering from Texas A&M University, College Station, TX. Mari's research area was in the development of offshore oil fields. In 2015, he received his Ph.D. degree in Petroleum Engineering from Pennsylvania State University, State College, PA, where his research area was in artificial intelligence applications in shale gas development.

During his tenure at Penn State, Mari was a technical reviewer for the *Journal of Petroleum Exploration and Production Technology*.

Prof. Turgay Ertekin is a Professor of Petroleum and Natural Gas Engineering and Head of the John and Willie Leone Family Department of Energy and Mineral Engineering at Pennsylvania State University. He is also the holder of the George E. Trimble Chair in Earth and Mineral Sciences at the university. Turgay's main research area is mathematical modeling of fluid flow dynamics in porous media and implementation of artificial intelligence technology with respect to various reservoir engineering process analyses.

He is a recipient of several Society of Petroleum Engineers (SPE) international awards, including the 1998 Distinguished Achievement Award for Petroleum Engineering Faculty, the 2001 Lester C. Uren Award for Distinguished Achievement in the Technology of Petroleum Engineering, the 2001 SPE Distinguished Member Award, and the 2013 SPE Honorary Membership Award.

At Penn State, Turgay has received the College of Earth and Mineral Sciences' Teaching, Research, Service, and Mentorships awards and also the university's Graduate School Teaching Award.

For a two-year period, he served as the Executive Editor of the *SPE Formation Evaluation Journal* and he currently is serving as Editor-in-Chief for the *Journal of Petroleum Exploration and Production Technology*.

Turgay received his B.S. and M.S. degrees in Petroleum Engineering from the Middle East Technical University, Ankara, Turkey, and his Ph.D. degree in Petroleum and Natural Gas Engineering from Pennsylvania State University, State College, PA.

Sultan M. Almalki is a Petroleum Engineer working in the Gas Reserves Group of Saudi Aramco's Upstream Development Strategy and Reserves Department. He began his career with Saudi Aramco in 2010, working as a Reservoir Simulation Engineer, and then as a Petrophysicist. Sultan then went on an assignment with Halliburton in the United States, focusing on evaluating unconventional resources. He has been also part of several integrated reservoir studies.

Sultan has extensive experience in 3D reservoir modeling, reservoir simulation, petrophysics, unconventional resources evaluation, and oil and gas reserves estimation.

He is an active member of the Society of Petroleum Engineers (SPE), and in 2016, Sultan was selected to be the e-Media and Publicity Chairperson. In 2018, he was recognized for his work with SPE by being awarded the prestigious SPE Century Club Award.

In 2010, Sultan received his B.S. degree (with honors) in Petroleum Engineering from the University of Manchester, Manchester, U.K.

Holistic Evaluation of Water Cut in High GOR Wells for Better Production Management

Mohammad S. Al-Kadem, Dr. Dhafer A. Al-Shehri, Dr. Mohamed Mahmoud, and Dr. Rahul N. Gajbhiye

ABSTRACT

Water cut measurement becomes essential in fields where there is significant water production, especially when combined with gas production, making the measurement of all three phases difficult. In other words, water cut measured values are affected by the presence of gas near the surface. Therefore, the objective of this study is to estimate the water cut in high gas-oil ratio (GOR) wells with values greater than 2,000 standard cubic ft/stock tank barrel (scf/stb)[1].

One of the trusted methods in measuring water cut is the multiphase flow meter (MPFM). This equipment gives accurate and reasonable values at typical conditions where there are no flow assurance issues at the surface such as free gas, slug, or emulsions. It is worth mentioning that there are very limited MPFMs applicable for a high GOR environment. A model was developed with various inputs combined from downhole and surface sections of the well to better calculate water cut where free gas exists, obtaining these parameters on a real-time basis.

Analytical and empirical models are available in the literature to provide an accurate estimation of water cut at various conditions. The developed artificial neural network (ANN) model was compared to existing models with similar applications. It was also validated against actual measurements from existing test separators and wellhead samples. The average absolute percentage error obtained upon comparing the developed model to the examined ones, and the actual values, was significantly reduced to 4.2%. This drastic improvement in water cut estimation was due to the use of a wide range of surface and subsurface parameters, provided that they are attained on a real-time basis.

The leverage of knowing the correct water cut is quite imperative to better manage reservoirs in the case of abnormal conditions such as a high GOR. There are few MPFMs in the industry that are applicable for high GOR wells, but not yet trial tested, thereby providing an opportunity for the engineer to have a practicable model to estimate water cut on a real-time basis.

INTRODUCTION

Water cut measurement becomes essential in fields with high water production. Oil companies tend to produce oil, and to maximize recovery, avoid the excessive production of water. This mandates monitoring the water cut during the early life of the well. To avoid a scenario of producing unnecessary water, an accurate measurement of the water cut is attained. Nevertheless, water cut is a very important input in designing the surface facilities at the early stage of the field. Surface facilities, including water and gas handling or processing equipment, are designed based on predefined calculations of the water cut and gas-oil ratio (GOR).

As a key parameter, the water cut measurement is important when the reservoir pressure is lower than the bubble point pressure, where gas can cause major errors in measurement rates and the water cut measurement. An inaccurate input value of water cut might underestimate or overestimate the capital expenditure (CAPEX), which might require an unexpected upgrade of the handling facilities at a later stage of field production. Figure 1 shows the impact of water production on the required capital expenditure for processing high volumes of water and gas[2]. Also, another observation is that it is more expensive to treat water, with a minor additional cost to treat gas. For this reason, water cut was considered as the calculation output rather than gas because a water processing facility has more impact on capital expenditure than a gas processing facility.
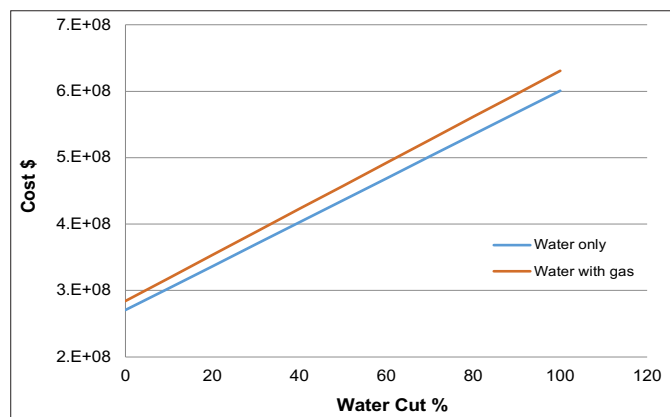

Fig. 1. The impact of water and gas production on facility costs[2].

The importance of water cut measurement is not limited to the design of the surface facilities, but is also a critical parameter to manage reservoirs. An accurate measurement will enable decision makers to provide advice to shut-in or sidetrack wells with high water cuts, thereby maintaining oil production in the field. Also, reservoir simulation will require an accurate water cut measurement as an input to ensure the precision of the simulation model for engineers to forecast field production, and advise on any additional required action that would sustain or enhance the oil recovery.

Monitoring the water cut could lead to maximizing recovery instead of maximizing production, thereby jeopardizing the health of the reservoir. There are available technologies and software to monitor water cut on a real-time basis with the objective of maximizing the recovery, avoiding the need of considering secondary or tertiary enhanced oil recovery.

Another important aspect of water cut measurement in high GOR wells is to explore the flow assurance problems when producing high water and gas volumes at the surface. Two flow issues are addressed as:

1. High water/gas production might cause corrosion: Chemical corrosion is caused by soluble organic acids within the produced formation water or carbon dioxide within gas in the reservoir. These components react with the metal and cause severe pitting.

2. When there is a high GOR produced at the surface, line pressure drop increases, which lowers oil production, exerting a high backpressure on the surface line, Fig. 2[3].

More sensitivity analysis was performed to study high water cut and high GOR on an inflow performance relationship, and a tubing performance relationship model. The forces affecting the tubing performance relationship curve are:

$$P_{wf} = f(P_{wh}, \Delta P_f, \rho gh) \qquad (1)$$

where P_{wf} is the flowing bottom-hole pressure, P_{wh} is the
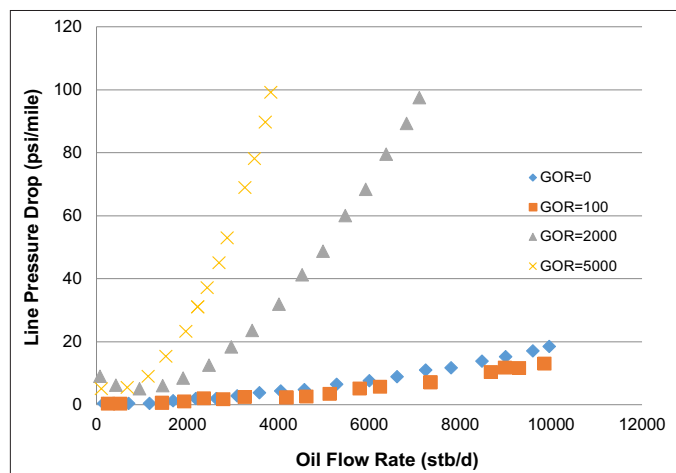
Fig. 2. Impact of a high GOR on line pressure drop[3].

Reservoir Type	GOR
Black Oil	< 2,000
Volatile Oil	2,000 to 3,300
Gas Condensate	3,300 to 50,000

Table 1. Classification of reservoirs based on GOR

flowing wellhead pressure, ΔP_f is the pressure drop due to friction, and ρgh is the hydrostatic component.

Referring to the hydrostatic component, density is highly affected by the presence of high water production or/and high GOR.

A GOR of more than 2,000 standard cubic ft/stock tank barrel (scf/stb) is considered in this article[1] for reservoir types. The type of reservoir that is addressed in this article is considered to be volatile oil based on the standard classification of reservoirs based on the GOR in Table 1.

WATER CUT METERING TECHNOLOGIES

A Microwave-based Water Cut Monitoring Technology

A device was developed to measure water cut using microwave signals[4]. This is a cost-effective technology where it accounts for oil composition, temperature variation, water salinity, crude properties, and water conductivity. It is a compact system and requires a small footprint. Microwave signals transmitted through a reflection area from fluids are based on strong polarity, which shows that there is high permittivity due to the strong electrical energy where water has a polarity larger than oil. The drawback of this technology is that it will measure water cut inaccurately when there is free gas at the surface, and also when emulsion is taking place at the surface.

Magnetic Inductive Flow Multiphase Meter

A magnetic inductive flow multiphase meter has a partial separation separator to separate liquid from gas and a Coriolis flow meter[5]. This meter was developed for high GOR applications. It can measure wells rates from 100 barrels per day (bpd) to 15,000 bpd, and with a GOR up to 80,000 scf/stb. The measurement is based on a microwave technology where fractions of flow rates in the pipe are measured. The accuracy of oil rate is 5%, and the gas rate is 1% to 2%.

Portable Multiphase Production Tester

This is a portable multiphase flow meter (MPFM) with a gas volume fraction range from 10% to 20% for high water cut applications[6]. A water cut meter is one of the meter components that is not affected by salinity, and is insensitive to low entrapped gas. It can also measure high oil flow rates and high water cut.

Weatherford Water Cut Meter

This meter is a Weatherford water cut meter, which has two components: a water cut monitoring sensor, and Coriolis flow meter[7]. The measurement is independent of density changes, but is applicable for a low GOR — up to 550 scf/stb, and a water cut of 5% to 42%. The infrared meter measures water cut based on near infrared absorption spectroscopy[8] where water absorbs large amounts of electromagnetic energy. This meter provides a real-time measurement, whereas accuracy and the availability of real-time measurements can lead to corrective action in a timely manner.

Trial Test of Multiple MPFMs

MPFM technology has been rolled out in the industry for the past 20 years[9]. There is no such MPFM that operates with a high GOR and high volume fraction of more than 95%. Three MPFMs were trial tested for multiple wells with a high GOR, but none of them succeeded. Liquid rates at high gas volume fraction started to diverge because uncertainty starts to increase, due to the rapid change of flow regimen; mist, and annular at high gas fraction; which also affects the oil rates.

Permanent Downhole Water Cut Measurement

This article addresses various techniques for the permanent downhole water cut measurements[10]:

- Relative permittivity where there is a high polarity or permittivity for water.
- Near infrared where water absorbs more energy at higher wavelengths.
- Time domain transmissometry, where it measures the transmission through water, oil, or gas, where transmission is slower in water due to high density.
- The Coriolis Effect, where water has the minimum oscillation frequency.
- Gamma ray absorption for radioactive meters, where the produced water has higher radioactivity than oil or gas.

These techniques are for oil applications where a low GOR is encountered. They are compared based on environmental impact, equipment reliability, measurement accuracy, and power requirements.

Technology of Optimization of Production of Liquid Hydrocarbons from Reservoirs Containing Oil or Condensate with High GOR

A new technology for testing wells with a high GOR is called Technology for the Optimization of Production (TOP). This

technology is basically a pressure regulator installed downhole along the tubing to control the condensate production for high GOR wells[11]. This regulator controls the flowing bottom-hole pressure (P_{wf}), to keep it at the optimum pressure at which gas is kept in the condensate and reduces the condensate flow, while also maintaining the P_{wf} to avoid any unnecessary reduction. The range of applicability of GOR is up to 5,000 scf/stb.

High Gas ABB VIS MPFM

An ABB Group vega isokinetic sampling MPFM is a non-gamma meter that measures individual oil, water, and gas rates for wells with a high gas volume fraction of more than 90%[12]. The article explained a compact system of this metering technology where liquid and gas are then measured separately as single phases with considerable accuracy with no calibration required. Overall flow rates are calculated through the sampling ratio, i.e., the ratio between the probe and the pipe areas, and the gas flow rate is measured separately using a venturi meter as part of the MPFM body. The accuracy of this meter measurement can reach up to ± 5% in water cut, yet this meter has not been trial tested in the field.

WATER CUT ESTIMATION MODELS

High GOR Wells Optimization

Empirical observations, tools and examples are demonstrated in gas handling for oil wells[13]. Wells with the average GOR of 17,000 scf/stb were studied and optimized. Wells with high GOR were classified into two categories; restricted (choked back) and unrestricted. Also, challenges of excessive water, gas, and solutions were explored. Environmental impacts due to flaring gas were assessed when the design of gas processing facilities were underestimated.

A Model for Predicting Water Cut in Oil Reservoirs

This article proposed a new model for forecasting water cut considering exponential analysis (Arps) where many variables are constant[14]. Five models were discussed: Ershaghi-Omoregie, Liu, Warren, Purvis, and Lawal. The models with their corresponding equations are listed next.

Utilization of Downhole Sensor Data to Estimate Water Cut

Three published papers[15-17], developed an analytical method to estimate rates and water cut using real-time data from electric submersible pump (ESP) downhole pressure and temperature sensors. The range of applicability in the GOR was targeted for black oil applications. Also, this method is applicable for wells with ESPs only.
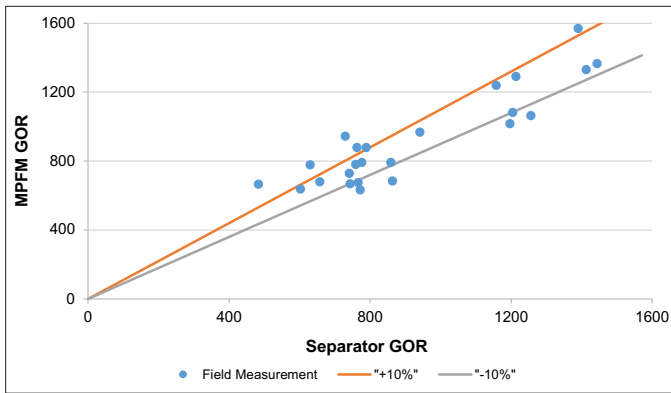
Fig. 3. Comparison between the separator GOR and the MPFM GOR of less than 2,000 scf/stb.
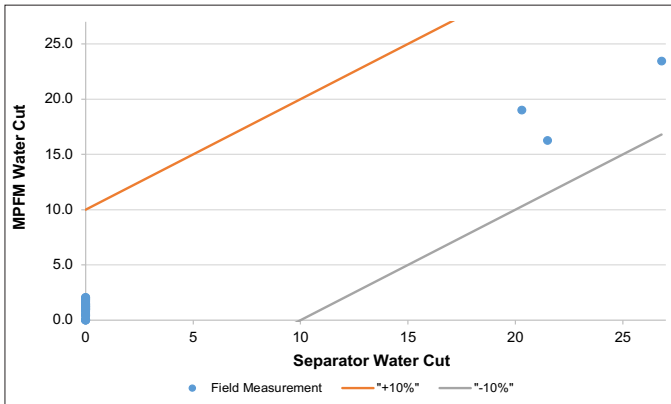

Fig. 4. Comparison between the separator water cut and the MPFM water cut for a GOR of less than 2,000 scf/stb.

Horizontal Well Water Cut Estimation due to Water Coning

Water cut in horizontal wells is indescribable by analytical models for homogeneous reservoirs. A new model is proposed using a statistical variogram as the best fit model between the water cut and the recovery factor in horizontal wells[18]. The modeled variogram is a function of reservoir dip angle, oil column thickness, well construction, and permeability anisotropy. The model was addressed to oil applications only.

STUDY MOTIVATION

Little Work Done to Estimate Water Cut for High GOR

Based on the literature review in the previous section, little work was focusing on estimating water cut in high GOR wells. One technology, magnetic inductive flow meter, was examined for high GOR wells — GOR up to 80,000 scf/stb — with high accuracy in the water cut and rates measurement. Another technology was discussed, TOP, which is a pressure regulator to control the excessive production of condensate in high GOR wells. A model for classifying and assessing wells with a high GOR was developed to better optimize the wells' oil production and avoid condensate production.

Limited Meter Technology for High GOR Wells

One of the conventional methods in measuring water cut is the MPFM. This equipment gives accurate and reasonable values at typical conditions, however, they do not perform well at certain conditions. There is no such MPFM applicable for high GOR environments. MPFMs measure inaccurate water cut, but measure oil rate in isolation of the MPFM. It will be a considerable addition to the industry when coming out with a new methodology that fills that gap. Despite this fact, there are issues associated with the MPFM, such as the limited number of manufacturers, equipment pricing, and use of radioactive sources. Also considering the MPFM as a conventional metering technology, it requires frequent calibration and maintenance, whereas having a model, calibration will not be an issue.

The MPFM measures flow rates in all phases, water cut, and GOR with considerable accuracy at a GOR of less than 2,000 scf/stb. Figures 3 and 4 are a comparison between the conventional test separator and the MPFM readings for GOR and water cut, respectively[9]. Both GOR and water cut are falling within the acceptable error band of ±10%.

In contrast, wells with a GOR of greater than 2,000 scf/stb were tested using both a test separator and the MPFM. At a
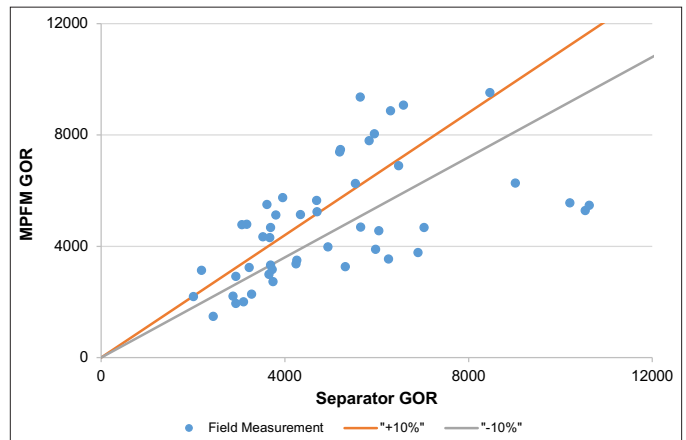

Fig. 5. Comparison between the separator's GOR and the MPFM's GOR when greater than or equal to 2,000 scf/stb.
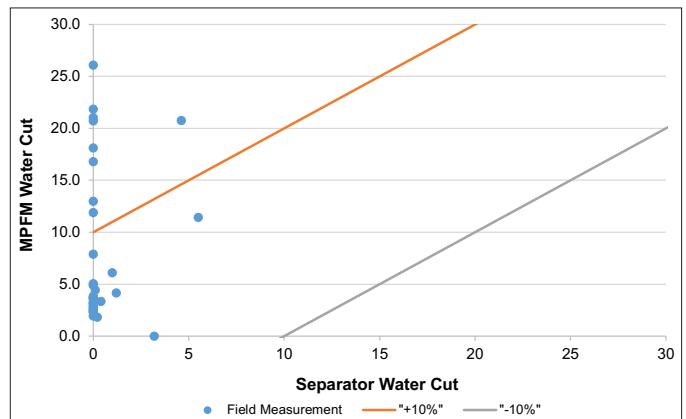

Fig. 6. Comparison between the separator's water cut and the MPFM's water cut for a GOR greater or equal to 2,000 scf/stb.

GOR >2,000 scf/stb, the deviation between the MPFM's GOR and the test separator's GOR was more than ±10% in terms of absolute error, Fig. 5[9]. Nevertheless, this also impacts the water cut readings, where the MPFM is failing to measure the water cut accurately at a high GOR, Fig. 6[9]. Therefore, a high GOR affects the rate measurement and water cut values, thereby confirming that there are no MPFMs certified for high GORs.

NEW METHODOLOGY

The following steps summarize the methodology in a nutshell.

1. Proposed steps estimate the water cut:

   - Gather data for low and high GOR wells.
   - Compare actual water cut with existing multiphase flow correlations.
   - Develop the ANN model.
   - Select the most appropriate model that achieves the least errors, and cover the whole range of the GOR.
   - Verify the optimized ANN model with a new set of data.

2. Data types required to estimate the water cut:

   - The dynamic data that are based on real-time frequency.
   - The upstream and downstream wellhead pressure or temperature.
   - The inflow control valve pressure.
   - The downhole gauge's pressure and temperature.
   - The choke valve position.

3. Static data to model the inflow performance relationship and TPR curves:

   - Pressure, volume, temperature.
   - Reservoir data such as permeability, pressure, temperature, skin, etc.
   - Wellhead samples.

RESULTS AND DISCUSSION

There were 100 wells with a total of 1,210 data points included in this research representing 48 wells with a GOR of less than 2,000 scf/stb, and 52 wells with a GOR greater or equal to 2,000 scf/stb. Initially, data was collected for nine inputs. The random Forest technique was used to select the most important parameters with respect to water cut. After implementing the subject technique, the number of inputs were reduced to five: (1) upstream flowing wellhead pressure, (2) downstream flowing wellhead pressure, (3) GOR, (4) oil

flow rate, and (5) downhole gauge pressure. The ANN model was then developed and optimized to get the most accurate and reasonable results. Table 2 shows the final optimized ANN model.

Figures 7 to 9 shows the training, testing, and overall results for the optimized ANN model, respectively.

Table 3 reflects the error analysis resulting from running the ANN model with five inputs. Overall error, E_{ar}, is 8.13%, which is a less than acceptable error of 10%. Also, the absolute error, E_{aa}, is less than 5%, which demonstrates the accuracy of the developed model with only five inputs.

The ANN model equation can be written as:

$$WC = [\sum_{i=1}^{N} w_{2i} * satlins(w_{1i,j}x_j + b_{1i})] + b_2 \qquad (2)$$

where w is noted for weights and b for biases.

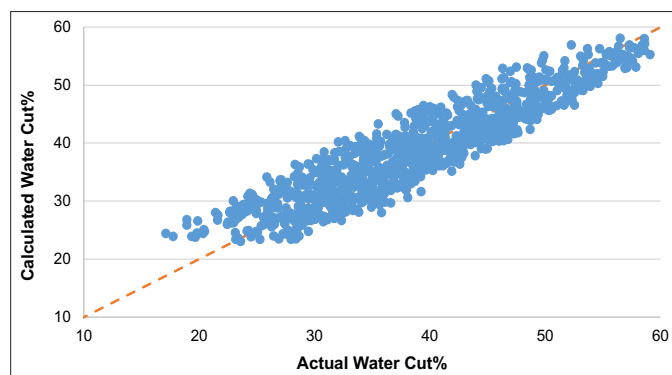| # of Inputs	5
# of Outputs	1
Training Function	Levenberg-Marquardt (trainlm)
# of Hidden Layers	1
Transfer Function	Symmetric Saturating Linear (satlins)
# of Neurons in Input Layer	5
# of Neurons in Hidden Layer	20
# of Neurons in Output Layer	1

Table 2. Final optimized ANN model

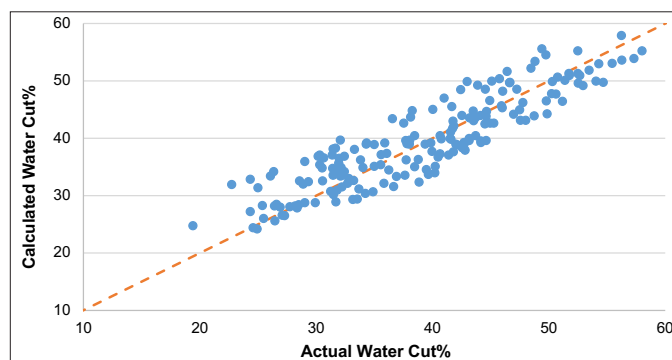Fig. 7. Optimized ANN model; training results.
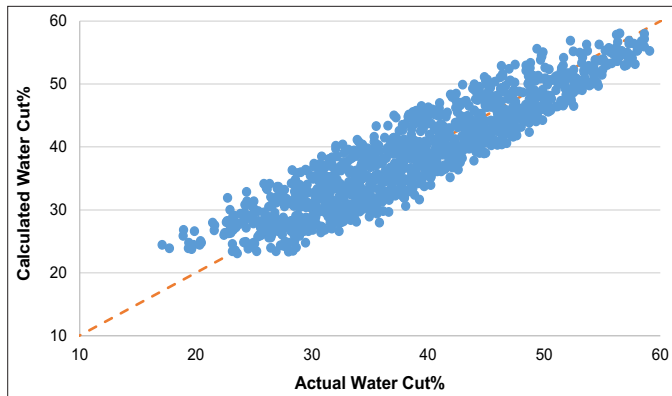

Fig. 8. Optimized ANN model; testing results.

Fig. 9. Optimized ANN model; overall results.

Stage	E_{ar}%	E_{aa}%	CC	R^2
Training	8.1129	2.9153	0.92	0.85
Testing	8.2523	3.0232	0.90	0.81
Overall	8.1339	2.9315	0.92	0.84

Table 3. Statistical error analysis

CONCLUSIONS

1. "Threat to Validity," models developed in this research are applicable to data ranges and boundaries.

2. A combination of real-time data and static data was used to accurately estimate water cut in high GOR wells.

3. The ANN technique proves its high accuracy for estimating water cut with a minimum error rate with a provided set of data, where it can be used as an alternative tool to estimate water cut when measurement devices, such as the separator, go down or require maintenance.

4. Also, the ANN model with nine inputs showed results with an average E_{ar}% of 8.18% against an error attained of 8.13% when using the ANN model with five inputs. This makes no significant difference when using either five or nine inputs, as the selected five inputs are the most important variables from the Random Forest technique.

5. Moreover, the ANN model was also verified with another set of data and resulted in an error of 7.72%, which confirms the robustness of the model.

ACKNOWLEDGMENTS

REFERENCES

1. McCain Jr., W.D.: *The Properties of Petroleum Fluids*, 2nd edition, PennWell Publishing Company, Tulsa, Oklahoma, 1990, 548 p.

2. Macro Trends: "Crude Oil vs. Gasoline Prices — 10 Year Daily Chart," retrieved January 2018, from *http://www.macrotrends.net*.

3. Moshfeghian, M.: "Impact of Gas-Oil Ratio (GOR) on Crude Oil Pressure Drop in Gathering Systems," PetroSkills online, 2014, retrieved March 2018, from *http://www.jmcampbell.com/*.

4. Hatton, G.J., Helms, D.A., Marrelli, J.D. and Durrett, M.G.: "A New Microwave-based Water Cut Monitor Technology," OTC paper 6426, presented at the Offshore Technology Conference, Houston, Texas, May 7-10, 1990.

5. Cellos, H. and Wee, A.: "Multiphase Flow Measurement System of High-GOR Applications," SPE paper 54605, presented at the SPE Western Regional Meeting, Anchorage, Alaska, May 26-27, 1999.

6. Oglesby, K.D., Mehdizadeh, P. and Rodger, G.J.: "Portable Multiphase Production Tester for High Water Cut Wells," SPE paper 103087, presented at the SPE Annual Technical Conference and Exhibition, San Antonio, Texas, September 24-27, 2006.

7. Al-Mutairi, A.R., Khuzzan, S.H., Helal, R. and Raman, B.: "Enhancing Well Testing Performance by Installing a Reliable Water Cut Meter Along with Coriolis Flow Meter," SPE paper 149117, presented at the SPE/DGS Saudi Arabia Section Technical Symposium and Exhibition, al-Khobar, Saudi Arabia, May 15-18, 2011.

8. Al-Saiyed, M.A., Warsi, S.A., Phillips, J.E., Gilani, S.K.M., et al.: "Measurement of Water Cut in Challenging Flow Conditions Using Infrared Technology," SPE paper 118038, presented at the Abu Dhabi International Petroleum Exhibition and Conference, Abu Dhabi, UAE, November 3-6, 2008.

9. Nasri, A., Al-Anizi, A., Al-Amri, M.A., Al-Khelaiwi, F.T., et al.: "Multiphase Flow Meters Trial Testing in High GOR/GVF Environment," IPTC paper 17422, presented at the International Petroleum Technology Conference, Doha, Qatar, January 19-22, 2014.

10. Arsalan, M., Ahmad, T.J., Black, M.J. and Noui-Mehidi, M.N.: "Challenges of Permanent Downhole Water Cut Measurement in Multilateral Wells," SPE paper 177665, presented at the Abu Dhabi International Petroleum Exhibition and Conference, Abu Dhabi, UAE, November 9-12, 2015.

11. Tseytlin, S., Tseytlin, D., Makarian, T. and Petrossov, V.: "New Technology of Optimization of Production of Liquid Hydrocarbons from Reservoirs Containing Oil or Condensate with High GOR and Oil Fringes of the Gas Formations (Russian)," SPE paper 181951, presented at the SPE Russian Petroleum Technology Conference and Exhibition, Moscow, Russia, October 24-26, 2016.

12. Genolini, M.: "High Gas Multiphase Flow Meter (MPFM)," ABB presentation, 2016, retrieved March

2018, from *https://library.e.abb.com.*

13. Peruzzi, T. and Krumanocker, E.: "High GOR Wells Optimization, Prudhoe Bay Practice," SPE paper 54634, presented at the SPE Western Regional Meeting, Anchorage, Alaska, May 26-27, 1999.

14. Li, K., Ren, X., Li, L. and Fan, X.: "A New Model for Predicting Water Cut in Oil Reservoirs," SPE paper 143481, presented at the SPE EUROPEC/EAGE Annual Conference and Exhibition, Vienna, Austria, May 23-26, 2011.

15. Camilleri, L.A.P. and Zhou, W.: "Obtaining Real-Time Flow Rate, Water Cut, and Reservoir Diagnostics from ESP Gauge Data," SPE paper 145542, presented at the Offshore Europe Conference, Aberdeen, Scotland, U.K., September 6-8, 2011.

16. Al Enezi, S.M., Warlick, M.L., Almusabeh, M.I. and Kaba, A.A.: "Forecasting and Monitoring Water Cut Utilizing ESP Pump Discharge Pressures and Fluid PVT Analysis," SPE paper 160886, presented at the SPE Saudi Arabia Section Technical Symposium and Exhibition, al-Khobar, Saudi Arabia, April 8-11, 2012.

17. Al-Amri, M.A., Al-Khelaiwi, F.T. and Al-Kadem, M.S.: "Advanced Utilization of Downhole Sensors for Water Cut and Flow Rate Estimation," SPE paper 161063, presented at the Abu Dhabi International Petroleum Conference and Exhibition, Abu Dhabi, UAE, November 11-14, 2012.

18. Safin, D.A., Korobkin, A.P. and Sitnikov, A.N.: "Horizontal Well Water Cut Estimation due to Water Coning in Heterogeneous Formations with Vertical Flow Barriers (Russian)," SPE paper 182047, presented at the SPE Russian Petroleum Technology Conference and Exhibition, Moscow, Russia, October 24-26, 2016.

BIOGRAPHIES

Mohammad S. Al-Kadem is a Petroleum Engineer working with the Northern Area Intelligent Field Team of Saudi Aramco's Northern Area Production Engineering and Well Services Department. Since joining Saudi Aramco in 2011, he has worked in two development assignments; the Production & Facilities Development Department and the Northern Reservoir Management Department in 2012 & 2014, respectively.

Mohammad is an active member of the Society of Petroleum Engineers (SPE). He was awarded with SPE certification in 2014. Mohammad is an author and/or a coauthor of 15 papers pertaining to his field of specialization.

In 2018, he received his M.S. degree in Petroleum Engineering from King Fahd University of Petroleum and Minerals (KFUPM), Dhahran, Saudi Arabia.

Also as part of his self-development, Mohammad earned the Saudi Aramco Lean Six Sigma Green Belt Certification in 2018.

Dr. Dhafer A. Al-Shehri is the Chairman of the Petroleum Engineering Department and a faculty member within the College of Petroleum Engineering and Geosciences at King Fahd University of Petroleum and Minerals (KFUPM), Dhahran, Saudi Arabia. Prior to this position, he worked at Saudi Aramco from 1996 to 2014, gaining experience in drilling, production, reservoir management, and applied research.

Overall, Dhafer has more than 30 years of experience in the oil and gas industry, as well as academic experience. This includes work in several technical and management positions with upstream operations, and engineering and research capacities.

He is an active member of the Society of Petroleum Engineers (SPE) and served on many committees, including chairing the SPE Technical Symposium, and also was a keynote speaker in several SPE workshops. Dhafer has authored many conference and journal papers. He is also a member in several professional societies.

In 1983, Dhafer received his B.S. degree, and in 1987, he received his M.S. degree — both in Petroleum Engineering — from KFUPM. In 1994, Dhafer received his Ph.D. degree in Petroleum Engineering from Texas A&M University, College Station, TX.

Dr. Mohamed Mahmoud is an Associate Professor working in the Petroleum Engineering Department with King Fahd University of Petroleum and Minerals (KFUPM), Dhahran, Saudi Arabia. Prior to assuming this position in 2016, he had been a Research Assistant in the same department since 2008.

From 2004 to 2008, Mohamed worked as a Petroleum Engineer at Belayim Petroleum Co. in Egypt. During the period from 2001 to 2004, he was a Drilling Engineer at Magawish Petroleum Co., Egypt.

Mohamed's research interests are varied and cover several subjects, including well simulation, enhanced oil recovery, and multiphase flow in vertical and horizontal wells.

He received his Ph.D. degree in Petroleum Engineering from Texas A&M University, College Station, TX, in 2011.

Dr. Rahul N. Gajbhiye is an Assistant Professor working in the Petroleum Engineering Department with King Fahd University of Petroleum and Minerals (KFUPM), Dhahran, Saudi Arabia. His research area includes rheology and drilling hydraulics, cuttings transport, and multiphase flow in pipes, fracturing, and enhanced oil recovery.

Presently, Rahul is working on carbon dioxide foam assisted enhanced oil recovery, modeling of leak detection in subsea pipelines, and polymer foam rheology for underbalance and fracturing applications.

He is a member of the Society of Petroleum Engineers (SPE), and the American Association of Drilling Engineers (AADE). Rahul has received several awards for presentations; in 2009 at the GOM Deepwater Technical Symposium, New Orleans, LA, and in 2010, at the AADE Premier Fluid Conference, Houston, TX.

He received his B.S. degree in Petroleum Engineering from the Maharashtra Institute of Technology, Pune, India, and his Ph.D. degree in Petroleum Engineering from Louisiana State University, Baton Rouge, LA.

Introduction of Real-Time Flow Measurements Opens New Paths to Overcome Challenges Encountered during the Acid Stimulation of Extended Reach Wells

Laurie S. Duthie, Hussain A. Al-Saiood, Hamad M. Almarri, and Danish Ahmed

ABSTRACT

Challenges related to matrix acid stimulation and fluid placement in extended reach horizontal wells are usually exaggerated, and demand a constant flow of innovation. The optimization of real-time fluid placement, increasing the reservoir contact and establishing uniform fluid distribution for better production/injection across the open hole interval, is one area that can benefit from these new innovations.

Coiled tubing (CT) equipped with a tractor and new real-time downhole flow measurement capabilities was selected as the solution. While a CT tractor facilitates the reach, flow measurements provide a clearer understanding of downhole injectivity patterns. Real-time fluid direction and velocity are acquired and used to identify high/low intake zones. The data is subsequently applied to adjust the stimulation diversion schedule accordingly. In a water injection well, baseline data was acquired before commencing a matrix stimulation treatment. The treatment was squeezed through the CT at the depths highlighted as low intake during the initial profiling.

The CT real-time flow tool was deployed during the matrix stimulation treatment of the extended reach water injection well with a downhole tractor. The flow tool measured the baseline injection profile, which was then correlated with the mobility data. Results from the pre-stimulation profile showed that 70% of the injection fluid was entering in a 3,000 ft section near the toe (24,500 ft), whereas 30% of the injection fluid was spread across the remainder of the open hole interval. The acquired flow data was able to identify sections of the wellbore featuring low mobility and viscous fluids, which in turn provided additional information for the adjustment of the subsequent stimulation pumping sequence. The real-time optimization of stimulation treatment helped to increase the post-stimulation injection rate by over four times the pre-stimulation rate.

The combination of the CT tractor with a real-time flow measurement tool provides an efficient means to stimulate extended reach water injector wells. The basic technology behind the real-time flow tool is a synchronized system with a series of heating elements and temperature sensors along the tool to determine the direction and mean velocity of the fluid. This ultimately allows for a more accurate placement of the

stimulation treatment to the targeted zones. The technology can also be applied for extended reach oil producers, however, for optimum tool performance, the well should first be displaced with an inert fluid.

BACKGROUND

The challenges associated with matrix acid stimulations in extended reach horizontal wells are formidable and extensive, and of those challenges, reaching total depth (TD) and the accurate placement of the stimulation fluids are two of the major ones. To overcome these challenges, a downhole coil tubing (CT) tractor is run in combination with a real-time flow tool. CT under its own "steam" can only go so far along a long horizontal wellbore before it eventually locks up under the effects of weight stacking, frictional forces, and helical buckling[1]. At that point, the CT tractor is activated to pull the coil to TD.

The 4.7" diameter CT tractor is capable of pulling up to 14,500 lb, has full flow through capability and is placed at the top of the string. The tractor is hydraulically powered from the surface by pumping a predetermined rate of fluid to activate the tractor, engaging the arms to pull the CT to the desired depth. One of the goals to simplify a complex reservoir is to obtain an evenly distributed water injection profile along the open hole section of the injector wells. The real-time flow tool solves this part of the equation, delivering accurate fluid placement to where it is most desired, and also allows for a rapid and effective evaluation of the matrix acid treatment. The real-time flow tool is connected by fiber optic cable to the surface through the CT reel, and all measurements are available via the data telemetry interfaces.

INTRODUCTION

Blikra et al. (1994)[2] defined extended reach wells on the basis of measured depth to the true vertical depth (MD:TVD) ratio, and according to the definitions, extended reach wells have a MD:TVD ratio greater than 2.0. In barefoot injectors and producer completions, even relatively shallow drilling induced near wellbore damage can substantially impede the flow or injectivity[3]. Therefore, matrix acid stimulation was required to

remove and bypass drilling induced reservoir damage from the overbalanced water-based mud, which uses calcium carbonate as a weighting material[4]. The option to bullhead the acid treatment from the surface or from a CT early lock up depth are not considered viable alternatives as this could result in a loss of control of the fluid placement.

The treatment fluids under this scenario will always find and take the path of least resistance to the highly permeable and non-damaged zones. Of course, these zones may not require treatment, and worse still, end up bypassing the zones with the greatest need of the treatment[5]. This could lead to the unfortunate outcome of the acid stimulation doing more harm than good, helping to create channels that could lead to early water breakthrough in nearby oil producer wells.

Therefore, the importance of covering the entire wellbore of the extended reach wells cannot be emphasized enough; leaving potentially large sections of the open hole in a nonproductive state will certainly lead to a poor outcome. To further stress this point; the whole reason for drilling extended reach wells — increased reservoir contact, reduced footprint, and less wells drilled — will be eliminated by a poorly executed stimulation job[6].

The open hole formation and extended reach well completions are serious impediments that must be overcome to successfully reach TD, including the effective delivery of stimulation fluids to the target zones. The intent of the authors is to demonstrate how the effective use of available technologies can be applied in these demanding environments to ensure optimized placement of needed stimulation fluids.

WELL INFORMATION

The candidate well was drilled as an extended reach power water injector, consisting of a 7,586 ft open hole toe up section. Figure 1 shows the candidate well's wellbore geometry.

The well is completed with a 7" tubing, and a 3D plot in Fig. 2 illustrates the well profile in terms of azimuth, trajectory, and inclination of the wellbore.

JOB OBJECTIVES

The main job objective was to remove formation damage and achieve full stimulation coverage of the entire open hole section. The injection rate was well below the target rate and was
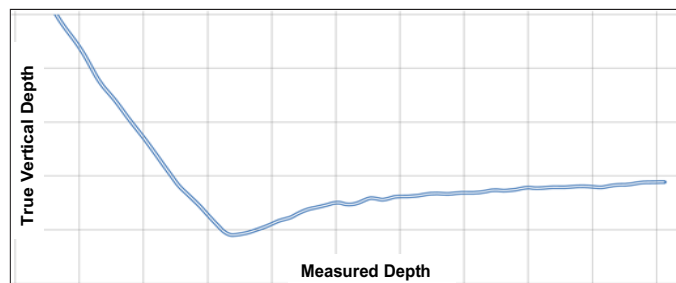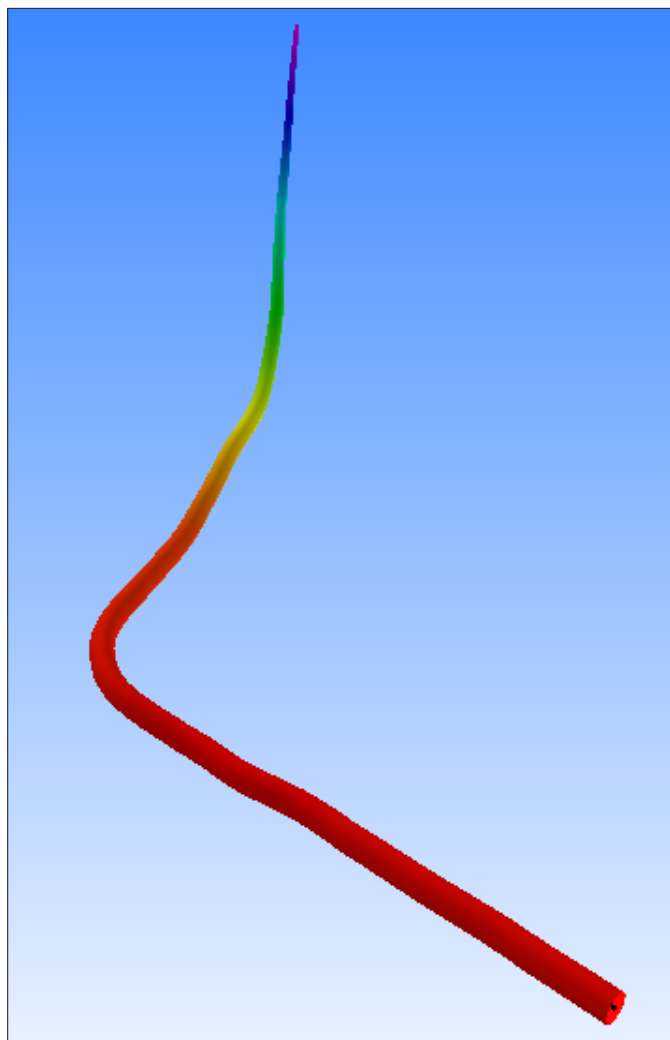

Fig. 2. A 3D well profile of the candidate well, showing the azimuth, trajectory, and inclination of the wellbore.

selected for a matrix acid stimulation to improve well injectivity. During the job's design phase, reach simulations of the CT were conducted, and it was determined that a tractor was required to ensure full coverage of the well to TD.

In addition, for an effective stimulation treatment, it is highly beneficial to obtain the pre-stimulation injection profile with identification of the tight and/or damaged, and high permeable zones.

CHALLENGES

The main challenges to reach TD were:

- A high hydrogen sulfide (H_2S) environment
- Uneven borehole
- Viscous fluids
- High load (+24,500 ft of 2" pipe)
- Open hole of +7,500 ft
- High risk of becoming stuck, due to differential pressure
- Understanding injectivity patterns

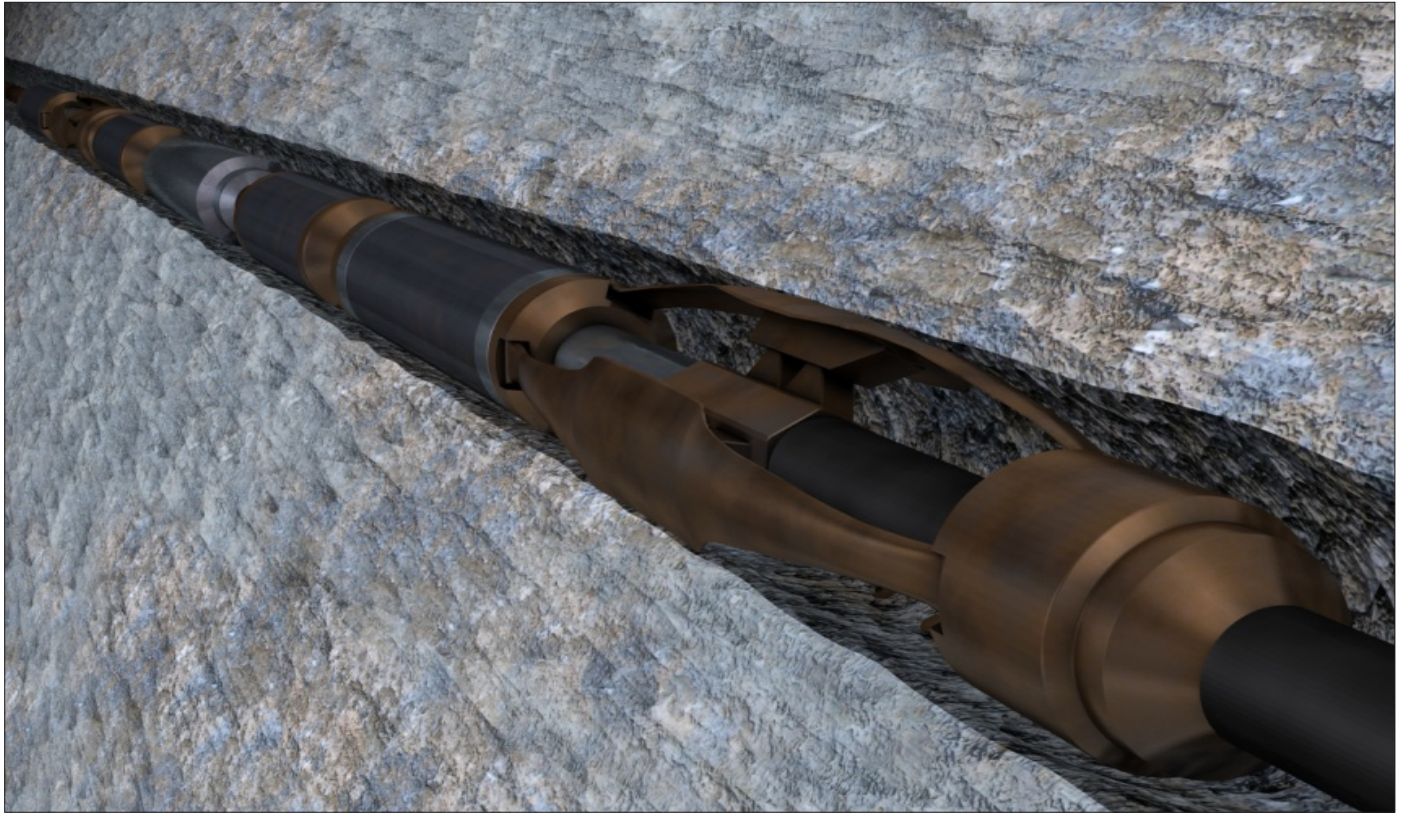Fig. 1. The wellbore geometry of the candidate well.

Fig. 3. An image of the 4.7" CT tractor.

The first five challenges can be overcome by selecting a tractor that can not only survive in this tough environment, but has been designed to deliver the high pulling force required to reach the well's TD. Another consideration and a significant risk, especially for extended reach open hole sections, was that keeping the CT stationary for lengthy periods can lead to a situation where the CT is stuck due to differential pressure.

Distributed temperature sensing (DTS) has been extensively utilized successfully for the optimization and evaluation of stimulation treatments and can provide quantitative analysis and injection profiling. An integral part of DTS operations necessitates lengthy periods of stationary CT to monitor the temperature response along the hole, and is in direct conflict with measures in place to avoid becoming stuck in the hole. DTS dependency to determine injection profiling is based on the technique of cooler fluid injection and formation warmback. This poses a challenge if there is cross flow during DTS warmback, as the DTS data cannot be utilized for interpretation. With these DTS limitations, the CT real-time flow tool was better suited to deliver the real-time flow data to better understand the injectivity patterns.

CT 4.7" TRACTOR DESCRIPTION

As shown in Fig. 3, the 4.7" CT tractor is the largest downhole CT tractor available, and is considered to be the pulling powerhouse of CT tractors. The 4.7" CT tractor can deliver up to 14,500 lb of pulling capacity and is the preferred choice for extended reach well water injectors.

CT 4.7" TRACTOR DESIGN FEATURES

Several key design features are incorporated in the 4.7" CT tractor:

- The tractor has full flow through capability, and the ability to connect tools below the surface via an electric line or fiber optic connection; the tractor can be isolated if required by dropping a ball down the CT.

- The tractor is controlled and driven 100% by hydraulic fluids, making it an ideal tool for CT operations in lengthy duration jobs.

- The arms, or "grippers," exert a positive force on the cased or open hole wellbore with constant traction and can work in a hole size in the range from 5.2" to 8½".

- This allows traversing along an uneven borehole, through viscous fluids with extremely high loads.

- The components are extremely tough, resistant to acids, H$_2$S, and are designed to cope with the harshest of downhole conditions.

Tractor Operation:

- The tractor consists of two gripper assemblies, with one assembly at either end of the tool, Fig. 4. The control unit
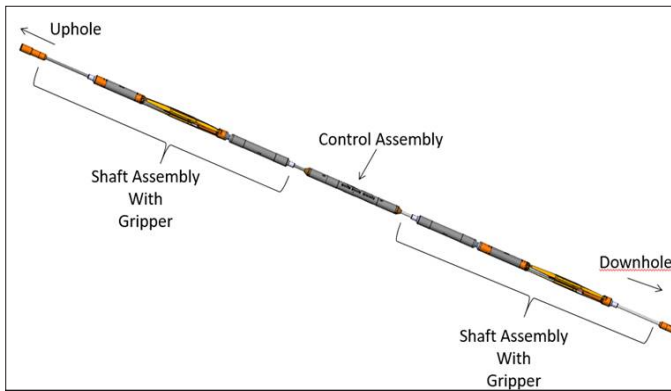
Fig. 4. CT tractor components.

diverts pumped fluids from the surface in a synchronized movement. The tractor can be started by increasing the pump rate until it exceeds the pre-set pressure.

- The fluid is diverted to the front gripping assembly, which expands and engages with the formation wall, where once engaged, a piston is activated to drive the tractor forward and pull the CT behind it.

- This is then repeated with the rear gripping assembly engaging, and then the front gripping assembly is released and pushes the tractor forward again.

- This repeated motion is similar to how an inchworm moves, Fig. 5. The tractor speed is regulated by the available differential pressure across the tool and the rate of the CT being fed through the injector head. A speed of around 15 ft/min across the horizontal section is typical.

- Once the desired depth has been reached, the tractor can

Fig. 5. Illustration of an inchworm's movement.

be stopped by simply reducing the pump rate to below the activation threshold.

- Fluid treatment can then be pumped into the formation while pulling out of the hole.

- To restart the tractor, the pump rate needs to be increased to above the predetermined set point.

CT REAL-TIME FLOW TOOL DESCRIPTION

The CT real-time flow tool, Fig. 6, provides CT measurements of downhole flow velocity and fluid direction during the matrix
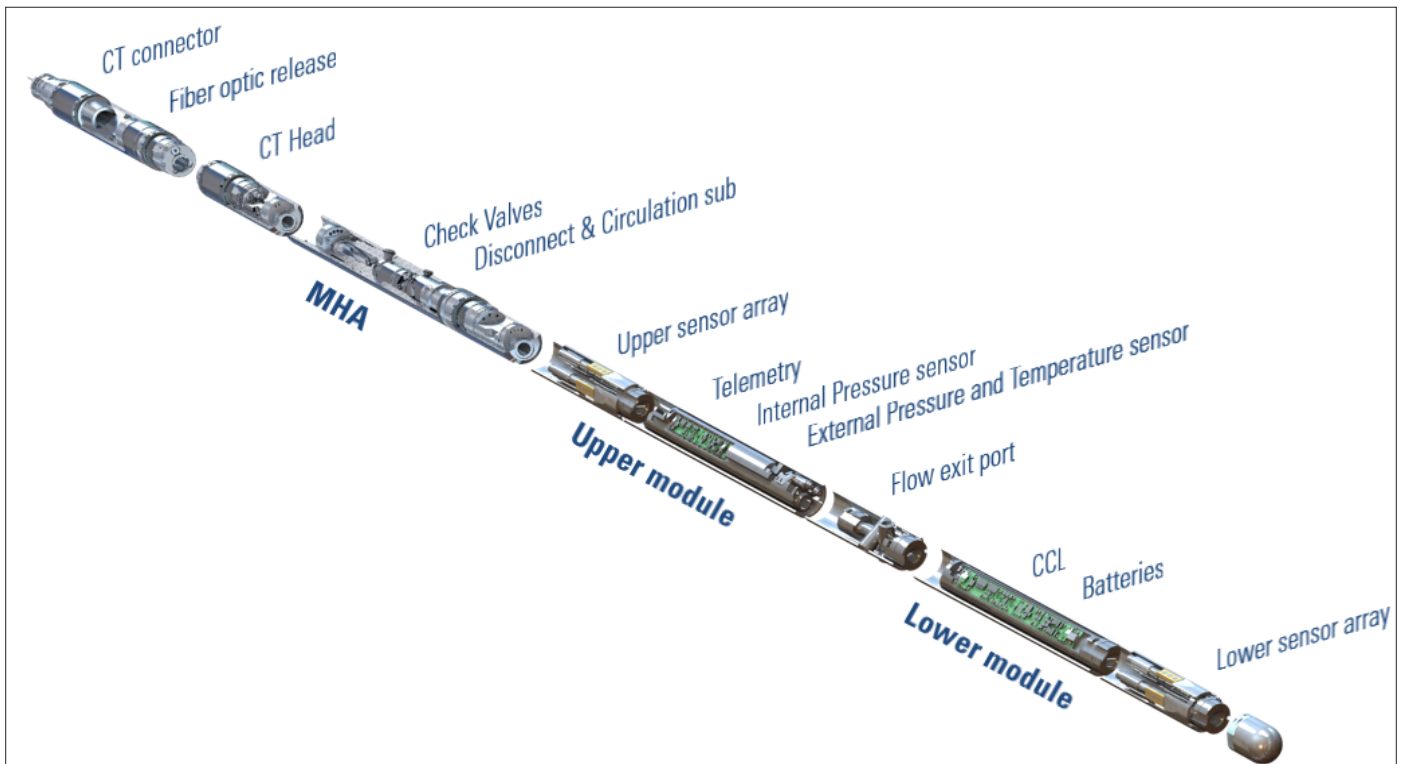
Fig. 6. The CT real-time flow tool.
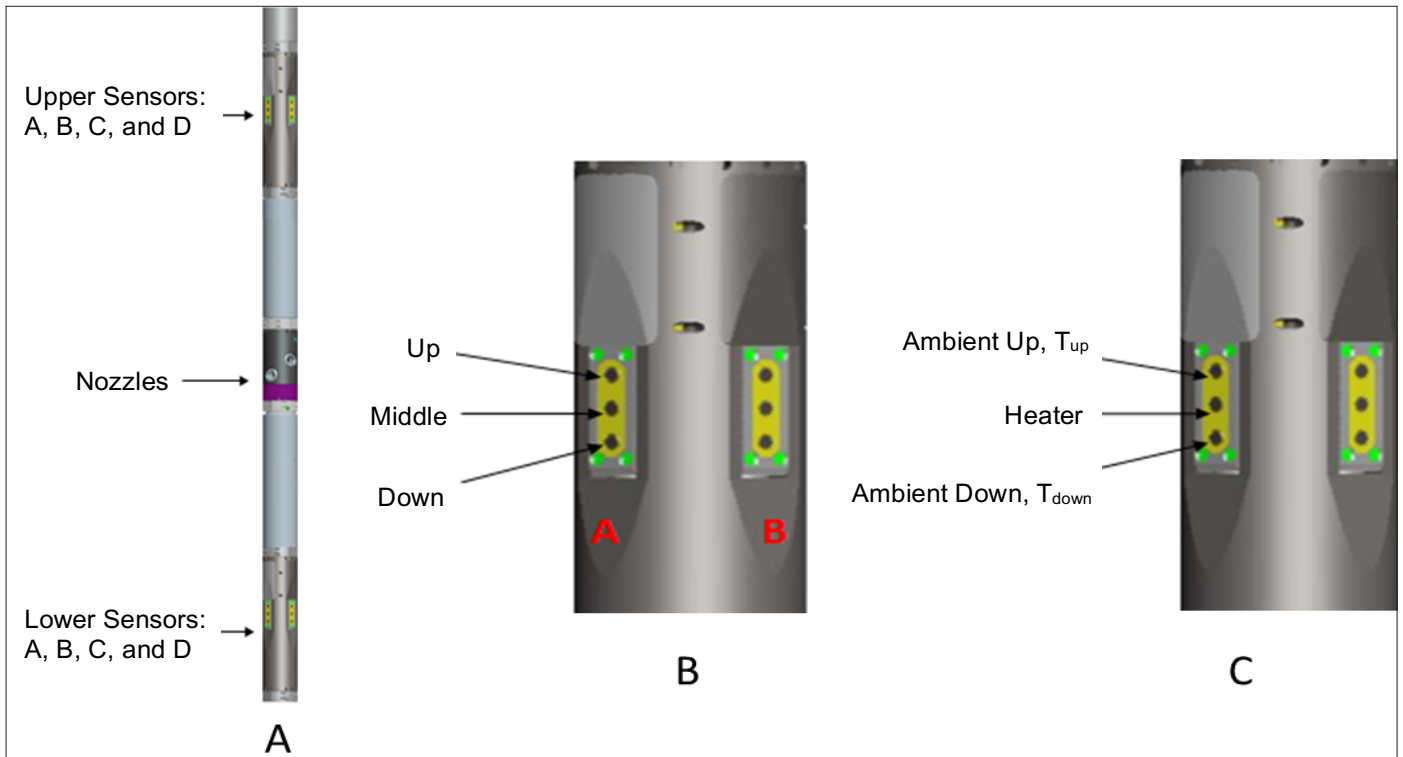
Fig. 7. The CT real-time flow tool nozzle and sensor locations.

acidizing operation along with pressure, inside the coil and outside, i.e., in the annulus, temperature, T, casing collar locator (CCL), and gamma ray. Data is transmitted to the surface via a continuous fiber optic cable placed inside the CT reel. The tool sensors are used to calculate the mean fluid velocity in the annulus between the CT reel and the wellbore, providing real-time data of the fluid distribution and direction of flow.

The fluid pumped from the surface down the CT exits via the CT real-time flow tool through nozzles situated between the upper and the lower parts, Fig. 7a. The upper and lower sections are made up of four sets of sensors: A, B, C, and D. Each set of sensors have three temperature probes, and all of the sensors are located far enough away to avoid the effects of fluid jetting. The sensor sections, Fig. 7b, have an up, middle, and down temperature probe, and all of these temperature probes have dual modes, which can act as either a heater or temperature sensor. As depicted in Fig. 7c, a typical configuration has the middle probe in heater mode at a constant temperature, and the up and down probes as temperature sensors measuring the ambient temperature. This type of configuration allows the direction of the flow to be detected[7].

In the case of upward flow being detected, Fig. 8a, the middle probe is heated, creating a thin layer of warmer fluid close to the tool, and the warmer fluid disperses in the direction of the

flow. The upper temperature probe now measures this warmer fluid, whereas the lower temperature probe continues to measure the ambient fluid temperature, therefore, the direction of flow is easily detected. To confirm the fluid direction, the temperature difference between the ambient probes T_{up} - T_{dwn} will result in a positive number, while a negative number will indicate the direction of flow as down, Fig. 8b[7].

FLUID VELOCITY CALCULATION

Fluid velocity is calculated based on the fluid thermodynamic properties using the relationship between the amounts of power dissipated to give a unit of temperature difference. The power, P, is used to heat the middle probe and is dissipated in the fluid, whereas the fluid velocity, v, is a function of the dissipated power: $v = f\,(P/DT)$. Where, the amount of the dissipated power per 1° of the temperature excursion in the fluid, P/DT, depends on the fluid velocity. To calculate the fluid
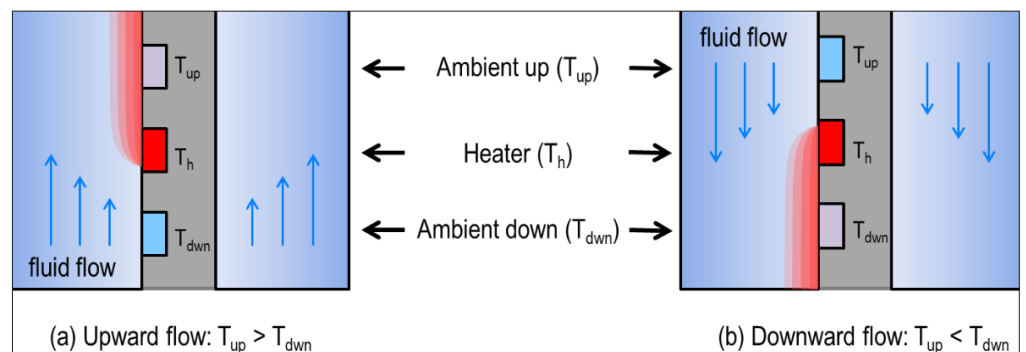

Fig. 8. The upward flow sensor (a), and the downward flow sensor (b).

velocity, a calibration of the tool is necessary to refine the relationship to actual conditions.

Although a lab-based empirical calibration for the downhole tool is possible, a more accurate calibration is obtained in situ under actual fluid and well conditions. To conduct the calibration under live conditions, the tool is normally stationed in a non-flow zone such as the casing so that 100% of the pumped fluids will go in one direction. The fluid is pumped at different pre-selected rates and the power dissipation is recorded as a function of the fluid velocity in the CT/casing annulus[7].

INTERVENTION WORKFLOW

An intervention workflow combining the CT real-time flow tool measurement and tractor was defined as outlined here:

Step 1. Performing a pre-job injectivity test:

- Perform an injectivity test before the CT is run in hole (RIH).

Step 2. CT real-time bottom-hole flow parameters tool calibration (Run-1):

- With the well in shut-in condition, RIH with CT without pumping fluid through the CT.
- Calibrate the CT real-time flow tool by RIH and pulling out of hole (POOH) at different CT speeds within the 7" liner.
- Calibrate the CT real-time flow tool by pumping water through the annulus of the CT and completion. Keep the CT stationary, but increase the pumping rates.
- Conduct the depth correlation utilizing CCL measurements.

Step 3. Pre-stimulation CT real-time flow tool injection profile (Run-1):

- RIH the CT to TD, and start the seawater injection down the CT's annulus.
- While bullheading water from the annulus of the CT, and the completion at 4.0 bbl/min, POOH to the liner shoe of the CT while recording the CT real-time flow tool.
- Perform CT real-time flow measurement tool stationary measurements (while bullheading water from the annulus of the CT and completion), stop for logging stations while recording with the CT real-time flow tool.

Step 4. Stimulation treatment (Run-2):

- Pump stimulation as per interpretation of the CT real-time flow tool.

Step 5. Post-stimulation evaluation (Run-3):

- Perform CT RIH for post-stimulation injection profiling with the CT real-time flow measurement tool.
- Perform the CT real-time flow measurement tool calibration as necessary.

Step 6. Performing post-job injectivity test:

- Perform an injectivity test after the stimulation treatment.

EXECUTION

Step 1. Performing pre-job injectivity test:

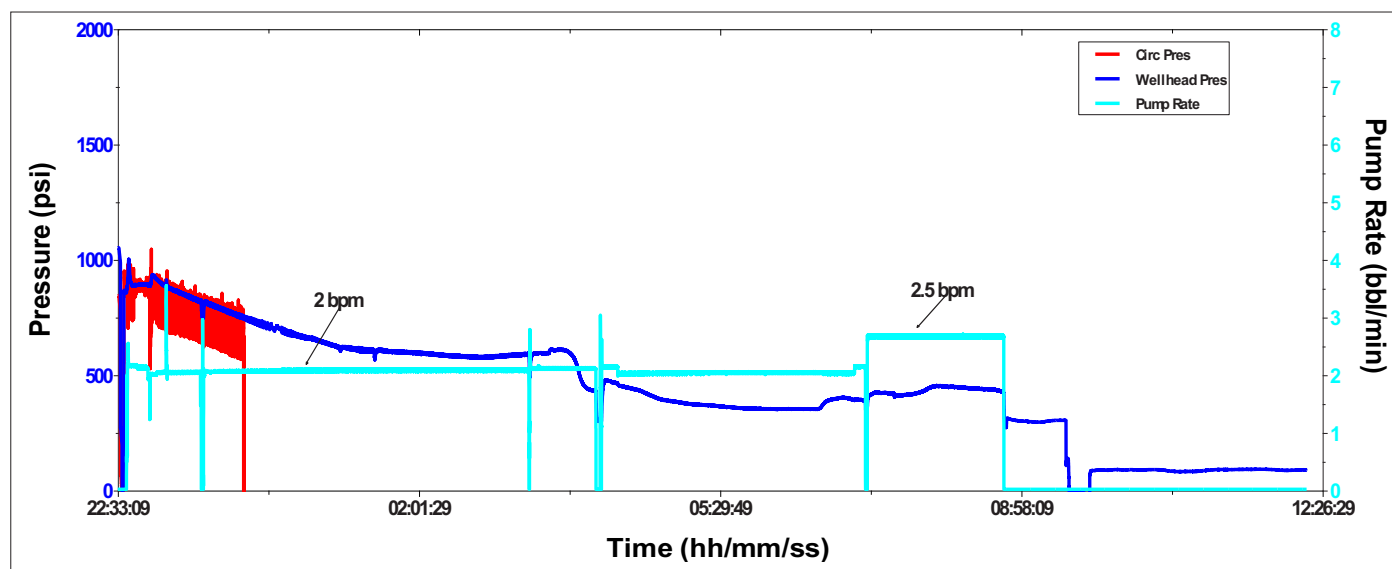Before the first CT is RIH, 30 bbl of organic solvent was

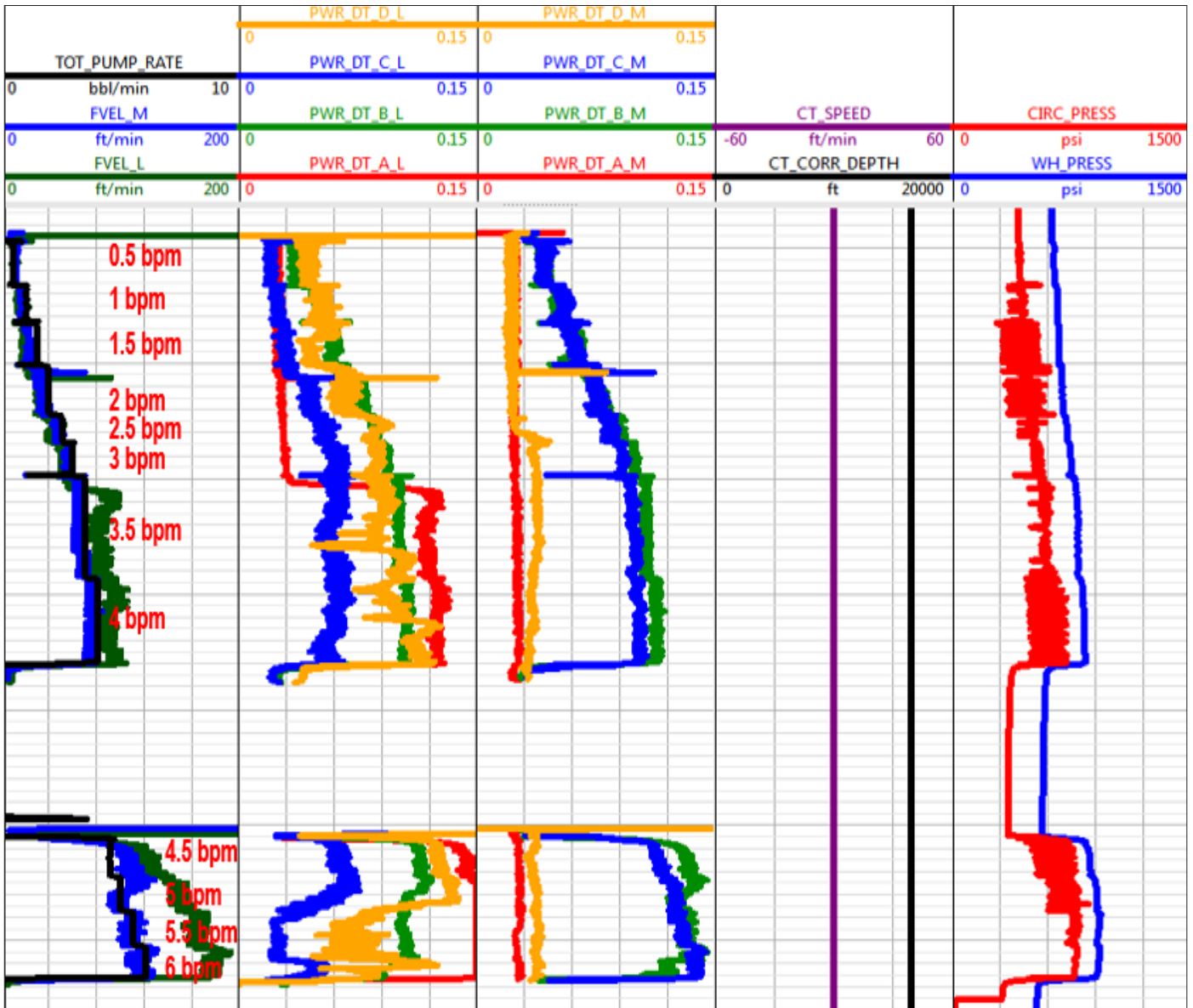Fig. 9. Results of a pre-job injectivity test with water.

Fig. 10. Results of a CT real-time flow tool calibration at depth while pumping from the annulus of the CT at different rates.
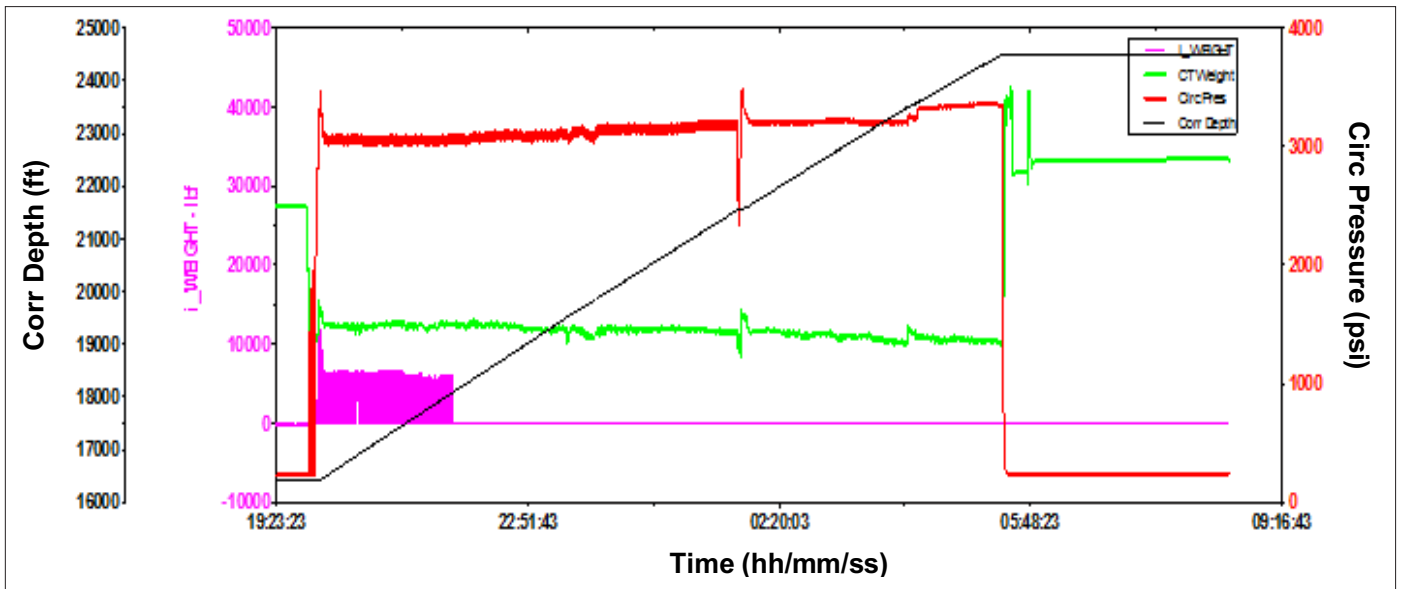

Fig. 11. The CT parameters during tractoring, Run-1.

bullheaded, followed by the pumping of 180 bbl of freshwater mixed with 20 bbl of a mutual solvent. After the complete wellbore displacement, an injectivity test with water was performed, where a total of 1,345 bbl of water was injected, Fig. 9.

Step 2. CT real-time bottom-hole flow parameters tool calibration (Run-1):

The CT was RIH with the CT real-time flow tool and tractor and consisted of the following steps:

• The CT was RIH and stopped 500 ft above the casing shoe.

• Performed a CT real-time flow tool calibration at depth by pumping through the annulus of the CT and completion at different rates, Fig. 10.

• After performing the calibration, continue to RIH and perform depth correlation at the casing shoe, before entering the open hole.

Figure 10 shows the CT real-time flow tool velocity measurement during the calibration process. The tool was stationed inside the 7" liner during calibration. The black curve in the first track represents the surface injection rate and the blue and green curves represent the downhole fluid velocity measurements from the upper and lower CT real-time flow tool, respectively. A step increase in the downhole velocity perfectly coincides with the change in surface injection rate, validating the tool's measurement.

Step 3. Pre-stimulation CT real-time flow tool injection profile (Run-1):

After correlation, the CT was RIH until it reached its maximum depth where it locked up very suddenly — weight reduction. At this point, the tractor was activated and started to RIH to the target depth. The CT reached to 24,500 ft (100 ft before TD), Fig. 11.

With the CT at 24,500 ft, a pull test was conducted to confirm the pipe was free and could maintain a stable POOH weight. Annulus injection profiling took place at 4 barrels per minute (bpm). The CT real-time flow tool injection profiling was recorded at 200 ft intervals from 24,382 ft to 20,382 ft. After this, the CT flow measurement tool sensors were

showing unclear readings, likely due to organic deposits covering the sensors. To clear the sensors, 20 bbl of water was pumped through the CT. Afterwards, the CT flow measurement tool sensors then began to show positive readings.

Injection profiling continued from 20,382 ft to 19,160 ft, and again the CT flow measurement tool sensors started to show unclear readings. An attempt to clean sensors by pumping 100 bbl of water through the CT was not effective. The next step was to mix and spot 50 bbl of organic solvent around the end of the CT to clean up the sensors. After organic solvent came out from the nozzle, the CT flow measurement tool sensors again began to show positive readings. Annulus injection profiling continued from 18,280 ft to 17,008 ft to complete the open hole profile.

Figure 12 shows the CT real-time flow tool injection profile; the injection profile (blue shaded area) is shown in the fourth track from the left. The profile is based on station
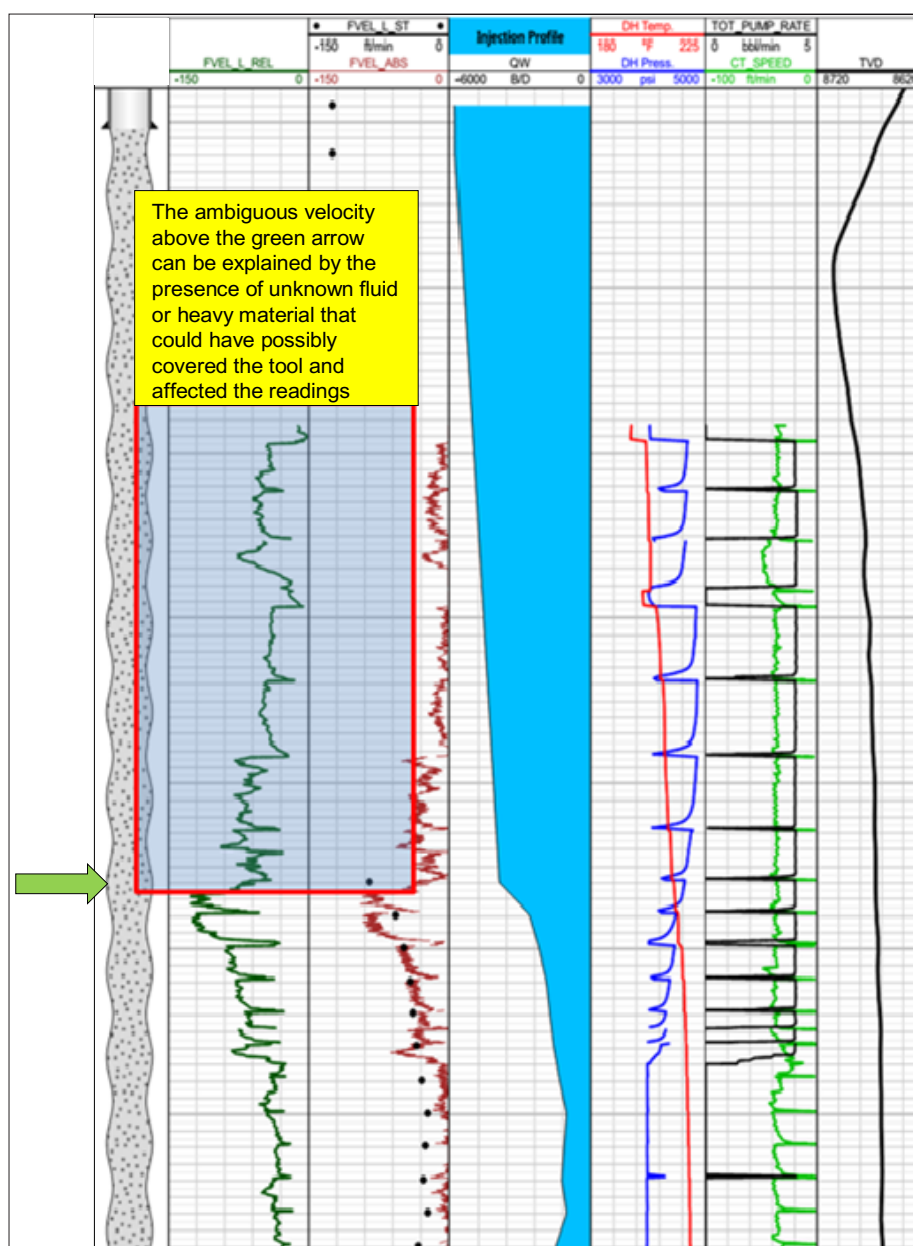

Fig. 12. The CT real-time flow tool injection profile.

measurements. The red curve in the third track from the left is the absolute downhole velocity measured by the CT real-time flow tool, while the black dots in the same track represent the velocity during stationary stops. The CT real-time flow tool velocity profile is obvious from the toe and shows a clear increasing trend. Subsequently, velocity measurements above the green arrow are affected by downhole conditions; i.e., the presence of an unknown fluid or heavy material, like tar. Therefore, the injection profile above the green arrow is a linear interpolation between the velocity measured at the green arrow, and the velocity inside the 7" liner. Based on the calculation, the open hole interval above the green arrow is taking about 32% of the total injection.

Step 4. Stimulation treatment (Run-2):

The CT was POOH to the surface after the completion of injection profiling through the CT real-time flow tool. The stimulation treatment was optimized based on the CT real-time flow tool injection profiling results, and was pumped during the CT's Run-2, Fig. 13.

- RIH to casing shoes at 17,038 ft.
- Start tractoring from the case hole to open hole and stop at 24,500 ft.
- Start mixing fluid as per the program.
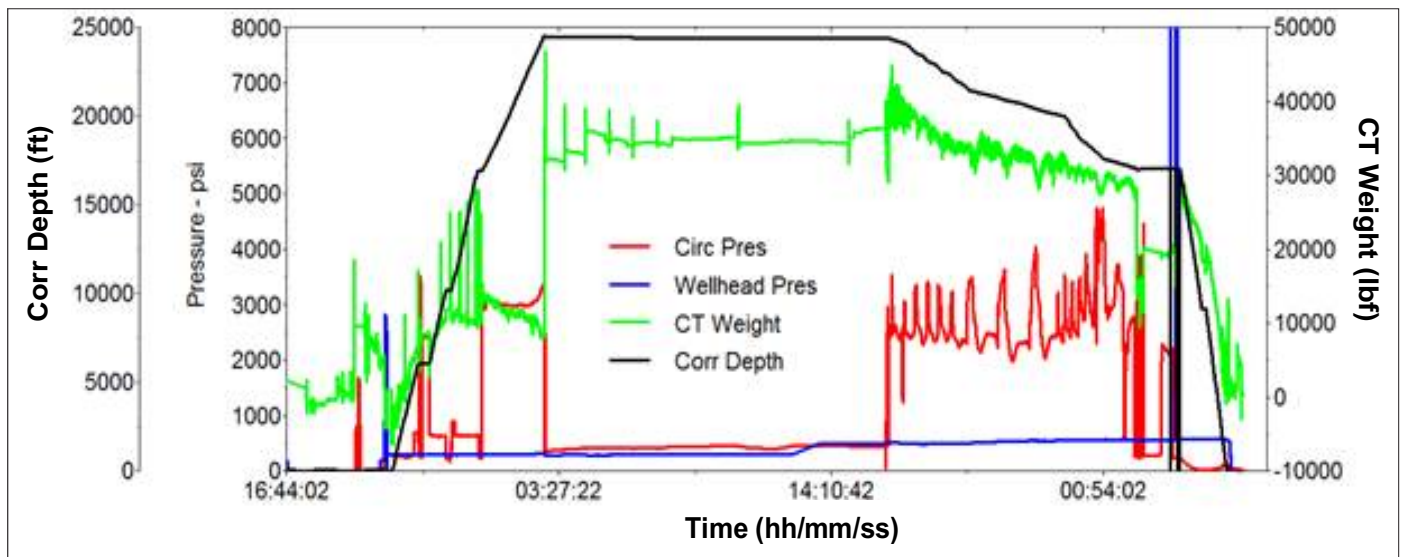- Pump the treatment as per the optimized schedule.
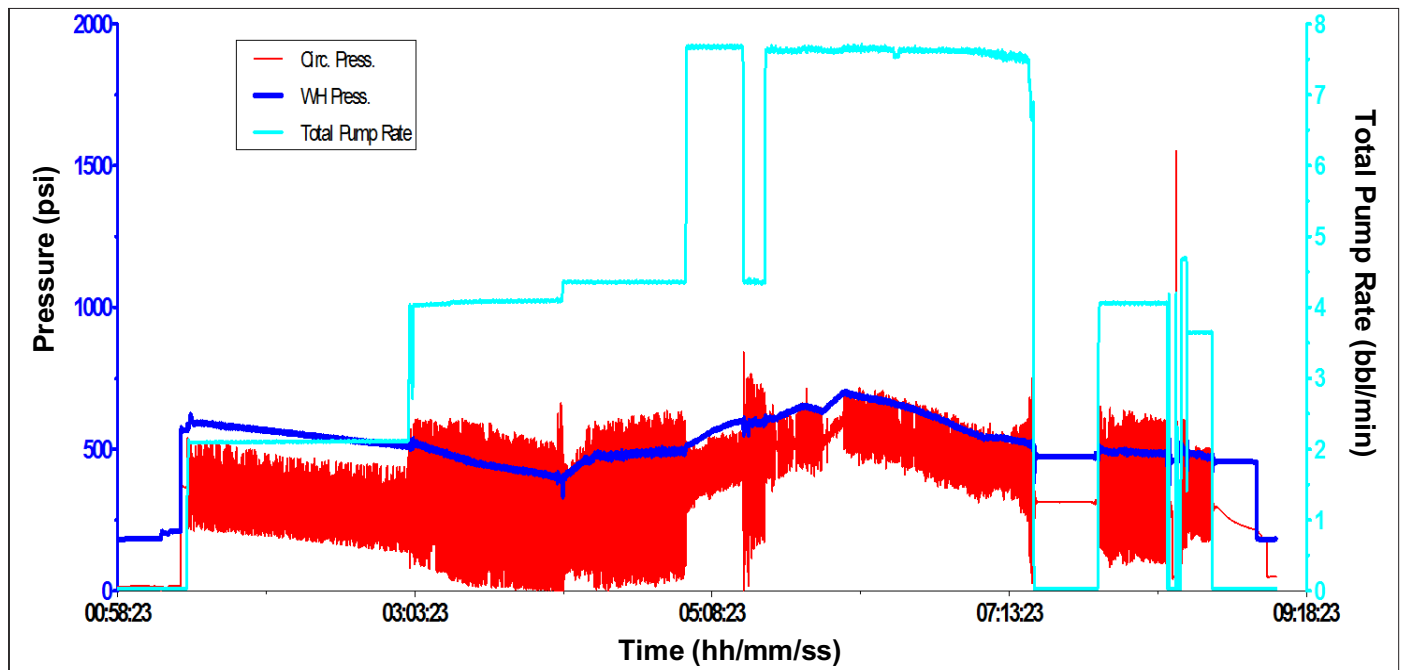

Fig. 13. The CT parameters during Run-2.

Fig. 14. Injection test after stimulation.

Step 5. Post-stimulation evaluation (Run-3) and Step 6: Performing post-job injectivity test:

Following the second CT run, the CT was POOH to the surface for Run-3 to achieve the post-stimulation injection profiling through the CT real-time flow tool. After multiple trials, the CT was only able to reach 19,650 ft; however, an injectivity test was conducted after the stimulation treatment to evaluate the effectiveness, where the injection rate was increased to 7.50 bpm, and the maximum wellhead pressure reached only 650 psi, Fig. 14. Compared to the pre-stimulation, the injection rate was four times higher — 8.0 bpm compared to 2.0 bpm — with a similar wellhead pressure ~500 psi.

SUMMARY

1. The CT real-time flow tool data displayed a good correlation with downhole data showing the presence of heavy fluids, therefore proving the CT real-time flow tool measurements are reliable and can be used in cases where no other data is available.

2. The CT real-time flow tool calibration in the cased hole section, pumping from the annulus and conducting CT real-time flow tool pre-stimulation profiling while the CT is POOH, and the CT stations in the open hole section were completed successfully.

3. The CT real-time flow tool profiling results showed that most of the injection, i.e., approximately 68% of the injection is entering from 21,600 ft to TD. The remaining injection (32%) is spread from the heel section to 21,600 ft.

4. During the CT real-time flow tool profiling and the CT real-time flow tool stationary measurements from the heel to 21,000 ft, it was observed that the CT real-time flow tool sensors were contaminated by unknown fluids in the deepest section of the wellbore. Subsequently, more stationary measurements helped in acquiring a complete injection profile, therefore, the injection profile above 21,600 ft is a linear interpolation between the measured CT real-time flow tool velocity at 21,600 ft and the total velocity inside the 7" casing.

5. The CT real-time flow tool pre-stimulation profiling results were applied to optimize the pumping schedule.

6. During the third CT real-time flow tool run for post-stimulation profiling, CT lockup occurred at 19,600 ft during RIH; several attempts to free the CT were conducted without success. Therefore, CT real-time flow tool data for post-stimulation profiling could not be recorded, as an adequate amount of open hole was not able to be reached.

CONCLUSIONS

The combination of state-of-the-art integrated technologies to access the entire length of the 24,500 ft wellbore and achieve accurate and optimized fluid placement are critically important factors in delivering a well-managed reservoir. The robust design of the tools is also a key factor in the successful deployment. The tools are manufactured to withstand large compressive and tensile loads, high resistance to H_2S, and corrosive fluids such as acid.

The world's first intervention of this type, running the CT real-time flow tool together with a CT tractor, has shown promising results. This allowed for an accurate and efficient fluid treatment placement with downhole flow monitoring data in real-time to quickly evaluate the treatment effectiveness. This, in turn, led to the main job objectives being met with a 400% improvement in well injectivity achieved.

ACKNOWLEDGMENTS

REFERENCES

1. Beheiri, F.I., Al-Mubairik, A.J., Al-Mulhim, A.K., Al-Meshal, F.M., et al.: "Optimization of Coiled Tubing Interventions on Extended Reach Open Hole Completion in a Field in Saudi Arabia," SPE paper 116845, presented at the SPE Russia Oil and Gas Technical Conference and Exhibition, Moscow, Russia, October 28-30, 2008.

2. Blikra, H., Drevdal, K.E. and Aarrestad, T.V.: "Extended Reach, Horizontal, and Complex Design Wells: Challenges, Achievements and Cost Benefits," SPE paper 28005, presented at the 14th World Petroleum Congress, Stavanger, Norway, May 29-June 1, 1994.

3. Bennion, D.B., Thomas, F.B. and Bietz, R.F.: "Formation Damage and Horizontal Wells — A Productivity Killer?" SPE paper 37138, presented at the International Conference on Horizontal Well Technology, Calgary, Alberta, Canada, November 18-20, 1996.

4. Arukhe, J., Duthie, L.S., Al-Ghamdi, S., Hanbzazah, S., et al.: "World's First Tandem 2.125" Coiled Tubing Tractor for ESP Open Hole Completions," SPE paper 17386, presented at the International Petroleum Technology Conference, Doha, Qatar, January 20-22, 2014.

5. Al-Najim, A., Zahedi, A., Al-Khonaini, T., Al-Sharqawi, A., et al.: "A New Methodology for Stimulation of a High Water Cut Horizontal Oil Well through the Combination

of a Smart Chemical System with Real-Time Temperature Sensing: A Case Study of South Umm Gudair Field, PZ Kuwait," SPE paper 154387, presented at the SPE/ICoTA Coiled Tubing and Well Intervention Conference and Exhibition, The Woodlands, Texas, March 27-28, 2012.

6. Duthie, L.S., Saeed, A., Shaheen, S., Saiood, H., et al.: "Design Transformation of Hydraulically Powered Coiled Tubing Tractors for Matrix Acidizing Stimulations in Extended Reach Carbonate Reservoirs," SPE paper 188927, presented at the Abu Dhabi International Petroleum Exhibition and Conference, Abu Dhabi, UAE, November 13-16, 2017.

7. Buhassan, S., Halder, S., Tammar, H., Beheiri, F., et al.: "Case History: New Horizons for Downhole Flow Measurements via Coiled Tubing Equipped with Real-Time Downhole Sensors at South Ghawar Field, Saudi Arabia," SPE paper 172570, presented at the SPE Middle East Oil and Gas Show and Conference, Manama, Kingdom of Bahrain, March 8-11, 2015.

BIOGRAPHIES

Laurie S. Duthie is a Production Engineer with Saudi Aramco and part of a team focused on the development of the Manifa field increment. He has more than 27 years of experience in oil and gas exploration and production operations, management, and petroleum engineering consulting. Laurie started his career in 1986 on offshore installations in the U.K. North Sea as a Field Engineer in well testing and wireline operations. He gained extensive operational experience in diverse remote locations — onshore and offshore — across Africa, Central Asia, the former Soviet Union and the Asia Pacific, with the last few years in the Middle East region.

Laurie received his M.S. degree in Petroleum Engineering in 2005 from the University of New South Wales, Sydney, Australia.

Hussain A. Al-Saiood is a Production Engineer working in the Manifa Production Engineering Division of Saudi Aramco's Northern Area Production Engineering and Well Services Department. Joining Saudi Aramco as a Petroleum Engineer, he has also held several drilling and reservoir engineering positions, covering several onshore and offshore fields. Hussain's areas of interest include rigless intervention with coiled tubing (CT), wireline, and hydraulic workover operations.

Throughout his career, he has worked in multiple projects, including the change out of electric submersible pumps utilizing the hydraulic workover unit, and developing downhole equipment to enhance the CT reach, i.e., CT tractors and pulsation tools, in extended reach wells for stimulation and logging applications.

Hussain received his B.S. degree in Petroleum Engineering from the University of Oklahoma, Norman, OK.

Hamad M. Almarri is a Production Engineer in the Manifa Production Engineering Unit under the Northern Area Production Engineering and Well Services Department. From 2009 to 2013, Hamad spent one year with the Safaniyah Production Engineering Unit, one year with the Manifa Reservoir Management Unit and almost two years with the Manifa Production Engineering Unit.

In 2009, he received his B.S. degree in Petroleum Engineering from the University of Louisiana at Lafayette, LA, and began working with the Safaniyah Production Engineering Unit as a Production Engineer.

In 2015, Hamad received his M.S. degree in Energy and Mineral Engineering from Pennsylvania State University, State College, PA.

Danish Ahmed has been working at Saudi Arabia Schlumberger since 2007. He is the technical expert currently working with Schlumberger Well Services – Coiled Tubing Services. Danish's experience involves working as a Field Engineer with Well Production Services (Fracturing and Pumping Services) based in 'Udhailiyah, where he designed, executed and evaluated the proppant/acid fracturing and matrix acidizing jobs. Danish also worked as a Production Technologist with Petro-Technical Services (formerly called Data and Consulting Services) in Dhahran, Saudi Arabia.

In 2007, he received his M.S. degree in Petroleum Engineering from the Heriot-Watt Institute of Petroleum Engineering, Edinburgh, Scotland, U.K.

Transport Properties of Heterogeneous Carbonate and Sandstone Samples from Digital Rock Physics and Laboratory Measurements

Abrar A. Alabbad and Dr. Jack Dvorkin

ABSTRACT

Coarse resolution digital images do not reveal the pore-scale features of rock. Instead, they offer a large field of view (FOV), enabling a better representation of the textural heterogeneity of rock at the plug scale. Here we present a digital rock physics (DRP) workflow to estimate the porosity, permeability, and electrical resistivity from such 3D images of sandstone and carbonate plugs. These samples were imaged at two energy levels providing the volumes of the bulk density, ρ_b, and photoelectric factor, P_f, respectively. The latter was converted into the mineralogy volumes that, in turn, gave us the mineral matrix (or grain) density, ρ_g, volumes. These volumes, combined with ρ_b, gave us the total porosity, ϕ, volumes from the mass-balance equation.

Next, we used the Kozeny-Carman permeability-porosity equation to arrive at the elemental absolute permeability, k, at each voxel. In the same fashion, Archie's equation was used to obtain an elemental electrical formation factor, F, distribution inside each plug. The effective k and F of the entire plug were then computed using the respective computational modules of the multiphysics package COMSOL.

These DRP results were validated by physical data. The computed effective ρ_b, ρ_g, and ϕ appeared to closely match the laboratory values, as did the formation factor. Quantifying the permeability proved to be more problematic since k not only depends on ϕ, but also on the grain size, which cannot be directly determined from the coarse resolution images. Still, by selecting a plausible grain size value, we achieved a match between the computed and measured permeability, although not as robust as for the electrical formation factor.

This workflow is an example of the dual energy X-ray computed tomography (CT) applications in estimating the basic petrophysical properties of sandstone and carbonate rocks. An extension of this methodology will be a combination of coarse resolution imaging with selected pore-scale microtomographic images used to determine the permeability-porosity and formation factor-porosity relations, which can consequently be used in each coarse element to compute the effective k and F.

INTRODUCTION

Computing Directional Effective Transport Properties

The original idea of digital rock physics (DRP) "image and compute," is to produce the pore-scale 3D images of rock fragments and then simulate a desired physical process in such a digital object: fluid flow to obtain permeability, electrical current flow to obtain resistivity, and stress field to obtain the elastic moduli[1]. To accomplish this objective, high resolution images of rocks are required to resolve the fine details of the pore structure and simulate such processes. The drawback of this approach is that the field of view (FOV) is compromised — the finer the resolution, the smaller FOV. This is a disadvantage, since often strong heterogeneity of natural rock cannot be captured within a small FOV. To overcome this challenge, we need to develop a method to estimate the physical properties of rocks on relatively large samples where the resolution is coarser than the pore scale, and therefore, the pore structure is not adequately resolved[2].

To address this challenge, we produced dual energy 3D images of inch-sized carbonate and sandstone samples. Needless to say, the pores were not resolved for this large FOV. These computed tomography (CT) scan images were transformed into 3D volumes of the bulk density, ρ_b, and photoelectric factor, P_f. The P_f volumes were used to obtain the volume fractions of the minerals in each voxel and then compute their grain density, ρ_g. Next, ρ_b and ρ_g were used to compute the total porosity, ϕ, for each voxel from the mass-balance equation[2]. The electrical conductivity, σ, and absolute permeability, k, in each voxel were assumed to be related to ϕ according to the Archie and Kozeny-Carman equations, respectively[3]. Finally, a Darcy-type solver was used to compute the effective electrical conductivity, σ_{eff}, and absolute permeability, k_{eff}, of each 3D volume. The effective electrical formation factor, F_{eff}, was obtained from σ_{eff} and the conductivity of the brine.

These computational results were compared to the laboratory measurements. The densities, ρ_b and ρ_g, and ϕ from DRP, matched the laboratory results. The F_{eff} match was also satisfactory. To match the DRP's effective k_{eff} to the laboratory data, we had to adjust the grain size used in the

Kozeny-Carman equation. A single average grain size, d_g, was used for all carbonate samples, and a different d_g was used for all sandstone samples. Except for some of the samples, the k_{eff} match between the DRP and laboratory appeared to be adequate as well. To address the uncertainty in the grain size, scanning electron microscope (SEM) images were obtained for five samples. Using these results helped us somewhat improve the DRP laboratory match. The new methodology introduced here opens a way of utilizing coarse resolution CT scan images of plugs and even cores to estimate the transport properties of large heterogeneous samples.

Electrical Conductivity and Permeability Anisotropy

To analyze the σ and k anisotropy, we assumed that the laboratory measurements of the parallel to bedding core plugs represented the simulation results in the X and/or Y directions, while the measurements of the normal to bedding core plugs corresponded to the simulation results in the Z direction. After numerically simulating the directional σ_{eff} and k in all three directions for each sample, we found that all samples were approximately isotropic. These results were confirmed by the laboratory data.

SAMPLE DESCRIPTION

There is a total of four core plug pairs — three carbonate pairs #1 to #3, and one sandstone pair #4. In addition, we used one sandstone core plug cut normal to the bedding. Its parallel-to-the-bedding pair was damaged and could not be used.

A core description, as well as a thin section description, were obtained for all carbonate and sandstone samples.

Core Description

The carbonate samples are light gray, composed of approximately 80% calcite and 20% dolomite, cryptocrystalline to fine crystalline with no visible porosity. The sandstone samples are dark brown, composed of approximately 90% quartz and 10% clay, moderately consolidated, argillaceous, non-calcareous, fine- to medium-grained with noticeable porosity.

Thin Section Description

The carbonate samples are composed of two main lithologies: dolomitized rock, and micritized lime mudstone. The dolomitized rock is cross-lined with a dark muddy matrix. It also contains micritized oolites, aggregate grains (mostly oolites) and fresh unmicritized grains, including paleopods. The micritized lime mudstone is very heterogeneous mixed with burrowed mudstone. No visible porosity is apparent in the carbonate thin sections, perhaps due to very small pore size.

The sandstone samples are composed of a heterogeneous siliciclastic unit with two main interlayered and intermixed
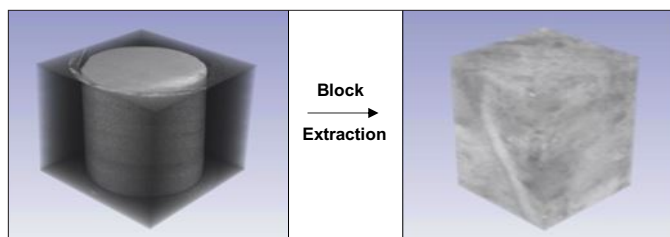

Fig. 1. On the left is a core plug image as received, and on the right is the extracted block.

lithologies: fine-grained sandstone and layers of muddy sandstone. The fine-grained sandstone is well sorted with high visible porosity. At the same time, some pores are mud clogged and appear to have patchy distributions in the samples examined. The layered muddy sandstone is composed of approximately 50% organic rich mudstone and 50% siltstone. The sandstone sample's thin sections show fairly large chunks of bitumen and charcoal — woody material.
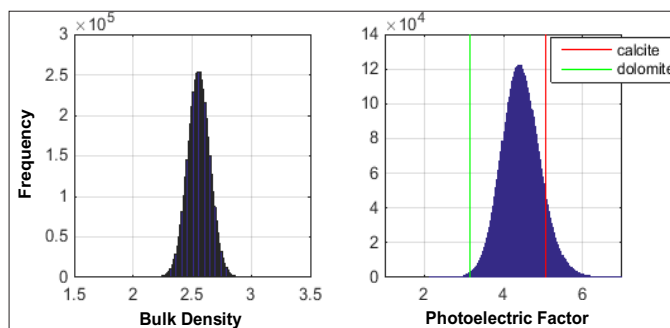

Fig. 2. The ρ_b (g/cc) and P_f (barns/electron) distributions of Pair 1 parallel to the bedding carbonate sample.
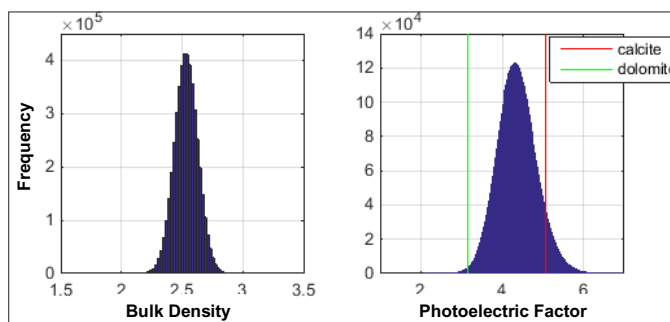

Fig. 3. The ρ_b (g/cc) and P_f (barns/electron) distributions of Pair 1 normal to the bedding carbonate sample.
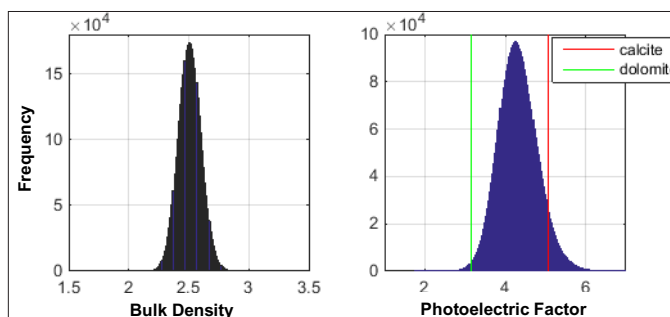

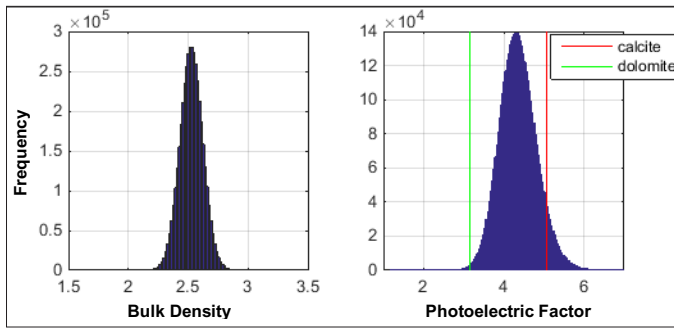Fig. 4. The ρ_b (g/cc) and P_f (barns/electron) distributions of Pair 2 parallel to the bedding carbonate sample.

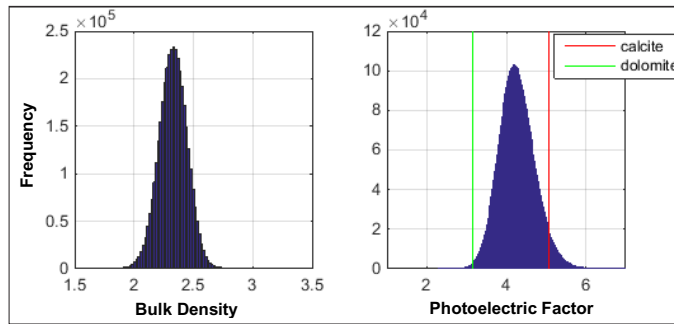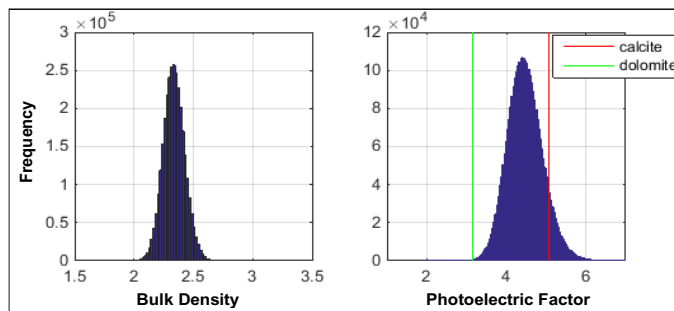Fig. 5. The ρ_b (g/cc) and P_f (barns/electron) distributions of Pair 2 normal to bedding the carbonate sample.

Fig. 6. The ρ_b (g/cc) and P_f (barns/electron) distributions of Pair 3 parallel to the bedding carbonate sample.

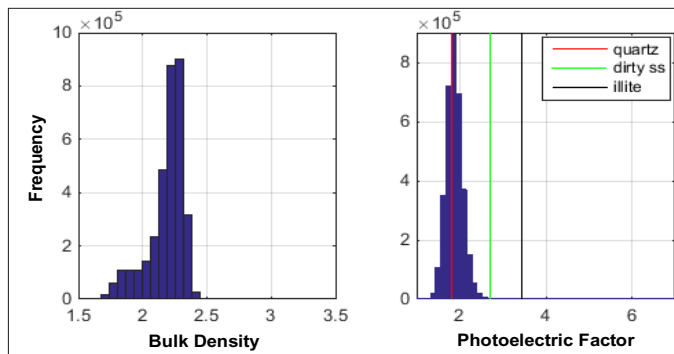Fig. 7. The ρ_b (g/cc) and P_f (barns/electron) distributions of Pair 3 normal to bedding carbonate sample.

Fig. 8. The ρ_b (g/cc) and P_f (barns/electron) distributions of Pair 4 parallel to the bedding sandstone sample.

DRP WORKFLOW

Our computational workflow includes two steps: (1) estimating rock properties, namely mineralogy, density, porosity, permeability, and electrical conductivity at each voxel, and (2) using the respective elemental volumes as input for numerical
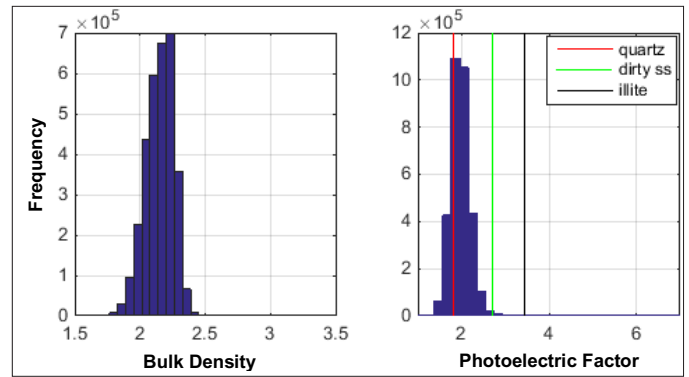

Fig. 9. The ρ_b (g/cc) and P_f (barns/electron) distributions of Pair 4 normal to the bedding sandstone sample.
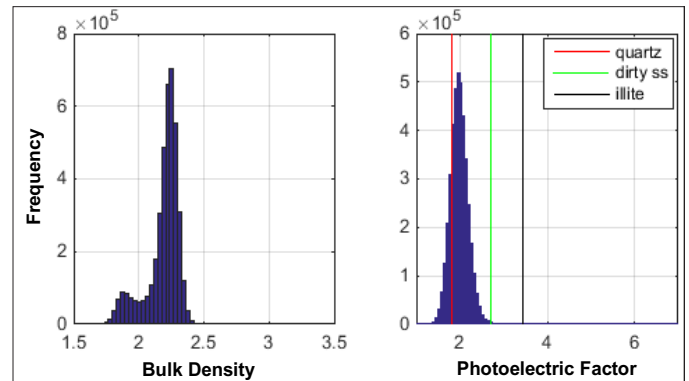

Fig. 10. The ρ_b (g/cc) and P_f (barns/electron) distributions of a normal to the bedding sandstone sample whose pair was damaged.

simulations to obtain the directional effective transport properties[2].

Computing Rock Properties at each Voxel

Dual Energy 3D ρ_b and P_f Raw Data. The raw images contain the cylindrical core plugs encased in sleeves. Our first step was to extract a rectangular block from these images, Fig. 1.

Figures 2 to 10 show the histograms of the ρ_b and the P_f for each rectangular block.

Scalar Rock Properties: Mineralogy, ρ_g, and ϕ. The P_f 3D volumes were used to determine the mineralogy of our samples, and then the ρ_g and porosity. The P_f volumes give information about mineral mass fractions at each voxel ($Mineral_m^{ijk}$); however, we need their volume fractions in the mass-balance equation ($Mineral_v^{ijk}$). In the carbonate samples, we assumed the rocks are composed of calcite and dolomite. The volume fraction of calcite was computed at each voxel using Eqns. 1 and 2, with the individual mineral P_f values listed in Table 1[4].

$$calcite_m^{ijk} = \frac{P_f^{ijk} - P_{f\,dolomite}}{P_{f\,calcite} - P_{f\,dolomite}} \tag{1}$$

$$calcite_V^{ijk} = \frac{calcite_m^{ijk}\,\rho_{dolomite}}{\left(dolomite_m^{ijk}\,\rho_{calcite}\right) + \left(calcite_m^{ijk}\,\rho_{dolomite}\right)} \tag{2}$$

Determining the mineralogy of the sandstone samples was

Mineral	ρ_b (g/cc)	P_f (barns/electron)
Calcite	2.71	5.08
Dolomite	2.87	3.14
Quartz	2.65	1.81
Dirty Sandstone	2.39	2.7
Illite	2.52	3.45

Table 1. The mineral's densities used to calculate the ρ_g and the P_f of the samples[12]

more challenging because sandstones are rarely composed of pure quartz and often found mixed with various clay minerals and shale. Therefore, to address this uncertainty in the mineralogy of sandstone and to test the flexibility of our method, we chose two scenarios: (1) to partition the composition into pure quartz and "dirty" sandstone, and (2) to partition it into pure quartz and illite. Then, similar to the carbonate samples, we computed the volume fractions for both scenarios at each voxel, using Eqns. 3 to 6 with the P_f values listed in Table 1.

$$quartz_m^{ijk} = \frac{P_f^{ijk} - P_{f\,dirty\,ss}}{P_{f\,quartz} - P_{f\,dirty\,ss}} \tag{3}$$

$$quartz_V^{ijk} = \frac{quartz_m^{ijk}\,\rho_{dirty\,ss}}{\left(dirty\,ss_m^{ijk}\,\rho_{quartz}\right) + \left(quartz_m^{ijk}\,\rho_{dirty\,ss}\right)} \tag{4}$$

$$quartz_m^{ijk} = \frac{P_f^{ijk} - P_{f\,illite}}{P_{f\,illite} - P_{f\,illite}} \tag{5}$$

$$quartz_V^{ijk} = \frac{quartz_m^{ijk}\,\rho_{illite}}{\left(illite_m^{ijk}\,\rho_{quartz}\right) + \left(quartz_m^{ijk}\,\rho_{illite}\right)} \tag{6}$$

Figure 11 shows the ρ_b vs. P_f cross-plots, indicating that some of the local P_f values fall outside the pure mineral bounds. The same is true for ρ_b, where some of the values exceeded 3 g/cc or even fell below zero. The histograms previously shown in Figs. 2 to 10 indicate that the number of such outliers is quite small and may be related to some artifacts in image acquisition. Based on these facts, our strategy of dealing with the outliers was as follows. If a local P_f value fell outside the pure mineral bounds, the value assigned to the voxel was that of the closest pure mineral P_f. For the ρ_b, any voxel with the ρ_b larger than ρ_g was assigned $\rho_b = \rho_g$. The voxels with negative ρ_b values were assumed to have zero density (100% porosity).

The ρ_g was computed next using the mineral's densities and volume fractions at each voxel via Eqns. 7 to 9 using the values listed in Table 1.
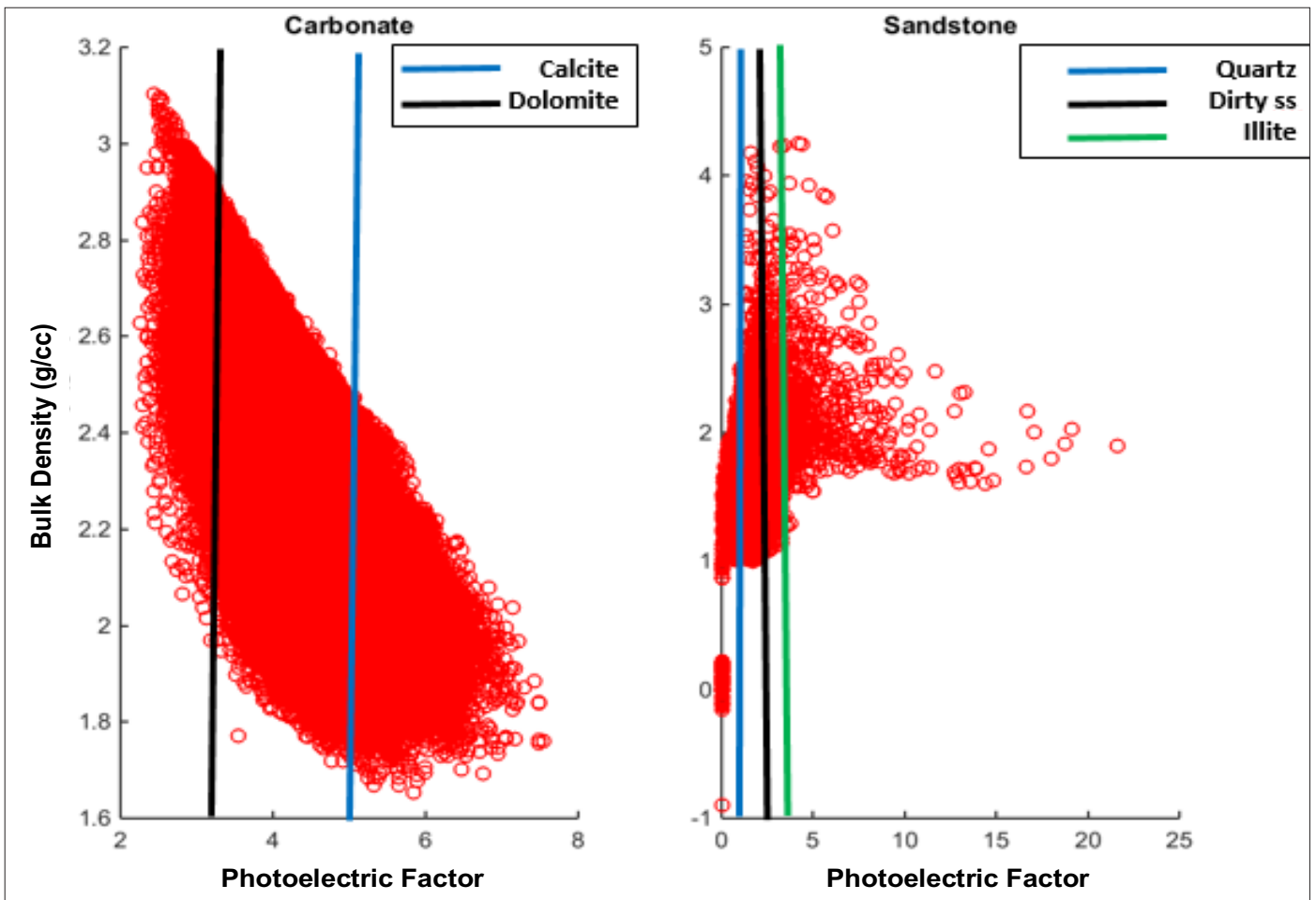

Fig. 11. The ρ_b (g/cc) vs. the P_f (barns/electron) cross-plot is shown for one sample of each lithology. The carbonate (left) and sandstone (right) samples show different patterns, which indicates differences in mineralogy and organic matter content. Data points that fall outside the mineralogy limits is assumed to be 100% composed of the mineral closest to it. The histograms in Figs. 2 to 10 show that the number of such outliers is statistically insignificant.
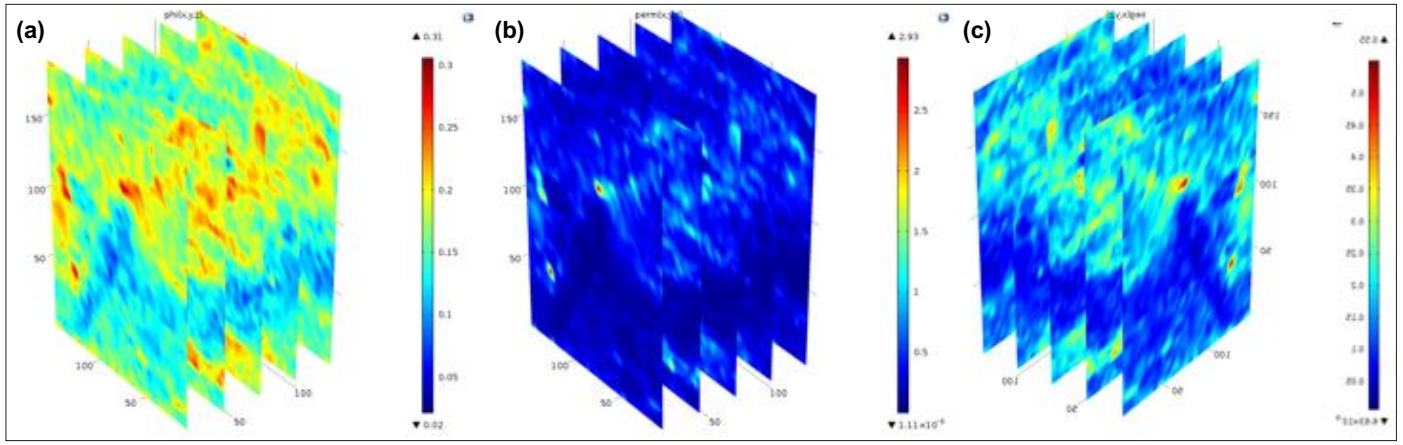
Fig. 12. Input files required for numerical simulations: (a) shows the 3D porosity profile, (b) shows the computed 3D permeability (mD), and (c) shows the 3D electrical conductivity (S/m).

$$\rho_{grain\,(carbonate)}^{ijk} = calcite^{ijk} * \rho_{calcite} + (1 - calcite^{ijk}) * \rho_{dolomite}$$
(7)

$$\rho_{grain\,(sandstone)}^{ijk} = quartz^{ijk} * \rho_{quartz} + (1 - quartz^{ijk}) * \rho_{dirty\,ss}$$
(8)

$$\rho_{grain\,(sandstone2)}^{ijk} = quartz^{ijk} * \rho_{illite} + (1 - quartz^{ijk}) * \rho_{illite}$$ (9)

The ϕ was then calculated at each voxel using the local ρ_b and the ρ_g, using Eqn. 10, which assumes that the pores are empty.

$$\Phi_t^{ijk} = 1 - \frac{\rho_{bulk}^{ijk}}{\rho_{grain}^{ijk}}$$
(10)

Transport Properties: Formation Factor and Permeability. We computed the formation factor using Archie's equation (Eqn. 11) with the same cementation exponent, m = 2, and tortuosity, a = 1, for all carbonate and sandstone samples.

$$F^{ijk} = \frac{a}{(\Phi_t^{ijk})^m}$$
(11)

Then, we related the electrical resistivity to the formation factor using Eqn. 12 with the same water resistivity as used in the laboratory measurements. Since the numerical simulation model requires 3D σ as input files, we calculated the σ as the inverse of resistivity at each voxel.

$$R^{ijk} = F^{ijk} R_w$$
(12)

The Kozeny-Carman relation (Eqn. 13) was used to determine permeability in millidarcies (mD) using tortuosity, τ = 2.5, and average grain sizes, $d_{carbonate}$ = 4.4 μm and $d_{sandstone}$ = 2.6 μm, for carbonate and sandstone, respectively.

$$k_{(mD)}^{ijk} = \frac{10^9}{72} \frac{(\Phi_t^{ijk})^3}{\left(1 - \Phi_t^{ijk}\right)^2 \tau^2} d^2$$
(13)

Numerical Simulations

To obtain the effective properties of the samples we used COMSOL. The required input files of local (elemental) σ, and permeability data, were used in the numerical simulations to compute the effective transport properties of the samples in the three directions, Fig. 12. COMSOL's electrical current and Darcy moduli were used to determine the conductivity and permeability, respectively, using a voltage difference of 1 V and a pressure difference of 1 Pa on the facies of the desired direction, while a no-current and no-flow boundary condition was applied to the other facies. Only the results in the Z direction were compared to the laboratory measurements, while for the results obtained in the X and Y directions, X and Y were used for the anisotropy assessment.

The output of the COMSOL electrical current module is the current flux, J (Amperes), which was then used with Ohm's law (Eqn. 14), to compute σ. The only needed input file for this modulus is σ (S/m). The formation factor is then calculated from Eqn. 15.

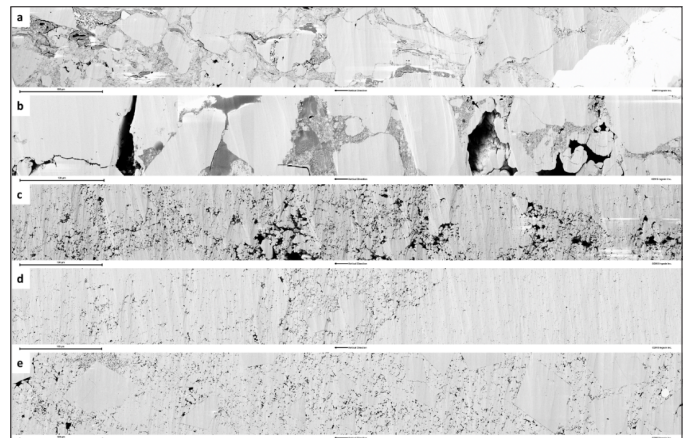$$\sigma_{eff} = -\frac{J}{\Delta V A}$$
(14)

Fig. 13. SEM images of five normal to bedding samples: (a) Pair 1-⊥, (b) Pair 2-⊥, (c) Pair 3-⊥, (d) Pair 4-⊥, and (e) Pair 5-⊥.

Sample	Specific Surface Area (1/mm)	Average Grain Size (mm)	Porosity (fraction)	Permeability (mD)
Pair 1-⊥	0.0308	0.0052	0.0761	0.0308
Pair 2-⊥	0.0193	0.0045	0.0722	0.0193
Pair 3-⊥	0.2081	0.0045	0.1504	0.2081
Pair 4-⊥	0.1068	0.0026	0.1707	0.1068
Pair 5-⊥	0.7832	0.0075	0.1641	0.7832

Table 2. The minerals' densities used to calculate the ρ_g of the five pairs of samples[12]

Sample	ρ_b (g/cc)	Klinkenberg Permeability (mD)	Porosity (fraction)	Parameters (from resistance)	
				Fa	m
Pair 1-//	2.72	0.030	0.059	204.84	1.88
Pair 1-⊥	2.71	0.026	0.072	117.79	1.81
Pair 2-//	2.72	0.009	0.083	73.61	1.73
Pair 2-⊥	2.72	0.016	0.073	121.39	1.83
Pair 3-//	2.70	3.47	0.156	34.64	1.91
Pair 3-⊥	2.70	1.85	0.149	35.93	1.88
Pair 4-//	2.55	5.75	0.168	28.16	1.87
Pair 4-⊥	2.54	0.073	0.167	78.16	2.44
Unpaired-⊥	2.54	0.055	0.161	74.43	2.36

Table 3. Laboratory measurements for each sample

where V is the electrical potential and A is the cross-sectional area of the sample.

$$F = \frac{1}{\sigma_{eff}\, R_w} \tag{15}$$

Similarly, COMSOL's Darcy flow simulator's output is the fluid flux, Q (m³/s). Darcy's law (Eqn. 16) was then used to calculate the permeability in mD:

$$k_{eff} = -\frac{\mu Q}{\Delta p A} \tag{16}$$

where p is the pore pressure and A is the cross-sectional area.

2D SEM IMAGES

2D SEM images were used to estimate the d_g in millimeters using the specific surface area (sS) relation, and thereby reduce the uncertainty in our permeability prediction.

The SEM images were acquired for the five normal to bedding samples, Fig. 13, resulting in a pixel resolution dx of 10^{-4} mm. The images were segmented into grains and pores by applying a threshold to estimate the specific surface area. After computing the specific surface area, Eqn. 17 was used to calculate the d_g in millimeters[3].

$$d_g = 10^3 \frac{6\,(1 - \phi)}{sS} \tag{17}$$

These new d_g values were then used in the Kozeny-Carman equation (Eqn. 7) to recalculate the permeability. Table 2

shows the summarized results of the five samples.

LABORATORY MEASUREMENTS

The laboratory measurements, Table 3, include the ϕ, ρ_g, Klinkenberg corrected k, apparent formation factor, Fa, and the cementation exponent, m (assuming that the tortuosity parameter $a = 1$) for each sample. The measurements were conducted under a confining stress of 15 MPa. The ϕ and k measurements were made using gas. While conducting the resistivity measurements, the resistivity of brine was 0.174 Ω.m.
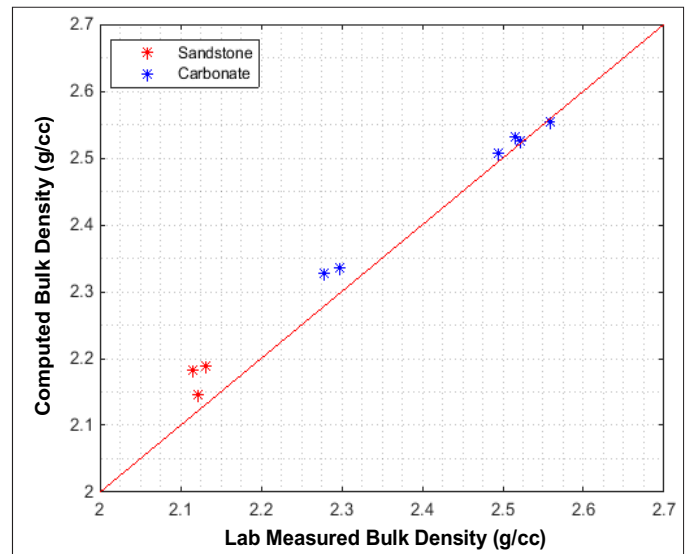

Fig. 14. The computed and measured ρ_b of the carbonate and sandstone samples. The dual energy CT scan data have excellent match.
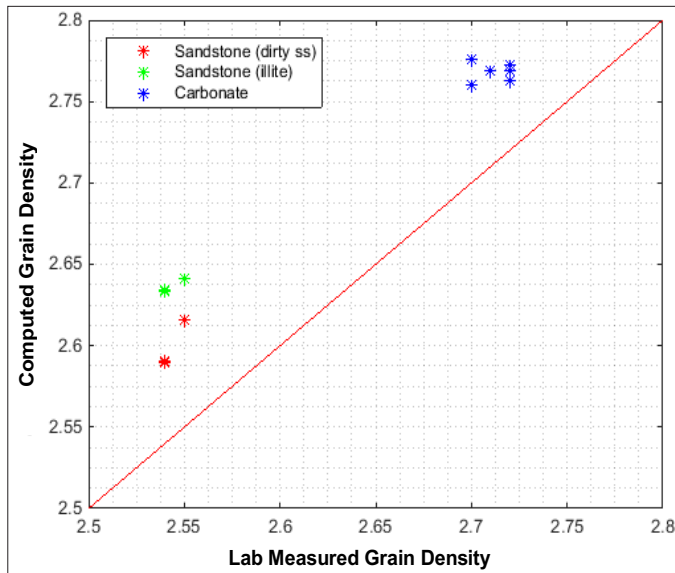
Fig. 15. The computed and measured ρ$_g$ of the carbonate and sandstone samples. The computed results are slightly higher than the measured densities. The dirty sandstone case shows a better match than the illite case.
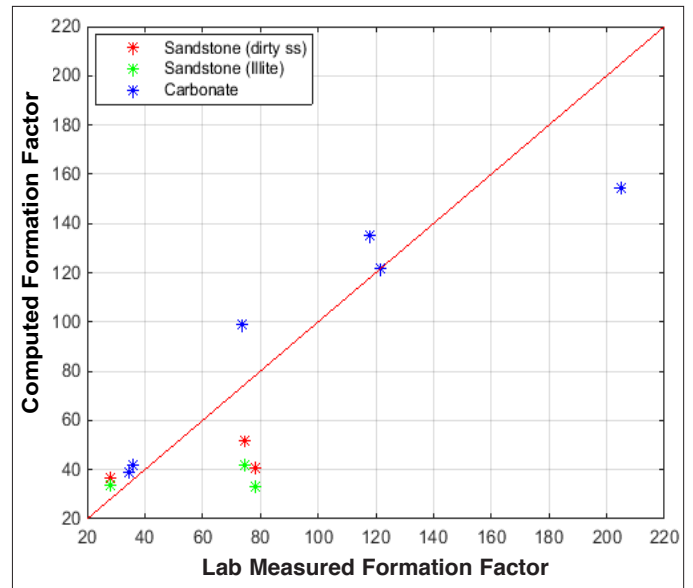

Fig. 17. The computed and measured formation factor for the carbonate and sandstone samples. The carbonate results match is higher than the sandstone samples. Both the dirty sandstone and illite give similar results.
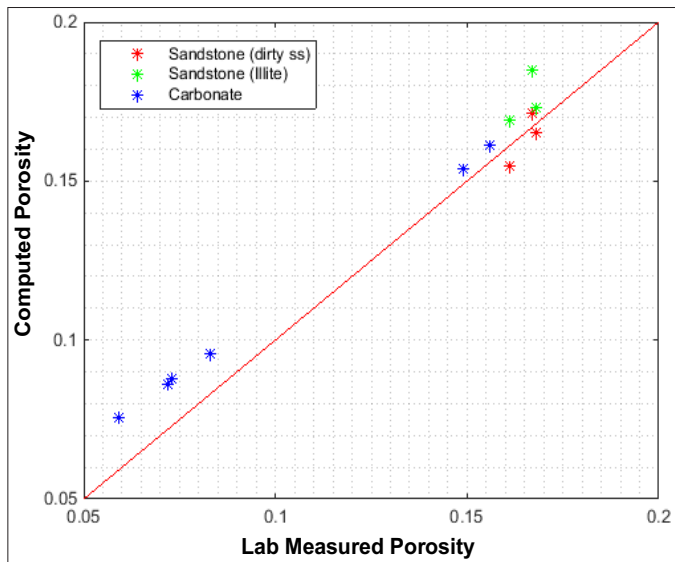

Fig. 16. The computed and measured porosities of the carbonate and sandstone samples. There is a good match, but the computed porosities are consistently higher. The dirty sandstone case shows better correlation.
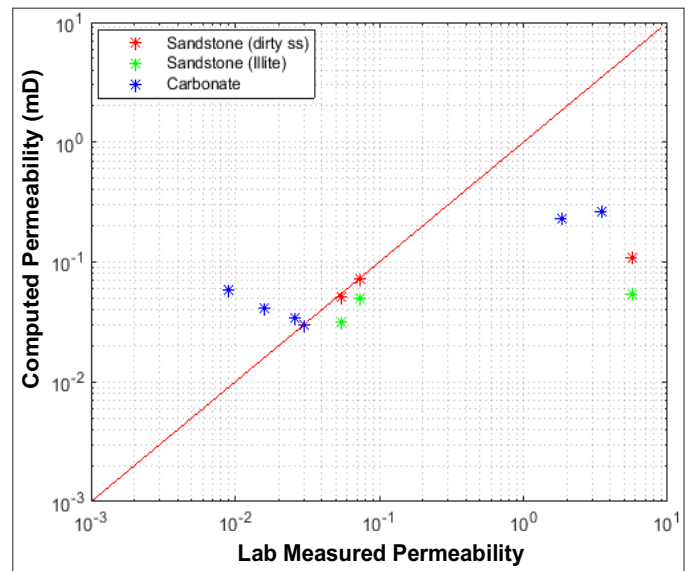

Fig. 18. The computed and measured permeability for the carbonate and sandstone samples.

RESULTS

Rock Properties

The measured ρ_b closely matches the volumetric average of the ρ_b at each voxel obtained using the dual energy CT, Fig. 14. The ρ_g obtained using laboratory measurement data also match the computed values, using the P_f data, especially so for the carbonate samples, Fig. 15. Computing the sandstone ρ_g was not as trivial because of its more complex mineralogy. Therefore, using a single clay mineral, illite, resulted in a larger deviation from the measured ρ_g, but when an average "dirty" sandstone value was used, the match was better. Both the ρ_b and the ρ_g are consistently higher than the laboratory measured ones.

We attribute this mismatch to the fact that some of the P_f values, as provided by dual energy scans, fell outside of the bounds for pure mineral end members. The reason for this effect is unknown, however, we feel that this apparently small mismatch justifies the method we used.

Of course, the laboratory data presented here are not necessarily the ground truth. For example, the laboratory ρ_g for sandstone in Fig. 15 is smaller than 2.55 g/cc, while that of pure quartz is 2.65 g/cc.

Both the laboratory measured and computed porosities match as well, but since the computed ρ_g were higher than the measured, we expected the ϕ to be slightly higher as a result, Fig. 16. The carbonate samples show a better match than the sandstone samples and "dirty" sandstone results have a closer match than the illite results.

Notice that in the low-porosity carbonate samples, the laboratory measured ϕ is about 0.01 to 0.015 smaller than the computed ϕ. One reason for this may be that in these tight samples, there are some disconnected pores, and as a result, the gas used in the laboratory measurement did not enter these pores. If this is so, the DRP method we used here may give a better ϕ estimate.

The computed formation factors were obtained using a fixed cementation exponent — $m = 2$ — for all the samples, while the cementation exponent derived from laboratory resistivity measurements for each sample somewhat differs from 2. Still, the formation factor values from DRP and the laboratory are fairly close to each other, Fig. 17, especially considering the fact that the formation factor is often displayed using a log scale.

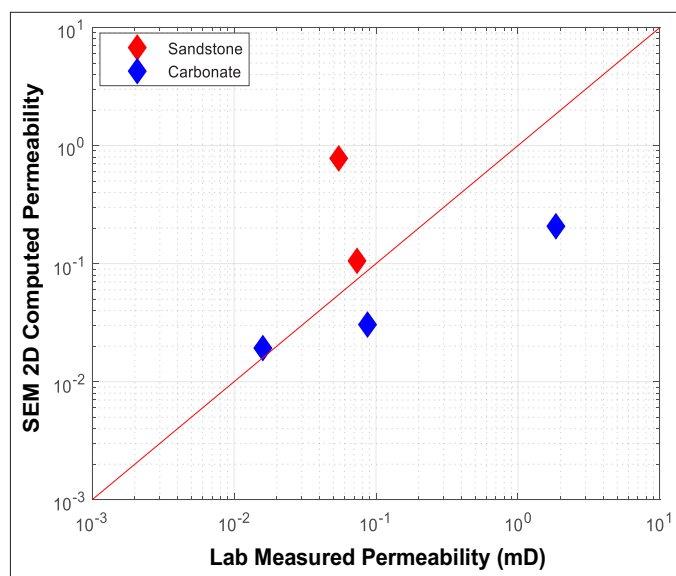The k match, Fig. 18, is not nearly as good as the formation factor match. The match is fairly good for some samples, but in other samples the mismatch can be as high as a factor of 10. The high measured k values may be attributed to small fractures that were not evident in CT scans. Also, because we use the Kozeny-Carman k equation, the assumed tortuosity and grain size values used in Eqn. 7 may not be appropriate. The permeability was recalculated using grain size values obtained from SEM images from five normal to bedding samples, Fig. 19, which slightly improved the match with the laboratory data.

Anisotropy of Transport Properties

We ran numerical simulations on the three directions X, Y, and Z, on each sample. Numerical simulations over the Z axis matches the laboratory measurement direction while the results of the numerical simulations over the X and Y directions were used to analyze the anisotropy of each sample. Table 4 and Table 5 show the resulting permeabilities and formation factors for the carbonate and sandstone samples, respectively. Both transport properties, k, and electrical properties in the directions are practically identical. Therefore, the samples appear almost isotropic. In addition, when comparing the parallel and normal to bedding pairs, we found that there are no large differences between the parallel and normal to bedding core plugs, which agrees with the results of the numerical simulations over the three directions.

CONCLUSIONS

The presented method shows promising results that can certainly be improved upon with additional DRP analysis, such as imaging selected subsamples at the pore scale and finding the effective grain size. The dual energy CT scan, ρ_b, is close to the lab measurements. Knowing how to interpret the P_f

Fig. 19. The SEM computed permeability and measured permeability for the carbonate and sandstone samples.

Carbonates	Permeability (mD)			Formation Factor		
Core Plug	X	Y	Z	X	Y	Z
Pair 1-//	0.028	0.027	0.030	162.532	164.773	154.405
Pair 1-⊥	0.041	0.042	0.034	126.899	125.807	135.443
Pair 2-//	0.053	0.053	0.058	105.758	104.942	99.100
Pair 2-⊥	0.045	0.044	0.042	118.956	121.524	121.712
Pair 3-//	0.294	0.294	0.260	37.196	37.346	38.699
Pair 3-⊥	0.242	0.237	0.231	41.163	41.406	41.773

Table 4. Numerical simulation results of the carbonate samples

Sandstone	Permeability (mD)			Formation Factor		
Core Plug	X	Y	Z	X	Y	Z
Pair 4-//	0.031	0.036	0.046	42.405	34.632	36.699
Pair 4-⊥	0.229	0.064	0.031	31.794	31.729	40.524
Unpaired-⊥	0.050	0.051	0.022	38.641	38.240	51.697

Table 5. Numerical simulation results of the sandstone samples

data is the key to get accurate ρ_g and ϕ. In principle, this method can be used to quantify the transport properties of rock. The computed formation factor results appear more reliable that the k results. The latter are clearly more difficult to obtain due to uncertainty in the Kozeny-Carman parameters. The k results were improved by obtaining grain size values from the SEM images.

ACKNOWLEDGMENTS

REFERENCES

1. Andrä, H., Combaret, N., Dvorkin, J., Glatt, E., et al.: "Digital Rock Physics Benchmarks — Part I: Imaging and Segmentation," *Computers & Geosciences*, Vol. 50, January 2013, pp. 25-32.

2. Abbad, A. and Dvorkin, J.: "Estimating Rock Transport Properties of Sandstone and Carbonate Samples Using Coarse Resolution 3D Dual Energy Images," paper presented at the 78th EAGE Conference and Exhibition 2016, Vienna, Austria, May 30-June 2, 2016.

3. Mavko, G., Mukerji, T. and Dvorkin, J.: *The Rock Physics Handbook: Tools for Seismic Analysis of Porous Media*, 2nd edition, Cambridge University Press, New York, April 2009, 524 p.

4. Plumb, R.A., Evans, K.F. and Engelder, T.: "Geophysical Log Responses and their Correlation with Bed-to-Bed Stress Contrasts in Paleozoic Rocks, Appalachian Plateau, New York," *Journal of Geophysical Research*, Vol. 96, Issue B9, August 1991, pp. 14509-14528.

BIOGRAPHIES

Abrar A. Alabbad is a Geologist working with the Geology Technology Division of Saudi Aramco's Exploration and Petroleum Engineering Center – Advanced Research Center (EXPEC ARC). So far in her career, she has worked on low resistivity, and low contrast pay zones in central Arabian clastic reservoirs. In addition, Abrar has worked on developing rock physics models for Jurassic carbonate reservoirs in Arabia.

Currently, she is focusing on digital rock physics and automation in geology by tackling multiscale data integration and utilizing advanced imaging technologies, including micro-computed tomography (CT), dual energy CT, confocal thin-section images, X-ray fluorescence, and by scanning electron microscope.

Abrar has authored several conference and peer-reviewed journal papers. She is a member of the European Association of Geoscientists and Engineer's Education Committee.

Abrar received her B.S. degree in Geoscience from Pennsylvania State University, State College, PA, and an M.S. degree in Geophysics from Stanford University, Stanford, CA.

Dr. Jack Dvorkin is the Program Leader in Rock Physics at King Fahd University of Petroleum and Minerals (KFUPM). He started his career in Geophysics in 1989 when he joined the Stanford University Rock Physics group. While at Stanford, Jack supervised over 20 students working toward their Ph.D. and M.S. degrees, and taught a regular class on applications of rock physics to reservoir characterization. He has taught rock physics classes worldwide.

Since then, Jack has coauthored three books on rock physics, as well as authored and coauthored over 150 refereed papers, mainly on the same topic. His last book is "Seismic Reflections of Rock Properties," and was published in 2014 by Cambridge University Press.

Jack is a co-founder of two companies, Rock Solid Images and Ingrain, both in Houston. He holds several U.S. patents, mostly in computational rock physics.

Jack's current interests include theoretical and computational rock physics, as well as applications of the rock physics laws and transforms across a range of spatial scales.

He was awarded a Society of Exploration Geophysicists Honorary Member Award in 2014. Also in 2014, Jack was one of three researchers at Stanford who won the ENI Award "New Frontiers of Hydrocarbon."

Between 1974 and 1989, he worked as a researcher in the petroleum industry in the USSR.

In 1980, Jack received his Ph.D. degree in Continuum Mechanics from Moscow University, Moscow, Russia.